Multi-Wavelength *in vivo* Photon Absorption Remote Sensing: Towards Non-Contact Label-Free Functional Vascular Imaging

by

Sarah J. Werezak

A thesis
presented to the University of Waterloo
in fulfillment of the
thesis requirement for the degree of
Master of Applied Science
in
Systems Design Engineering

Waterloo, Ontario, Canada, 2025

© Sarah J. Werezak 2025

Author's Declaration

I hereby declare that I am the sole author of this thesis. This is a true copy of the thesis, including any required final revisions, as accepted by my examiners.

I understand that my thesis may be made electronically available to the public.

Abstract

Blood oxygen saturation (SO_2) is an important functional metric in the diagnosis and monitoring of blinding eye diseases and cancer. Additionally, SO_2 imaging has high value in illustrating changes in blood oxygenation within a vascular network, particularity when changes are demonstrated within the context of surrounding biological structures. This has promising potential to provide valuable information to researchers and clinicians on the mechanisms of disease progression and the efficacy of treatment.

Various techniques have been explored for SO_2 imaging, however limitations of inaccuracy in measurement, a requirement of contact with the tissue and the reliance on exogenous labels have prevented the clinical adoption of these approaches. Photon absorption remote sensing (PARS) is a novel imaging technique that is label-free, non-contact and absorption-based. When a photon is absorbed by a biomolecule, energy can be released through radiative or non-radiative relaxation. Most imaging modalities are limited to capturing one form of relaxation contrast, however PARS is capable of capturing both simultaneously. The unique PARS approach has promising potential as an SO_2 imaging modality. This thesis explores work which furthers efforts towards accurate, non-contact, label-free SO_2 imaging using PARS.

First, system developments are implemented to demonstrate the first multi-wavelength *in vivo* PARS system. The use of independent excitation paths, power compensation, and the improvement of the secondary excitation generation enables the reliable and consistent *in vivo* multi-wavelength PARS imaging of chicken embryo vasculature. Additionally, the power compensation of incident excitation pulses is critical for quantitative SO_2 measurements to ensure that measured SO_2 is not impacted by power variations in the excitation source.

This is followed by the development of techniques for *in vitro* phantom studies. A blood oxygenation and deoxygenation protocol is developed and tested, enabling the time-efficient and low-cost preparation of blood samples at various oxygenation levels. Additionally, a flow phantom is developed with a 50 μm channel which successfully enables PARS signal to be captured from blood in an *in vitro* flow phantom. This experimental setup was unable to demonstrate a change in PARS signal across various blood samples at differing oxygenation levels. Simulation is used to demonstrate that the blood preparation and samples are not the cause of the unsuccessful result. This result is determined to be a consequence of the flow phantom design. The knowledge gained through the iterative design process provides valuable insight to guide future flow phantom developments.

Finally, *in vivo* experimentation of the multi-wavelength PARS system successfully demonstrated the variation in blood oxygenation during the hypoxia and recovery of a

chicken embryo. The hypoxia holder was designed to modulate the ambient oxygen inside the holder and induce states of hypoxia and recovery. This highlights the success of the PARS multi-wavelength system in demonstrating a relative change in SO_2 *in vivo*.

The presented work furthers efforts towards accurate, non-contact, label-free PARS SO_2 imaging through the development of the first multi-wavelength *in vivo* PARS system, *in vitro* blood and flow phantom developments and the *in vivo* demonstration of relative change in SO_2 measured using PARS.

Acknowledgements

Many thanks are extended to the team at the Photomedicine Labs, it has been a pleasure get to know each of you over the past two years. I am very grateful for this opportunity to explore fascinating research, and grow my skill set in science and engineering, for this I extend many thanks to my supervisor Dr. Parsin Haji Reza. I would like to acknowledge James A. Tummons Simmons for his work developing the single excitation *in vivo* PARS system and the software tools for system control and data extraction, all of which were instrumental to the success of this project. I am grateful for his technical guidance, and am very appreciative of his support in the lab, throughout the hours debugging technical issues or the exhausting hours and *hours* of *in vivo* imaging. I am grateful for Hager Gaouda and Sabeena Giri, who's hard work continuously caring for the chicken embryos made these *in vivo* results possible. Additionally, I would like to thank Hager Gaouda for her support and expertise throughout the laborious trial and error to determine the methods for *in vitro* blood oxygenation and deoxygention, and for always being willing to answer all my biology related questions. Many thanks goes to Jenna Veugen, whose friendship and support helped me laugh through the challenging moments. I appreciate our technical discussions, her suggestions and encouragement when I felt like I reached a dead end, and being able to pick her brain about optical fibers. I would like to thank Stephanie Clarke, whose administrative efforts ensured I had the resources I needed to be successful, and whose friendship brought the fun to my day-to-day.

I am very appreciative of my committee members for their time and feedback in reviewing this work, thank you.

Many thanks goes out to my family and friends for their continuous support. I'm most grateful for their encouragement, and their interest in hearing all about whatever cool and exciting piece of science or engineering that I was learning about. I could have not done this without you!

The funding for this work is provided by the following: Natural Sciences and Engineering Research Council of Canada, Canada Foundation for Innovation, Mitacs Accelerate, University of Waterloo Startup funds, Centre for Bioengineering and Biotechnology, illumiSonics Inc, New frontiers in research fund, the Canadian Institutes of Health Research and the Ontario Graduate Student Scholarship.

Dedication

This work is dedicated, in loving memory, to my Granddad, George Werezak (PhD, P.Eng). He was the first of three generations to pursue engineering and inspired my pursuit of graduate studies. I also dedicate this thesis to my Grandma, Diane Werezak, for her continuous and enthusiastic support of my pursuit for higher education.

Table of Contents

Author's Declaration ii

Abstract iii

Acknowledgements v

Dedication vi

List of Figures xi

List of Tables xiii

1 Introduction 1

1.1 Motivation 1

1.2 Thesis Objectives 2

1.3 Thesis Organization 3

2 Background & Literature Review 4

2.1 Optical Imaging Principles 4

2.2 Accuracy, Consistency and Repeatability 6

2.2.1 Terminology 6

2.2.2 PARS-SO_2 Accuracy 6

2.3 SO_2 Determination . . . 8
2.4 Current Modalities for SO_2 Imaging . . . 10
2.4.1 Scattering-based SO_2 Imaging Modalities . . . 10
2.4.2 Radiative SO_2 Imaging Modalities . . . 14
2.4.3 Non-Radiative SO_2 Imaging Modalities . . . 16
2.5 Photon Absorption Remote Sensing . . . 18
2.6 Stimulated Raman Scattering . . . 22
2.6.1 Raman Scattering . . . 22
2.6.2 Raman Gain . . . 23
2.6.3 Raman Threshold . . . 24
2.6.4 SRS Generation within A Fiber . . . 24
2.6.5 Polarization and SRS . . . 24
2.7 Conclusion . . . 27

3 Multi-Wavelength *in vivo* PARS System 28
3.1 Introduction . . . 28
3.2 Background . . . 29
3.2.1 Excitation Wavelength Selection . . . 29
3.2.2 Generating 558 nm with Stimulated Raman Scattering . . . 30
3.2.3 Independent Excitation Paths . . . 30
3.3 Methods . . . 30
3.3.1 558 nm Excitation Generation . . . 30
3.3.2 Optical System Architecture . . . 31
3.3.3 Imaging System Characteristics . . . 34
3.3.4 Interlacing and Image Extraction . . . 35
3.4 Results & Discussion . . . 36
3.4.1 Power Compensation . . . 36
3.4.2 558 nm Excitation Generation . . . 39
3.4.3 Multi-Wavelength *in vivo* PARS Images . . . 42
3.5 Conclusions . . . 45

4 *In vitro* Blood Deoxygenation and Oxygenation **46**
4.1 Introduction . . . 46
4.2 Background . . . 46
4.2.1 Blood Deoxygenation and Oxygenation . . . 46
4.2.2 Methemoglobin & Carboxyhemoglobin . . . 47
4.3 Methods . . . 48
4.3.1 Blood Selection . . . 48
4.3.2 Deoxygenation . . . 48
4.3.3 Oxygenation . . . 49
4.4 Results & Discussion . . . 51
4.4.1 Impact of Yeast on Non-Radiative Contrast . . . 51
4.4.2 Blood Deoxygenation and Oxygenation . . . 52
4.5 Conclusion . . . 54
4.6 Future Work . . . 55

5 *In vitro* Flow Phantom **56**
5.1 Introduction . . . 56
5.2 Background . . . 56
5.2.1 Optical Properties of a Single Red Blood Cell . . . 56
5.2.2 Phantom Models . . . 57
5.3 Design Requirements . . . 58
5.4 Material Selection . . . 59
5.5 Methods . . . 59
5.5.1 Flow Phantom Preparation . . . 59
5.5.2 Flow Phantom Experimental Procedure . . . 61
5.6 Results & Discussion . . . 61
5.7 Conclusion . . . 65
5.8 Future Work . . . 66

6 *In vivo* Blood Oxygenation **67**
6.1 Introduction . . . 67
6.2 Background . . . 67
6.3 Methods . . . 68
6.3.1 Hypoxia Holder . . . 68
6.3.2 Hypoxia Holder Sensors . . . 70
6.3.3 Experimental Methods . . . 70
6.3.4 Image Processing . . . 71
6.4 Results & Discussion . . . 73
6.4.1 Hypoxia Holder Results . . . 73
6.4.2 *In vivo* Blood Oxygenation Results . . . 74
6.5 Conclusion . . . 84
6.6 Future Work . . . 84

7 Conclusion **86**

Letters of Copyright Permission **88**

Bibliography **96**

APPENDICES **108**

A *In vitro* Blood Preparation Additional Information **109**
A.1 H_2O_2 Volumes for Blood Re-oxygenation . . . 109

B Initial Phantom Designs **110**
B.1 Design A: Liquid Sample Holder . . . 110
B.2 Design B: Flow Phantom Version 1 . . . 110

List of Figures

2.1 Jablonski Energy Diagram of Absorption 5
2.2 Deoxy- and Oxy-Hemoglobin Absorption Spectra 8
2.3 Oxymap T1 Fundus Photography Retinal Oximetry 11
2.4 Functional Hyperspectral Imaging of Vasculature of a Tumor 12
2.5 Vis-OCT Oximetry Map of the Optic Disk in a Human Retina 13
2.6 *In vivo* SO_2 Photoluminescence Imaging of Various Tumor Models 15
2.7 Multi-Photon Label-Free *in vivo* Colour Third-Order Blood Oxygenation in Adult Zebrafish Brain 16
2.8 Photoacoustic Imaging of a Mouse Brain in Normoxia and Hypoxia 17
2.9 Photoacoustic Remote Sensing System and Images of Chicken Embryo Vasculature 18
2.10 PARS Mechanism Diagram 19
2.11 PARS Composite Images of *in vivo* Chicken Embryo Vasculature 20
2.12 PARS Composite Images of *in vivo* Mouse Ear 21
2.13 Spontaneous and Stimulated Raman Scattering Jablonski Diagram 22
2.14 Single Mode and PANDA Polarization-Maintaining Fiber 25
2.15 Light Propagation in a Polarization-Maintaining Fiber 26
2.16 Half-Wave Plate (HWP) Diagram 27

3.1 Labeled Absorption Spectra of HbO_2 and Hb 29
3.2 Multi-Wavelength PARS *in vivo* System Diagram 32

3.3 Comparison of the Distribution of Power Compensation Measurements . . 36
3.4 Power Compensation of 558 nm Excitation on Carbon Fibers 38
3.5 SRS Spectra Across HWP Angle 40
3.6 SRS Spectra Across Laser Set Point 41
3.7 SRS Spectra Before and After Filtering 42
3.8 Multi-Wavelength *in vivo* Interlaced PARS Images of Chicken Embryo . . 44

4.1 Whole Sheep Blood Before and After Yeast Deoxygenation 49
4.2 Blood Chemical Oxygenation Method 50
4.3 PARS Images of Red Blood Cells and Yeast on Slides 51
4.4 Simulated Absorption Ratio With and Without Dyshemoglobins 54

5.1 Flow Phantom Diagram 60
5.2 Flow Phantom PDMS Mold 61
5.3 Multi-Wavelength Images of Blood in the Flow Phantom 62
5.4 Ratio of Non-Radiative Intensities of Blood in the Flow Phantom 64

6.1 Hypoxia Holder Diagram 69
6.2 Hypoxia Holder Photos 69
6.3 Hypoxia Holder Changes in Ambient Environment 73
6.4 Hypoxia Holder Ambient Oxygen, Location and Occurrence of Datasets Acquired During Hypoxia Experiment 74
6.5 Multi-wavelength PARS Images of Dataset Location 75
6.6 Detection Scattering Across Hypoxia Datasets 76
6.7 Segmented Mask and Non-radiative Angiography CAM Images 77
6.8 CAM Hypoxia Experiment Results without Power Compensation 79
6.9 CAM Hypoxia Experiment Results with Power Compensation 80
6.10 Repetition of CAM Hypoxia Experiment Results with Power Compensation 83

B.1 Liquid Sample Holder 111
B.2 Flow Phantom Version 1 111

List of Tables

2.1 Terminology. 6

3.1 Experimental beam width, resolution, and theoretical depth of focus. . . . 35

4.1 *In vitro* whole sheep blood deoxygenation and oxygenation 52

6.1 Hypoxia holder sensor specifications. 70

A.1 Blood re-oxygenation to intermediate SO_2 values. 109

Chapter 1

Introduction

1.1 Motivation

Understanding vascular function provides critical information on tissue health and disease pathology. Blood oxygen saturation (SO_2) is an important functional metric that can be used to characterize hypoxia and non-perfusion in tissue. This metric has the potential to provide high value information to clinicians and researchers in the diagnosis and monitoring of treatment efficacy in cancer [1][2][3][4] and blinding eye diseases [5][6].

In 2020, GLOBOCAN reported 19.3 million new cancer cases and 10 million cancer related deaths worldwide. Estimates suggest that in 2040 there will be 28.4 million new cancer cases [7]. Tissue hypoxia is a physical factor which contributes to the progression of cancer. Angiogenesis occurs in response to hypoxia, wherein tumors generate their own vasculature to meet metabolic requirements [8]. As a result, SO_2 has become an important metric for tissue characterization and prediction of treatment response for various pathologies such as breast cancer [1][2], esophageal cancer [3], and prostate cancer [4].

Additionally, over 8 million Canadians live with major eye diseases such as diabetic retinopathy (DR) and glaucoma, and vision loss in Canada costs a total of $33 billion per year [9]. Early detection of eye disease is critical for minimizing the severity of vision loss [9]. Recent studies have correlated retinal non-perfusion with the worsening of DR [5] and linked a higher retinal SO_2 with increased damage of the visual field in glaucoma [6]. Due to the functional changes associated with blinding eye diseases and cancer, accurate and clinically applicable SO_2 imaging has immense potential to revolutionize diagnosis and treatment.

Blood has high optical absorption, and absorption differs between oxy- and deoxy-hemoglobin across wavelengths. Current gold standard technology such as OCT and multi-wavelength fundus photography indirectly measures absorption changes through optical scattering. However, the accuracy of scattering-based systems is limited by confounding factors such as local geometry (e.g. vessel diameter) and surrounding biomolecules (e.g. melanin) [10][11]. Absorption-based methods, such as photoacoustics (PA), have an advantage over scattering-based methods by directly measuring absorption. Precise *in vivo* SO_2 has been achieved with PA, and through simulation PA has been demonstrated as accurate regardless of melanin concentration or vessel diameter [10][11]. However, PA is limited by the requirement of physical contact; this presents challenges in fragile tissues such as open wounds and the eye.

Photon Absorption Remote Sensing (PARS) is an advantageous, absorption-based, technology that does not require contact with tissue. Following an absorption event, energy is released through radiative or non-radiative relaxation based on the quantum yield of the biomolecule. Molecular specificity is achieved by selecting excitation wavelengths, which target chromophore-specific absorption, and capturing both radiative and non-radiative relaxations. Green excitation targets hemoglobin absorption, which has a low quantum yield, thus providing non-radiative contrast. Radiative relaxation from surrounding biomolecules is captured simultaneously without additional excitation, providing valuable structural context and facilitating the un-mixing of confounding biomolecules. PARS has recently demonstrated *in vivo* vasculature imaging in chicken embryo and mouse ear, with video-rate imaging speeds capable of capturing flow of individual red blood cells in chicken embryo capillaries [12]. Photoacoustic Remote Sensing demonstrated initial SO_2 results in chicken embryo [13] and rodent eye [14], however these results do not meet ISO standards for oximeter accuracy of a Root Mean Square (RMS) of $\leq 4\%$ [15].

This work includes the initial developments of the first *in vivo* multi-wavelength PARS imaging system. System developments improve the consistency and reliability of multi-wavelength imaging. Additionally, *in vitro* and *in vivo* studies explore the application of PARS for SO_2 imaging. This work promises to extend the capabilities of previous systems, laying the groundwork for SO_2 metrics and working towards a PARS oximeter system that achieves ISO accuracy standards [15].

1.2 Thesis Objectives

The high level goal of this work is to further efforts towards accurate PARS SO_2 imaging. These efforts are sub-divided into the following three main objectives:

1. Develop a multi-wavelength *in vivo* PARS system capable of consistent and reliable *in vivo* vascular imaging with two green excitation wavelengths.

2. Implement *in vitro* studies of PARS SO_2 measurement through the establishment of *in vitro* blood deoxygenation and oxygenation methods, as well as the development of a PARS-specific flow phantom.

3. Illustrate the capability of PARS to demonstrate relative change in SO_2 through the design and implementation of an *in vivo* hypoxia study.

1.3 Thesis Organization

The chapters within this thesis are organized as follows:

- Chapter 2 provides relevant technical background and an overview of current technology used for SO_2 imaging.
- Chapter 3 discusses the development of the multi-wavelength *in vivo* PARS system, and demonstrates reliable and consistent *in vivo* multi-wavelength images.
- Chapter 4 explores the development of a PARS-specific protocol for blood oxygenation and deoxygenation for use in *in vitro* phantom studies.
- Chapter 5 discusses the development of a custom flow phantom and results from *in vitro* studies of PARS SO_2 imaging.
- Chapter 6 presents the design of a custom hypoxia holder and the experimental results of *in vivo* hypoxia studies to demonstrate relative PARS SO_2.
- Chapter 7 provides conclusions and an overview of key results.

Chapter 2

Background & Literature Review

2.1 Optical Imaging Principles

The medical imaging devices typically found in a clinical setting include magnetic resonance imaging (MRI), X-rays radiography and computed tomography (CT) as well as ultrasound imaging. X-ray was first discovered in 1895, and in the 1940s ultrasound was introduced into medicine. Both CT and MRI were invented in the 1970s [16]. These techniques have become standard practice in the medical field and provide high value medical imaging.

Optical imaging is emerging as a valuable tool to further the capabilities of medical imaging. An advantage of optical imaging in medical applications is the use of non-ionizing, safe radiation. Additionally, light matter interactions within biological material can be leveraged to derive valuable, and clinically relevant information [16].

The primary modes of light matter interaction are scattering and absorption. Optical scattering is dominant in most biological tissue, and occurs when the path of a photon is re-directed by a biological structure. This occurs predominantly when the structure has a refractive index mismatch with respect to the surrounding medium, or when the optical wavelength matches the size of the structure. The probability of light being scattered in a particular medium is defined by the scattering coefficient (μ_s) [16].

Optical absorption occurs when the energy of a molecule is increased from a ground state to an excited state through the absorption of a photon. This energy is released through non-radiative, or radiative relaxation. Figure 2.1 summarizes the various mechanisms through which relaxation occurs. Briefly, non-radiative relaxation occurs through the generation of heat. For radiative relaxation, energy is released through the emission of

another photon, this can occur through fluorescence, phosphorescence or Raman scattering. Optical absorption is molecule and wavelength specific, as such, valuable biochemical information can be derived from the absorption of light. The probability that a photon will be absorbed in a particular medium is defined by the absorption coefficient (μ_a), and the primary absorbers in biological tissues are hemoglobin, melanin and water [16].

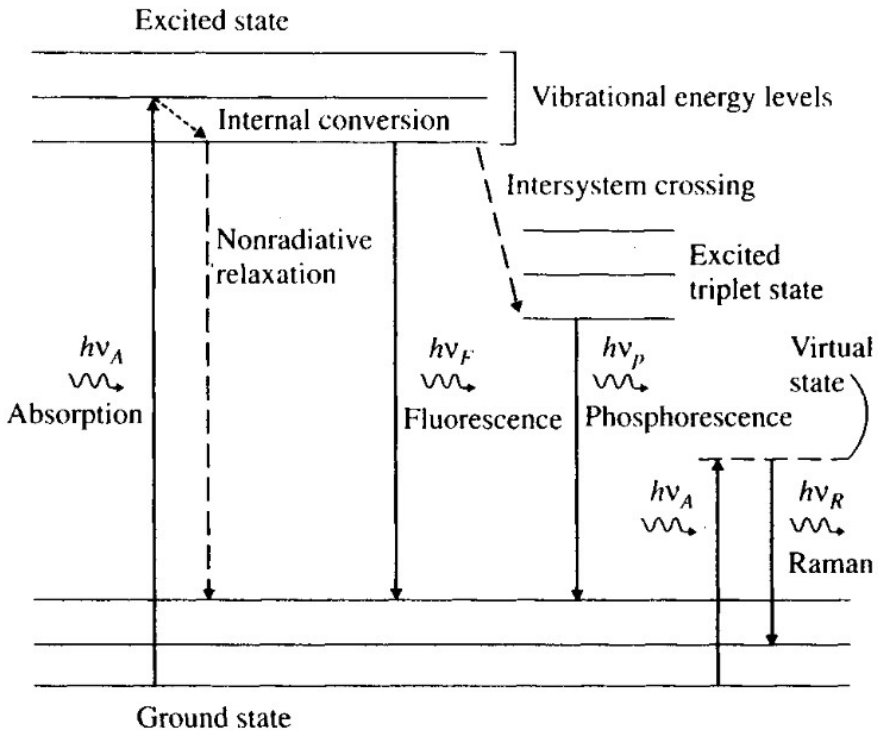


Figure 2.1: Jablonski energy diagram demonstrating absorption and the various mechanisms for relaxation, including non-radiative and radiative relaxations (fluorescence, phosphorescence and Raman). This figure is courtesy of Wang et al. [16] and is used with permission.

2.2 Accuracy, Consistency and Repeatability

2.2.1 Terminology

This work discusses the repeatability, consistency, accuracy etc. of SO_2 imaging and measurement systems. The terminology used throughout this work is defined below, and definitions are based on work by Hacker et al. [17].

Repeatability	The ability for the outcomes of an experiment, repeated on different days with the same procedure, to provide the same result when performed multiple times in the same lab, using the same equipment, by the same operator.
Consistency (Image)	The similarity between features of two or more images captured of the same imaging target using different excitation wavelengths for PARS imaging.
Accuracy	The closeness of an experimental measurement to the true value.
Bias	A systematic deviation of experimental measurements from the true value.
Validation	The process during which a method or system is assessed for accuracy and reliability.

Table 2.1: Terminology.

2.2.2 PARS-SO_2 Accuracy

The measurement of SO_2 using PARS can be broadly categorized into relative SO_2 and absolute SO_2. Relative SO_2 is demonstrated when oxy- and deoxy-hemoglobin concentration is shown to change proportionally with respect to itself and is measured in arbitrary units. Absolute SO_2 provides a measurement of the percentage of oxy- and deoxy-hemoglobin in the blood. An absolute PARS-SO_2 measurement is derived from a relative PARS-SO_2 measurement through the development of an empirical model. This model is derived by associating relative PARS-SO_2 measurements with known gold standard SO_2 measurements. Gold standard approaches are also used to assess accuracy of the absolute SO_2 measurement. Living tissue presents challenges for accurate, absolute SO_2 measurement due to factors such as blood vessel geometry (e.g. depth, diameter) and confounding bio-molecules (e.g. melanin) [10][11][18].

In this work, PARS-SO_2 accuracy is defined by the closeness of an absolute SO_2 measurement to the true oxy- and deoxy-hemoglobin concentration. This requires the use of gold standard approaches, such as blood gas analysis, to establish a true measurement against which PARS-SO_2 is compared. PARS-SO_2 accuracy metrics are determined with respect to gold standard blood gas analysis, using the assumption that these gold standard approaches provide ground truth measurements. Delving into the nuances of blood gas analysis accuracy is beyond scope of this work.

Current ISO and CSA standards for pulse oximeters outline an accuracy requirement of 4% root-mean-square error (RMSE) over a range of 70% to 100% oxygen saturation [15][19], however recent technology has outperformed this standard. Adaptive spectroscopic vis-OCT has demonstrated a 2.1% RMSE of major retinal arteries compared to a pulse oximeter [20]. Photoacoustic imaging has shown an RMSE of 2.16% in canine femoral arteries, and 3.97% in human radial arteries [21]. Near-infrared photoacoustic spectroscopy has demonstrated a measurement accuracy within 2.5% with a resolution of $\pm$ 1% in an *in vitro* validation study [22]. Finally, SO_2 accuracy of a commercial smartwatch has up to a RMSE of 2.9% when compared with clinical-grade pulse oximeters [23].

Current pulse oximeter technology is limited in accuracy across diverse populations, which was exposed in a landmark 2020 report that presented findings indicating a racial bias in pulse oximetry [24]. Additionally, a recent systematic review of 44 studies comparing pulse oximetry measured SO_2 against blood gas co-oximetry highlighted that pulse oximetry can overestimate the true SO_2 level in people with darker skin tones [25]. This is a critical area of research, not only in pulse oximetry, but throughout all types of SO_2 measurement techniques. Active research is addressing this in photoacoutsics [18], however many validation studies of SO_2 measurement devices lack adequate reporting on racial demographics. As PARS-SO_2 work continues, incorporating variable melanin concentration and skin tone will be crucial in validation studies and accuracy determination.

The ultimate goal for PARS-SO_2 is the ability to measure absolute SO_2 with an accuracy which meets, or is better than, the ISO and CSA standard. The PARS-SO_2 measurements should remain accurate despite factors such as melanin concentration and varying vessel geometry. Additionally, accuracy metrics must be validated across target tissue types, such as cancerous tissue or the retina, to account for differences in structure and bio-molecules in these tissues.

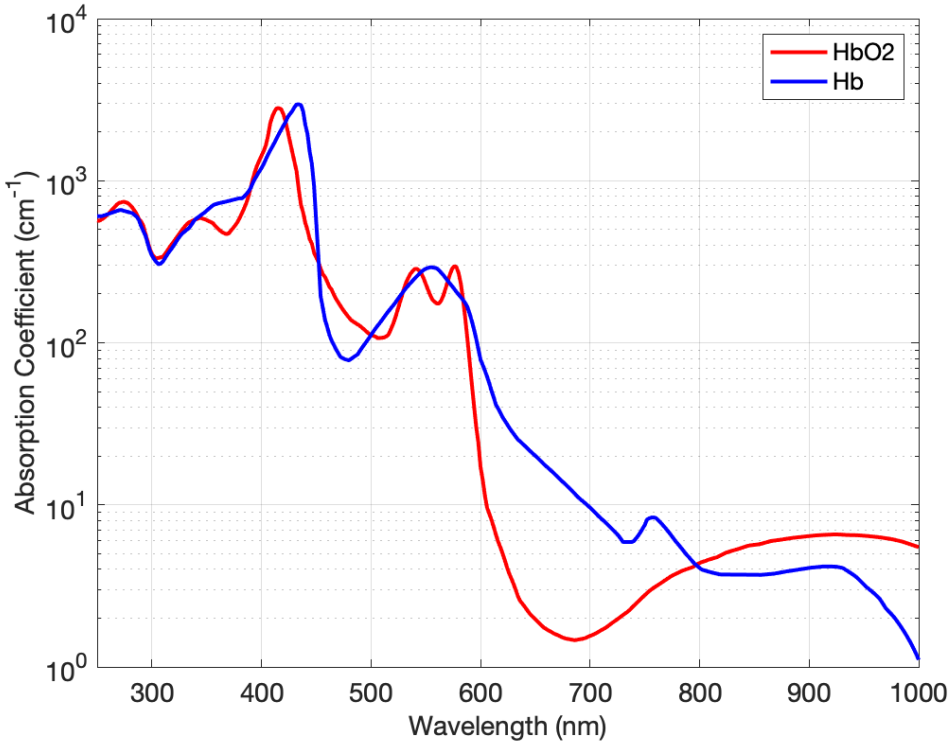


Figure 2.2: Absorption spectra of oxy-hemoglobin (HbO_2) and deoxy-hemoglobin (Hb). Original data source complied by Scott Prahl [26].

2.3 SO_2 Determination

Red blood cells (RBCs) make up 99% of the cells in normal human blood [27]. The primary protein found in RBCs is hemoglobin, which is responsible for oxygen transport in the body. This occurs when oxygen molecules (O_2) bind to one of four heme groups in a hemoglobin molecule. Oxy-hemoglobin (HbO_2) refers to the state of hemoglobin in which all heme groups are bound to oxygen, and deoxy-hemoglobin (Hb) refers to the unbound state of hemoglobin [28]. The absorption of oxy- and deoxy-hemoglobin varies greatly across the visible spectra as is shown in Figure 2.2. This absorption variation is the cornerstone of SO_2 measurement and imaging. The absorption of light is specific to the wavelength of incident light and the absorber species. This relationship is described using the Beer-Lambert Law for a single absorber species:

$$A(\lambda) = log_{10}(I_0/I) = \epsilon(\lambda) \cdot c \cdot l \tag{2.1}$$

Wherein $A(\lambda)$ represents the wavelength (λ) specific absorption, I is the intensity of transmitted light, and I_0 the intensity of incident light. The extinction coefficient $\epsilon(\lambda)$ is an absorption property specific to an absorber species at a particular wavelength, and c represents the concentration of the absorber species. Finally, l represents the path length of light propagating through the absorber [29][30].

For a mixture of multiple species of absorbers, the total absorption at a single wavelength is the sum of the absorption of each individual absorber species [29].

$$A(\lambda) = A_1(\lambda) + A_2(\lambda) + ... + A_n(\lambda) \tag{2.2}$$

Combining this definition with Equation 2.1, leads to the following equation [29]:

$$A(\lambda) = l \cdot (c_1 \cdot \epsilon_1(\lambda) + c_2 \cdot \epsilon_2(\lambda) + ... + c_n \cdot \epsilon_n(\lambda)) \tag{2.3}$$

To determine the fractional concentration of two absorber species, such as oxy- and deoxy-hemoglobin, the total absorption of blood is measured at two wavelengths with known extinction coefficients. To simplify the determination of the fractional concentration, a widely used approach is to select one wavelength at an isosbestic point, such that the extinction coefficient of both species is the same. The second wavelength is selected at a non-isosbestic point where the extinction coefficients vary greatly. In this configuration, fractional concentration (F) is determined as shown in Equation 2.4 [29].

$$F = \frac{c_2}{c_1 + c_2} = a \cdot \frac{A(\lambda_1)}{A(\lambda_2)} + b \tag{2.4}$$

Here a and b are constants which represent the ratio of absorption for a solution containing exclusively species 1 or 2 [29]. Equation 2.4 demonstrates the use of absorption measurements in determining the fractional concentration of two absorber species. This can be applied to the determination of fractional oxygen saturation (FSO_2), which is defined as the ratio of oxy-hemoglobin (O_2Hb) to deoxy-hemoglobin (Hb). This is referred to as simply SO_2 in this work.

$$FSO_2 = \frac{O_2Hb}{Hb + O_2Hb} \cdot 100\% \tag{2.5}$$

The Beer-Lambert law provides the basis for determining the fractional concentration of oxy- and deoxy-hemoglobin to measure SO_2. Implicit assumptions of the Beer-Lambert law include the assumption that absorption is the only interaction between the absorber species and radiation [29]. In complex *in vivo* structures, this assumption is not guaranteed. Many other scattering and absorbing bio-molecules are present *in vivo* beyond oxy- and deoxy-hemoglobin. As a result, it is important to establish an empirical model specific to an imaging modality and tissue type in order to account for such confounding factors. However, the Beer-Lambert law provides the foundational approach for SO_2 determination.

2.4 Current Modalities for SO_2 Imaging

Various approaches exist for the measurement and imaging of SO_2. The most widely implemented technology is the pulse oximeter. This is an SO_2 measurement device used in hospitals to estimate SO_2 of arterial blood, typically on the finger. Absorbance is typically measured via the transmittance of 660 nm and 940 nm [30]. Pulse oximeters are simple tools for monitoring blood oxygen, however these devices only provide a bulk metric for overall SO_2.

The imaging of SO_2 is the process of providing functional metrics of SO_2 within the context of vascular structure. This has high value for the determination of tissue health and disease pathology by enabling irregularities to be identified in specific locations or vascular structures. This review of current literature focuses on SO_2 vascular imaging modalities, which can be broadly separated into scattering-based and absorption-based approaches. Absorption-based techniques can be further separated into radiative and non-radiative approaches.

2.4.1 Scattering-based SO_2 Imaging Modalities

First, we examine approaches that rely on the scattering of light to determine contrast. Fundus photography is a technique limited to ophthalmology, whereas hyperspectral imaging and visible optical coherence tomography (vis-OCT) have a variety of applications.

Fundus Photography

The first report of human retinal SO_2 was demonstrated in 1959 by Hickman et al., who implemented the simultaneous exposure of two wavelengths of light for fundus photography

[31]. This approach determines SO_2 through the optical density ratio of images at two wavelengths. The optical density is calculated by measuring the brightness of an image inside a vessel, and just outside a vessel, using the assumption that the difference in brightness is due to absorption.

The use of fundus photography for retinal oximetry has been implemented into two commercial products, the Imedos Vesselmap (Imedos Systems GmbH, Jena Germany) and the Oxymap T1 (Oxymap ehf, Reykjavik, Iceland) [11]. Figure 2.3 illustrates an example of retinal SO_2 imaging using the Oxymap T1. These approaches have been used in a number of clinical research studies such as studies on glaucoma [32] and diabetic retinopathy [33], however widespread adoption has been limited. Factors which have been shown to impact the accuracy of these SO_2 measurements, such as retinal and choroidal pigmentation, linear blood flow velocity and vessel size [11]. Fundus photography is a non-contact, label-free, image-based approach, however it is limited in clinical adoption due to the accuracy of SO_2 measurement.

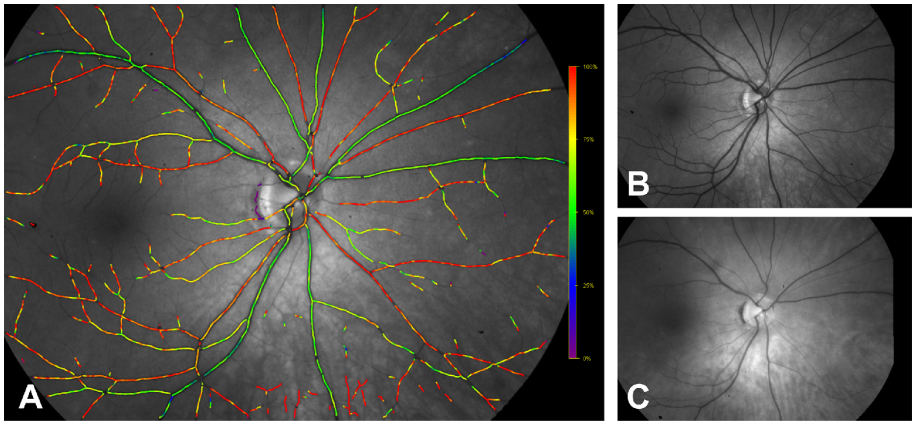


Figure 2.3: Oxymap T1 fundus photography for retinal oximetry. (A) illustrates the mapping of SO_2 onto vessels, (B) is the isosbestic fundus image captured at 570 nm and (C) is the non-isosbestic 600 nm fundus image. This figure is courtesy of Garg et al. [11] and made available through a Creative Commons Attribution 4.0 International license.

Hyperspectral Imaging

Building upon the dual wavelength approach used in pulse oximeters and fundus photography, hyperspectral imaging (HSI) approaches rely on the same principles for SO_2 determination. However, HSI uses a continuous spectrum of light rather than only two

wavelengths. Consequently, this approach is limited by many of the same artifacts of fundus photography [11]. HSI approaches rely on large volumes of data which are time-intensive to process and limit clinical translation since bio-markers cannot be displayed in real-time [28]. Vascular mapping of SO_2 has been demonstrated with HSI in the retina [34][35] and to assess vasculature surrounding tumors [36][37]. While this approach has been used in smaller studies, it continues to be limited in clinical adoption [28].

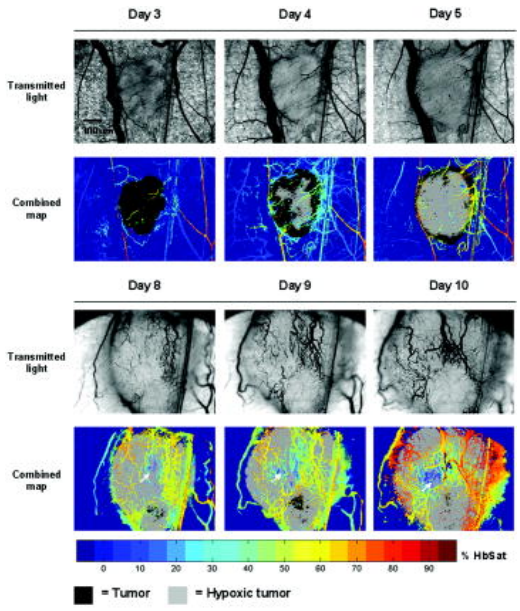


Figure 2.4: Functional HSI of tumor vasculature in a mouse. Fluorescence determines the hypoxia of the tumor. This figure is courtesy of Sorg et al. [36] and is used with permission.

A benefit of hyperspectral imaging is the capability of capturing fluorescence in addition to reflectance, depending on the configuration of the imaging system. Blood has a low quantum yield, such that it tends towards non-radiative relaxation. Work by Sorg et al. shown in Figure 2.4 leveraged hyperspectral imaging to capture both SO_2 vascular maps with reflectance, and fluorescent tumor structure labelled with exogenous dyes [36]. The simultaneous capture of SO_2 and surrounding bio-molecules, or a tumor, has high value in providing context for SO_2 irregularities when applied for disease monitoring and diagnosis.

Visible OCT

Optical Coherence Tomography (OCT) is a widely-adopted imaging technique that has become standard in the field of ophthalmology [11]. Through the use of low-coherence interferometry, OCT can capture three-dimensional structural images of tissue with fine lateral and axial resolution using a broadband light source. Commercial OCT systems predominately use superluminescent diodes (SLD) in the near-infrared (NIR) spectral range due to the deep penetration depth and availability of these light sources [38].

While NIR illumination is widespread, the use of visible light for OCT (vis-OCT) illumination using a supercontinuum (SC) light source is an emerging area of research. Biological tissues generally have higher scattering in the visible spectra compared to NIR. Vis-OCT can achieve higher imaging contrast, but is limited in penetration depth [38]. The primary area of research for vis-OCT is retinal oximetry due to the absorption of hemoglobin in the visible spectra [20][39][40][41]. An example of vis-OCT for retinal oximetry is shown in Figure 2.5. This technique has also demonstrated metabolic rate of oxygenation (MRO_2) by combining blood flow metrics with SO_2 in *in vivo* mouse retina [42].

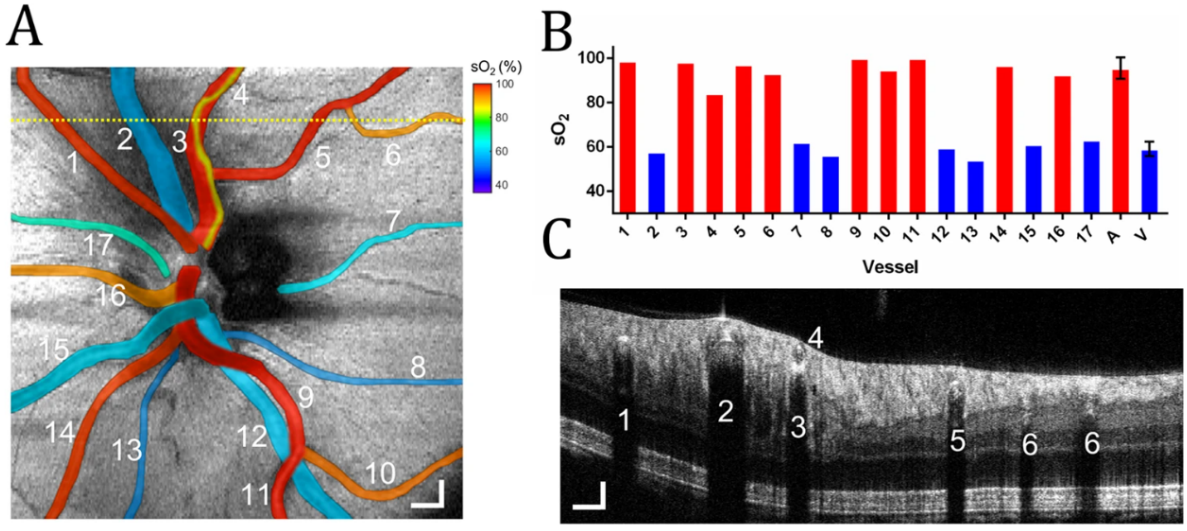


Figure 2.5: Vis-OCT oximetry map of the optic disk in a human retina. (A) illustrates a pseudo-coloured oximetry map, (B) the SO_2 measurement of arteries (red) and veins (blue) and (C) a B-scan located at the yellow dashed line in (A). This figure is courtesy of Rubinoff et al. [20] and made available through a Creative Commons Attribution 4.0 International license.

Earlier iterations of this technique were limited to major arteries and veins as smaller capillaries lack the blood volume required for the sufficient attenuation of scattering contrast [38], which is used to quantify absorption. However, recent works have demonstrated micro-vascular oximetry in capillaries using vis-OCT angiography (vis-OCT-A) in mouse ear [43], as well as rat [44] and human retina [45]. OCT angiography relies on the movement of red blood cells in successive images to localize and map capillaries [46]. As a result, vis-OCT-A is unable to detect small vessels and capillaries with no blood flow. Ocular vascular occlusive disorders are a common cause of visual disability [47]. Many of these disorders lead to ischemia and capillary non-perfusion, such that areas within the capillary system lose blood flow [48]. This has potential to limit vis-OCT-A for SO_2 measurement in areas of retinal non-perfusion where RBCs maybe be present, but not flowing.

2.4.2 Radiative SO_2 Imaging Modalities

Radiative contrast is absorption-based and occurs when absorbed optical energy is released in the form of a photon. This process is broadly referred to as radiative relaxation. These modalities can either rely on fluorescence or non-linear multi-photon interactions. Another form of absorption-based contrast is derived from non-radiative relaxation, which occurs through the dissipation of heat. This will be discussed in the subsequent section.

Photoluminescence Imaging

Recent work by Fang et al. [49] has demonstrated dynamic vascular mapping of SO_2 in tumors using photoluminescence imaging in the second near-infrared (NIR-IIb) window, ranging from 1,500 nm - 1,700 nm. In this range, autofluorescence (the fluorescence of biological tissue) is eliminated and light scattering is reduced, making this approach well-suited for deep-tissue imaging.

Briefly, this approach uses a nanoprobe that has varying emission properties based on the SO_2 of blood. This nanoprobe is injected intravenously and excited using 650 nm and 980 nm lasers. Radiative relaxation generates luminescence at 1,550 nm, which is detected for both excitation wavelengths to determine SO_2. This approach is capable of video rate imaging of dynamic SO_2 which is demonstrated in Figure 2.6. While this approach is non-invasive, it is limited by the requirement of intravenous injections to label oxy- and deoxy-hemoglobin [49].

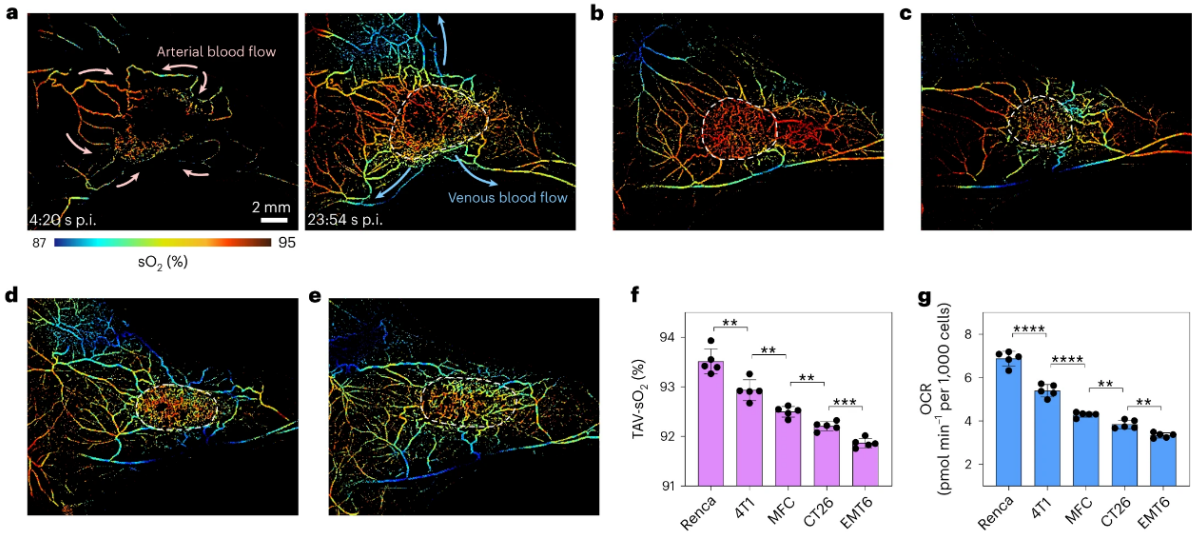


Figure 2.6: *In vivo* SO_2 photoluminescence imaging of various tumor models. (a) shows time-course dynamic SO_2 imaging of tumor vasculature, and (b) - (e) shows SO_2 imaging of vasculature surrounding various tumor types. This figure is courtesy of Fang et al. [49]. Reproduced with permission from Springer Nature.

Multi-Photon Imaging

Multi-photon imaging requires the non-linear interactions of more than one photon with a bio-molecule for sensing and imaging. Two-photon phosphorescence lifetime microscopy (2PLM) requires the injection of oxygen-sensitive exogenous dyes to measure local oxygen levels and offers sub-micron resolution [50]. This approach is largely applied to image microvasculature in the brain [51][52]. Limitations include the long phosphorescence lifetimes, which cause slow imaging speeds as well as the requirement for exogenous dyes [50].

Label-free multi-photon SO_2 imaging was recently demonstrated in zebrafish (see Figure 2.7) by Ferrer Ortas et al. [53] using third-harmonic generation (THG) and third-order sum frequency generation (TSFG) simultaneously at several emission wavelengths. Spectroscopic images are generated through the electronic resonance of the excited hemoglobin molecule in order to un-mix concentrations of oxy- and deoxy-hemoglobin [53]. This is a novel approach with interesting potential for future investigation. A limiting factor in the clinical feasibility of this approach, as well as other multi-photon methods, is the use of femtosecond lasers which are highly cost-prohibitive and limited in availability [54].

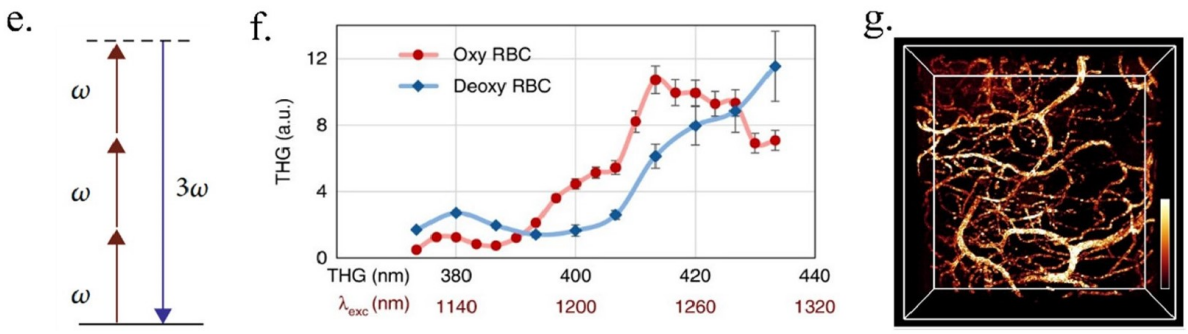


Figure 2.7: Multi-photon label-free *in vivo* colour third-order blood oxygenation in adult zebrafish brain by Ferrer Ortas et al. [53]. Figure is adapted with permission from Rathbone et al. [50]. Copyright 2024 American Chemical Society.

2.4.3 Non-Radiative SO_2 Imaging Modalities

Non-radiative techniques are absorption-based, wherein the relaxation of absorbed optical energy occurs through the dissipation of heat. This leads to photothermal or photoacoustic effects which are used to determine contrast.

Photoacoustic Imaging

Photoacoustic imaging (PAI) leverages short laser pulses to excite absorbers in tissue such as hemoglobin. Through non-radiative relaxation, the absorbed energy is converted to heat, and thermoelastic expansion produces acoustic waves. PAI captures acoustic waves with an ultrasonic transducer, which requires contact with the sample [28][11]. Acoustic waves are less scattered in tissue than light, thus PAI retains a high resolution in both the ballistic and diffuse optical regimes [55]. The primary architecture for PAI SO_2 imaging is the implementation of two [56][57] or more [58][59][60] excitation wavelengths chosen with at least one wavelength at an isosbestic point to determine SO_2. Recent work has demonstrated the capability of using a single excitation wavelength in an architecture which exploits linear and non-linear responses of absorbers through the Grüneisen-relaxation effect [61]. PAI for SO_2 vascular mapping has been demonstrated *in vivo* in various applications such as imaging the intestine [62], brain [56], and retina [63] as well as imaging the vasculature surrounding tumors [64][65]. SO_2 imaging of a mouse brain in states of normoxia and hypoxia is shown in Figure 2.8. PAI has also been used to demonstrate metabolic rate of oxygenation (MRO_2) which combines metrics of blood flow and SO_2 [65].

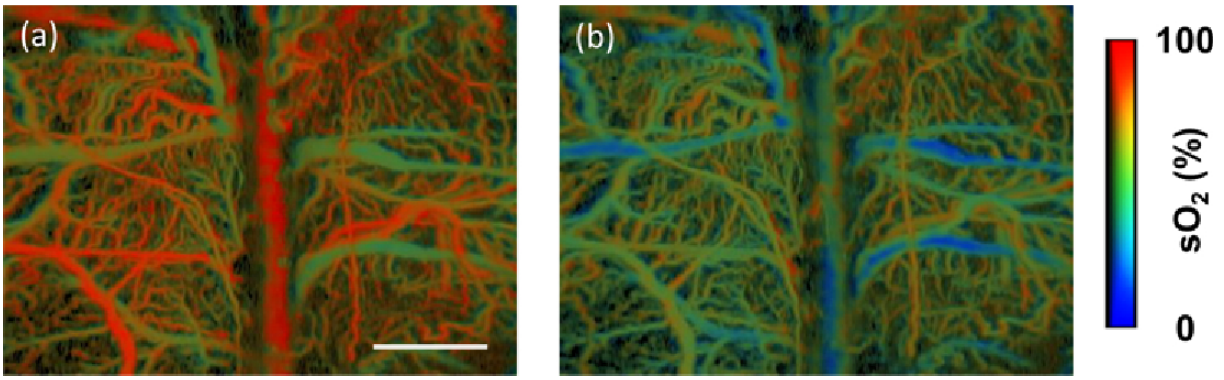


Figure 2.8: Photoacoustic imaging of a mouse brain in normoxia (a) and hypoxia (b). This figure is courtesy of Zhong et al. [56] and made available through a OSA Open Access Publishing Agreement license.

A primary limitation of photoacoustics is the requirement for contact. This causes significant limitations for clinical adoption in ophthalmoscopy and for delicate tissues such as open wounds. Another challenge in PAI is 'spectral colouring', such that wavelength-dependant distortions in fluence can occur due to the nature of light propagation in tissue [28]. This is particularly prevalent when imaging at depths beyond the optical diffusion limit of $\sim$1 mm in soft tissue. Overall, spectral colouring limits imaging depth and can ultimately confound the ability to un-mix HbO_2 and Hb [55]. Various research groups have explored the used of non-linear un-mixing methods and fluence correction to improve accuracy [59][22][66], however these methods have yet to be clinically validated [28].

Photoacoustic Remote Sensing

Previous work by the Photomedicine Labs explored the use of Photoacoustic Remote Sensing for SO_2 mapping. This is a non-contact, label-free technique which captures non-radiative relaxation for vascular imaging. Initial SO_2 results in chicken embryo (see Figure 2.9) [13] and rodent eye [67][14] have been demonstrated, however these results do not meet ISO standards for oximeter accuracy of a Root Mean Square (RMS) of $\leq 4\%$ [15].

The imaging system (shown in Figure 2.9) used stimulated Raman scattering (SRS) to generate excitation wavelengths of 532 nm, 545 nm, and 558 nm on a single excitation path. SRS is a non-linear process, which will be subsequently described in detail. A challenge of SRS is the pulse-to-pulse instability and overall power drift which can introduce variation in excitation pulse power throughout imaging [13].

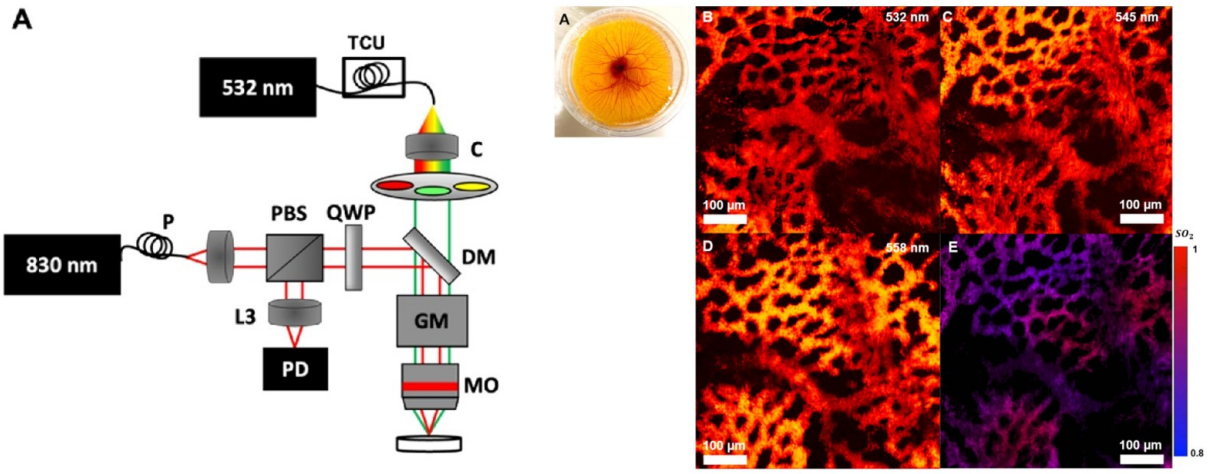


Figure 2.9: Photoacoustic remote sensing system (left) and images of chicken embryo vasculature (right). This figure is courtesy of Hosseinaee et al. [13] and made available through a OSA Open Access Publishing Agreement license.

2.5 Photon Absorption Remote Sensing

Photon Absorption Remote Sensing (PARS) is an all-optical, label-free and non-contact imaging modality which captures both radiative and non-radiative contrast simultaneously. The mechanisms for PARS contrast are summarized in Figure 2.10. An absorption event is caused by a focused, pulsed excitation source, the wavelength of which is selected to target a specific absorber. For example, ultra-violet (UV) excitation is used to target DNA in PARS histology systems [68][69] and green wavelengths are used to target hemoglobin excitation in PARS vascular imaging systems [70][14]. The absorbed energy (hv_{ex}) can be released through two primary mechanisms; radiative and non-radiative relaxation.

Radiative contrast (hv_{em}) is derived from the emission of photons in response to the absorption of optical energy. Radiative relaxation can be captured from a variety of mechanisms such as fluorescence or multi-photon fluorescence. Typically, the energy level of emitted photons is distinct from the optical energy which was absorbed [69]. To determine non-radiative contrast, a continuous wave detection source (I_{det}) is co-focused with the excitation source. Non-radiative relaxation involves the release of heat in response to absorbed optical energy. As described in PAI, sufficiently rapid excitation can result in thermoelastic expansion and the generation of acoustic pressures. Local modulation in temperature and pressure causes perturbations in detection scattering, denoted as $(\sigma_s + \delta\sigma_s)I_{det}$, enabling the non-contact detection of non-radiative relaxation [69]. In addition to absorption-based

contrast, PARS can also capture scattering from both excitation and detection sources. These contrasts are particularly valuable for system alignment and localization of the region of interest [70].

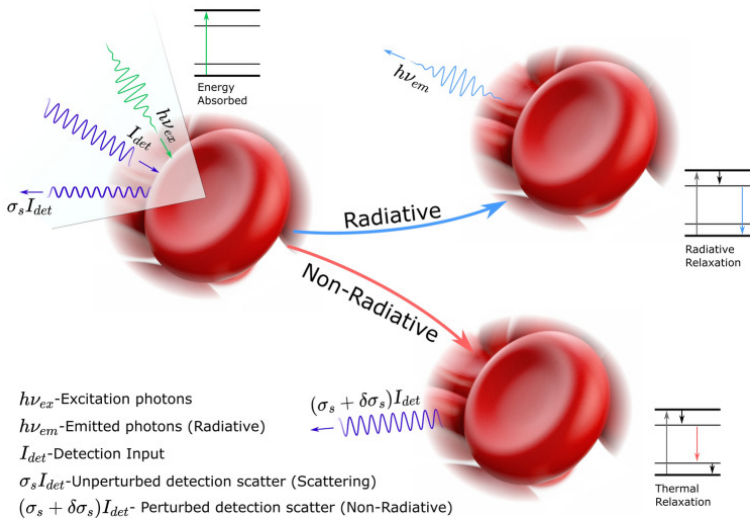


Figure 2.10: Diagram of the PARS Imaging Mechanism. An excitation photon is absorbed, and has two pathways for relaxation. Radiative relaxation occurs through the emission of a photon, typically at a lower energy level through mechanisms such as fluorescence. Non-radiative relaxation occurs through the local temperature and pressure modulations caused by heat dissipation. These modulations perturb the back scattering of the detection input. This figure is courtesy of Ecclestone et al. [69] and made available through a Creative Commons Attribution 4.0 International license.

Recent work by J. A. Tummon Simmons et al. has demonstrated the ability of PARS to capture unique *in vivo* images, as is demonstrated in Figure 2.11, which illustrates a mosaic image of vasculature in the chorioallantoic membrane (CAM) of a chicken embryo. System developments have also enabled video rate PARS imaging, which can capture red blood cells flowing through capillary vessels in a CAM [70].

The capability for simultaneous capture of radiative and non-radiative contrast enables images of vasculature to be localized within the context of surrounding bio-molecules. This is highlighted in images of *in vivo* mouse ear (shown in Figure 2.12) which shows non-radiative vasculature contrast surrounded by radiative contrast from cartilage matrices and sebaceous gland [70]. Images demonstrated in Figures 2.11 and 2.12 are captured with a single green excitation source.

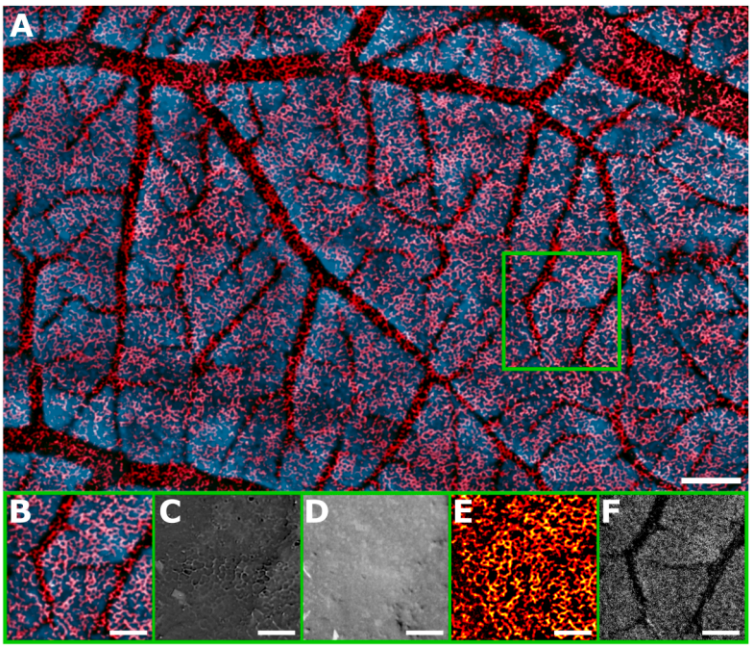


Figure 2.11: PARS composite images of *in vivo* CAM vasculature. (A) shows a composite image of radiative (blue) and non-radiative (red) contrast. (B) shows a zoomed in composite image of the area highlighted in (A). Detection scattering (C) and excitation scattering (D) demonstrate surface morphology. (E) shows the non-radiative contrast which highlights capillary vessels on the surface of the CAM. Radiative contrast in (F) illustrates the larger, deeper vessels which block radiative relaxation from sub-surface bio-molecules such as the yolk. This figure is courtesy of J. A. Tummon Simmons et al. [71] and made available through a Creative Commons Attribution 4.0 International license.

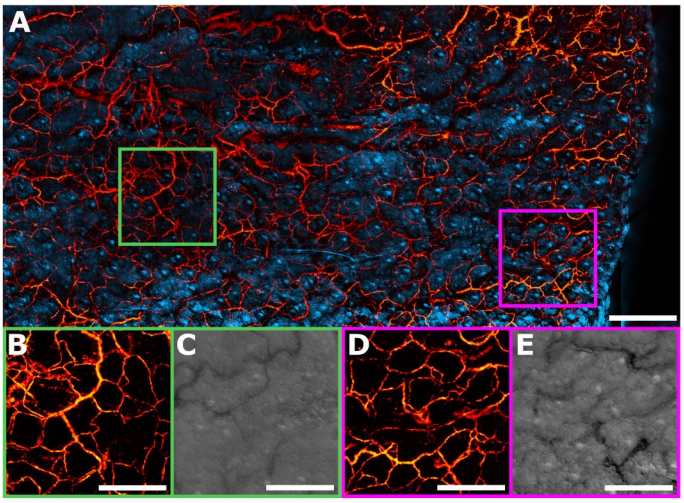


Figure 2.12: PARS images of an *in vivo* mouse ear. (A) shows a composite mosaic of radiative (blue) and non-radiative (red) contrast. (B) and (D) are zoomed in non-radiative contrast showing vasculature. (C) and (E) show radiative contrast highlighting cartilage matrices and sebaceous glands. This figure is courtesy of J. A. Tummon Simmons et al. [71] and made available through a Creative Commons Attribution 4.0 International license.

This work explores the addition of a secondary excitation wavelength to enable the determination of SO_2 using PARS, which provides a unique platform for SO_2 vascular imaging. First, radiative contrast provides important context of surrounding bio-molecules and structures. The eventual goal of SO_2 imaging is to be used in the detection and localization of irregular SO_2 for the diagnosis and treatment of disease. Determining SO_2 within the context of surrounding bio-molecules, highlighted with radiative contrast, has potential to provide valuable information to clinicians and researchers regarding disease mechanisms and pathology. Another advantage of PARS is that non-radiative vascular contrast is derived directly from the absorption of hemoglobin. Unlike vis-OCT-A, which requires the motion of RBCs to determine capillary vessels, PARS does not require motion. This enables absorption contrast to be obtained in occluded vessels. This is valuable as many disease states cause capillary non-perfusion, ischemia and vascular occlusion. Finally, PARS does not require contact with a transducer, as is the case with PAI. This is valuable when imaging delicate tissues such as the eye and open wounds.

2.6 Stimulated Raman Scattering

Stimulated Raman Scattering (SRS) is a non-linear phenomena used in this work to generate a secondary excitation wavelength. This approach has also been used in photoacoustics [62][59][60] and photoacoustic remote sensing [67][14][13] to generate additional wavelengths. The reliability of this excitation source is critical for successful *in vivo* imaging and quantitative measurements, which are required for SO_2 imaging. As a result, it is worthwhile to examine the underlying mechanisms of SRS in order to maximize performance of the secondary excitation wavelength.

2.6.1 Raman Scattering

The Raman effect is the transfer of power from one optical field to another through the vibrational modes of a molecular medium. This can occur through spontaneous and stimulated Raman scattering which is illustrated in the Jablonski diagram in Figure 2.13.

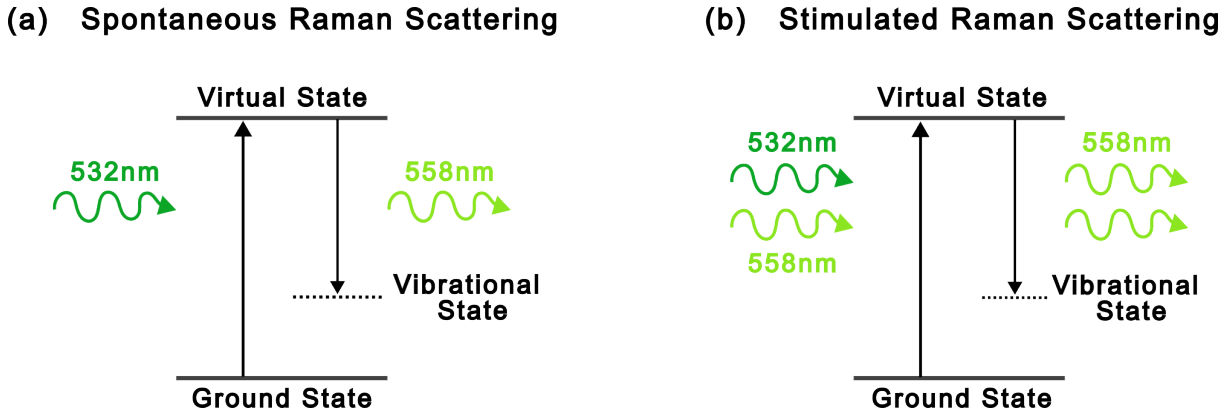


Figure 2.13: Jablonski diagram of spontaneous and stimulated Raman scattering.

From a quantum-mechanical perspective, spontaneous Raman scattering occurs when incident light (referred to as the pump) interacts with a molecular medium and excites the molecule to a virtual state. During relaxation, the molecule does not return to the ground state, but instead relaxes to a vibrational state by generating a Stokes photon that is radiated at a down-shifted frequency. Stimulated Raman scattering (SRS) follows the same process, with the exception that SRS occurs when both a pump and Stokes photon interact with a molecule, generating a higher number of output Stokes photons.

The generated Stokes photon is co-polarized with the pump photon for both spontaneous and stimulated Raman scattering [72].

The primary difference between spontaneous and stimulated Raman scattering is the rate of photon generation. If ω_1 represents the pump frequency, n_1 the number of pump photons, and ω_2 the Stokes frequency with n_2 as the number of Stokes photons, the rate of spontaneous (W_{spon}) and stimulated (W_{stim}) emissions can be represented by the expressions in 2.6 and 2.7. Spontaneous Raman scattering occurs when there are no photons in the ω_2 frequency, such that $n_2 = 0$ and $n_1 \gg 1$, whereas stimulated Raman scattering occurs when n_1 and $n_2 \gg 1$ [73]:

$$W_{spon} \propto n_1 \tag{2.6}$$

$$W_{stim} \propto n_1(n_2 + 1) \tag{2.7}$$

This can be summarized by the follow relationship [73]:

$$\frac{W_{stim}}{W_{spon}} \propto n_2 + 1 \tag{2.8}$$

This demonstrates that the presence, and increased number, of Stokes photons increases the subsequent generation of more Stokes photons. This causes stimulated Raman scattering to occur at a much higher rate than spontaneous Raman scattering when Stokes wavelengths are present [73].

2.6.2 Raman Gain

The difference between the frequency of the pump and Stokes depends on the spectrum of Raman gain. This is defined by the molecule with which the incident light is interacting. In most molecular media, Raman gain only occurs at specific frequencies. However, the fused silica in optical fibers is amorphous and non-crystalline. This creates a continuum wherein the frequencies extend over a broad range as a result of overlapping molecular vibrational frequencies which spread into overlapping bands. Within the Raman gain spectra, a maximum of gain occurs for frequencies which are 13.2 THz downshifted from the pump frequency. Co-polarization of the pump and stokes maximizes Raman gain, whereas orthogonal polarization significantly reduces gain [72].

2.6.3 Raman Threshold

In order for SRS to be observed, high power levels are required to achieve sufficient photon density to initiate the Raman effect. As input power is increased, the output power is converted from pump to Stokes. This conversion is near-exponential when the Raman threshold has been met. The Raman threshold is defined as the input pump power which causes the power of the output pump to equal to the power of the output Stokes. Theoretically, a complete conversion of power from pump to Stokes would occur, however in actuality, the Stokes wavelength then becomes the pump for a second-order Stokes wavelength. With enough power, SRS can cascade to generate multiple Stokes bands [72].

2.6.4 SRS Generation within A Fiber

There are various architectures to generate Stokes wavelengths using SRS, and this can be accomplished with or without an input Stokes beam. This work does not use an input Stokes beam, therefore subsequent explanation focuses on the pump-only architecture. The input pump and SRS generation is considered to be within a quasi-continuous regime for a pulse width range of 1-100 ns [72], which encapsulates the pulse width used in this work.

When a pump beam is launched into the input of a fiber without a Stokes beam, spontaneous Raman scattering must occur to provide the initial seed from which to initiate SRS. Any frequency within the Raman gain spectrum can be generated by spontaneous Raman scattering, however the frequency at which Raman gain peaks (13.2 THz downshifted from the pump) is maximized. These Stokes photons feed into SRS, and when the Raman threshold is met or surpassed, the maximized Stokes frequency increases exponentially [72]. In the case of a 532 nm pump, the frequency which is downshifted by 13.2 THz, and is therefore maximized, is 545 nm. With enough input power, the 545 nm Stokes then becomes the pump for a second-order Stokes wavelength at 558 nm.

2.6.5 Polarization and SRS

Polarization plays a critical role in the efficiency of SRS and Stokes wavelength generation. If polarization is not maintained throughout the fiber length, the relative polarization between the pump and Stokes can become scrambled, reducing Raman gain by a factor of two. This occurs because Raman gain is maximized when the Stokes and pump are co-polarized, and substantially reduced when the pump and Stokes are orthogonal [72]. Polarization-maintaining (PM) fibers are used to avoid scrambling throughout the fiber length and maximize the Raman gain.

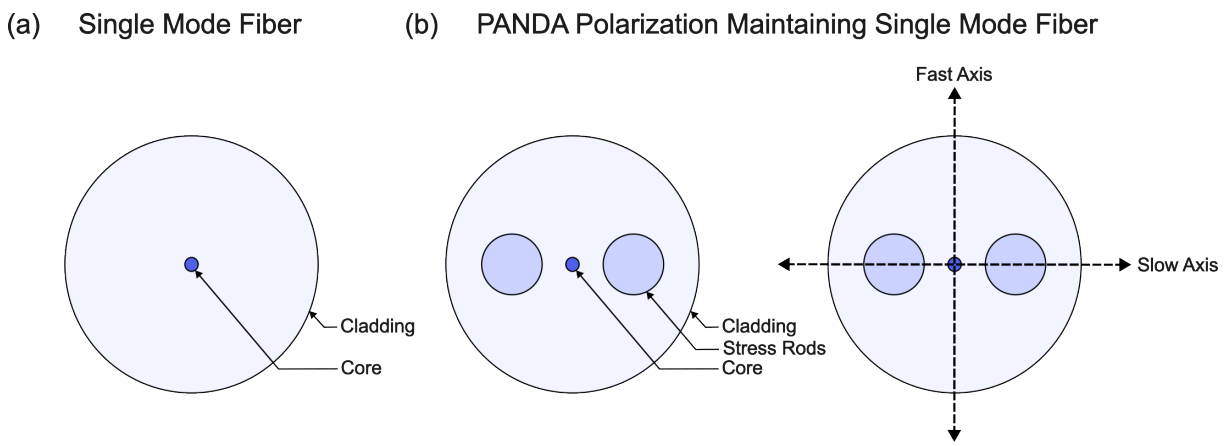


Figure 2.14: Diagram comparing the structure of single mode and PANDA polarization-maintaining single mode fiber.

Polarization-Maintaining Fibers

A single mode optical fiber has both a core and a cladding as shown in Figure 2.14. In an ideal case, the polarization state of incoming light would be unchanged as light propagates through the fiber. However, temperature, mechanical stress and imperfections in the fiber can impact the polarization state. To combat this, polarization-maintaining (PM) fibers are used. A common type of PM fiber is created in a PANDAS architecture. This approach uses two stress rods which run down the length of the fiber and are situated at 180 degrees from one another (see Figure 2.14), creating strong birefringence. The stress applied in one axis increases the refractive index, this creates a slow axis. Orthogonal to the slow axis, the axis without the stress rods has the lowest stress and lowest refractive index, and thus becomes the fast axis [74][75].

In a PM fiber, the polarization state of linearly polarized light is maintained when light is coupled exclusively into either the fast or slow axis as shown in Figure 2.15. This ensures that light only interacts with the refractive index of one axis, and will maintain polarization despite factors such as mechanical stress from bends and twists in the fiber [74]. Unpredictable and non-linear output polarization occurs if light is not properly coupled into one of the two axis. With incorrect alignment, the polarization becomes susceptible to changes in external temperature and mechanical stress, creating an unstable polarization state. In order for the output polarization of a fiber to be maintained throughout the fiber length and remain predictable, light must be entirely coupled into either the fast or the slow axis [74].

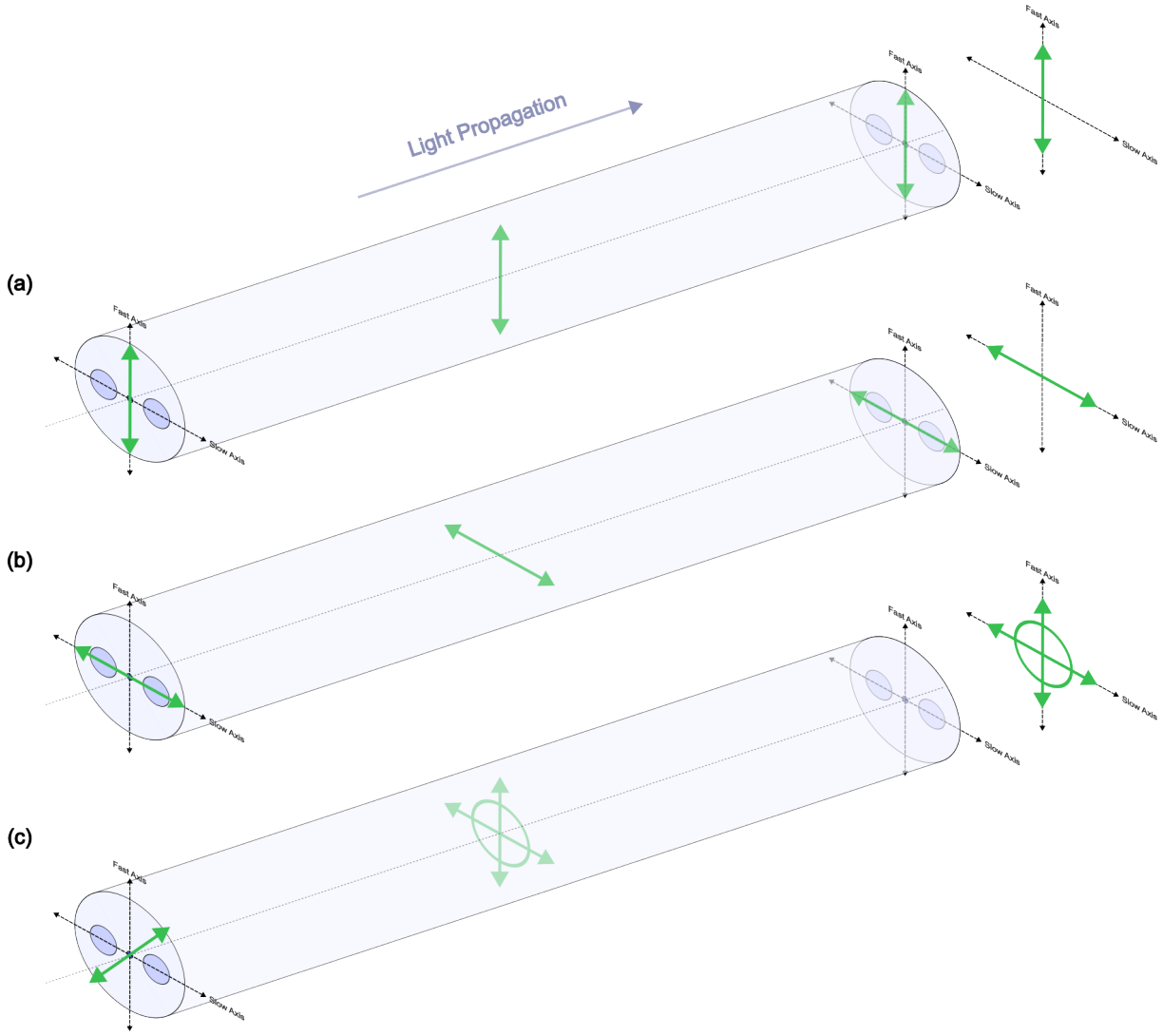


Figure 2.15: Light propagation in a polarization-maintaining fiber. (a) illustrates linearly-polarized light aligned into the fast axis, which maintains polarization at the output of the fiber. (b) shows the same maintenance of polarization when aligned to the slow axis. (c) illustrates that when the input polarization is not aligned to either axis, the output polarization state becomes unpredictable and unstable.

Half Wave Plate

Half wave plates (HWP) are used to align the polarization of light into the correct axis of a PM fiber. These devices are also made of birefringent material and have a fast and slow axis which results in a phase shift in the optical field [76]. When interacting with linearly polarized light, a HWP rotates the light such that it remains linear but is rotated with respect to the input beam. The angle between the input polarization and the optical axis of the half wave plate is represented by θ, and the angle between input and output polarization is 2θ as shown in Figure 2.16 [77]. Rotating the optical axis of the HWP enables the angle of the output polarization to be adjusted.

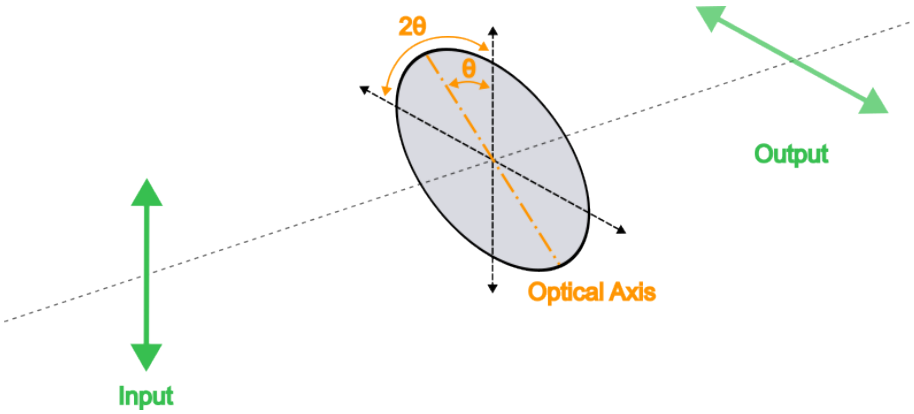


Figure 2.16: Half-wave plate (HWP) diagram and the effect on linearly-polarized light.

2.7 Conclusion

This chapter defines key terminology used within this work, and discusses other approaches which have been implemented for SO_2 imaging. PARS is described as an absorption-based, non-contact, label-free imaging platform that can derive signal from capillaries and larger vasculature without the requirement of blood flow. Additionally, PARS simultaneously captures non-radiative and radiative contrast, which provides valuable information on the bio-molecules and structures within vascular networks. This project focuses on improving the consistency and reliability of *in vivo* multi-wavelength PARS imaging. These efforts work towards the goal of accurate SO_2 imaging using PARS. SRS mechanisms are described to provide context for system developments which improve the performance and reliability of the second excitation wavelength generation.

Chapter 3

Multi-Wavelength *in vivo* PARS System

3.1 Introduction

This chapter presents the developments of the first *in vivo* multi-wavelength PARS imaging system, which builds off the existing single excitation system implemented by J.A. Tummons Simmons et al. [70]. New developments include pulse-specific power compensation to manage the effects of excitation source fluctuations and two independent excitation paths. Adding a secondary independent excitation path enables co-aligned, near-simultaneous multi-wavelength PARS contrast. The secondary excitation wavelength is generated using stimulated Raman scattering (SRS), and polarization alignment is implemented to maximize Raman gain and improve Stokes wavelength generation. These technical developments work towards consistent and reliable multi-wavelength *in vivo* PARS images. Reliability and consistency is crucial when taking the ratio of non-radiative images to determine SO_2. This requires that the same vessel structures can be captured by both wavelengths and that multiple PARS images can be acquired at the same location throughout the course of an experiment. These experiments will be explored in Chapter 5 and 6. The presented imaging system implements polarization alignment, independent excitation paths, and power compensation which lays the groundwork for SO_2 imaging and works towards a PARS oximeter system that achieves ISO accuracy standards [15].

3.2 Background

3.2.1 Excitation Wavelength Selection

The absorption of oxy- and deoxy-hemoglobin varies across the visible range, as shown in Figure 3.1. As discussed previously, the measurement of SO_2 leverages this phenomenon by determining the change in absorption across various wavelengths. The most common SO_2 determination paradigm leverages the ratio of absorption of two or more wavelengths. At least one wavelength is typically chosen at an isosbestic point where the absorption is the same, and another is chosen at a non-isosbestic point where the absorption differs [56][57][60][59][78].

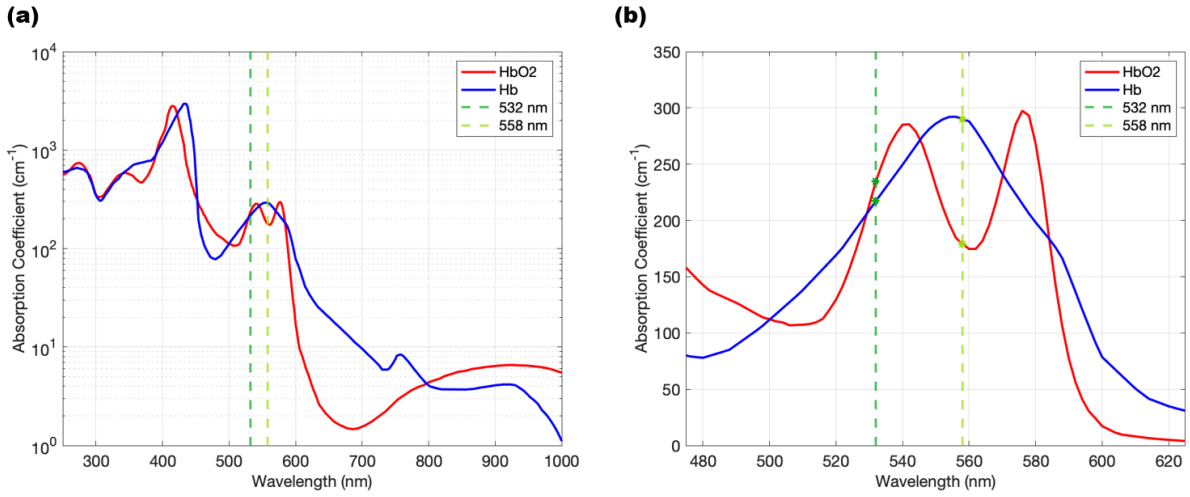


Figure 3.1: Absorption spectra for oxy-hemoglobin (HbO_2) and deoxy-hemoglobin (Hb), full range (a) and zoomed in (b). Original data source complied by Scott Prahl [26]

PARS requires the use of a nano-second or smaller pulse width laser source with a high repetition rate. This limits the commercial availability of lasers at idealized wavelengths for this work. 532 nm is a near-isosbestic wavelength (see Figure 3.1) which is commercially available and meets PARS laser requirements. As a result, a 532 nm source is used as the isosbestic wavelength. Through stimulated Raman scattering (SRS), wavelengths of 545 nm and 558 nm can be generated using a 532 nm excitation (pump) source [72][60]. 558 nm is a strong non-isosbestic point, thus this wavelength is used as the second excitation source. The combination of 532 nm and 558 nm wavelengths have been implemented in photoacoustic [56][57][62] and photoacoustic remote sensing SO_2 systems [14][13][67].

3.2.2 Generating 558 nm with Stimulated Raman Scattering

SRS is a useful approach to generate a 558 nm excitation source, however, it is not without challenges. The main challenges addressed in this work include maximizing Raman gain and managing the instabilities and transients in power.

As discussed in Chapter 2, Raman gain is closely tied to the polarization alignment into a PM fiber [72]. In order to generate sufficient 558 nm excitation power for *in vitro* and *in vivo* experiments, the Raman gain must be maximized. This is accomplished using a half-wave plate (HWP) to align into the PM fiber.

The temperature of the fiber impacts the stability of SRS, which was shown in previous work by our lab [13]. Temperature regulation is implemented using dry ice, however this does not entirely eliminate instabilities and transients of power. To further address this, power compensation is implemented by measuring incoming excitation pulses and compensating for variability in post-processing. Similar power compensation approaches have been used in PAI [57][79].

3.2.3 Independent Excitation Paths

PARS is a confocal imaging technique that requires lateral and axial alignment of spot sizes on the order of micrometers. If both excitation wavelengths are generated on the same excitation path, then chromatic aberrations and changes in alignment due to the changing of filters (used to select the excitation wavelength) cannot be mitigated. This impacts the ability for the system to image the same structures at the same depth for both 532 nm and 558 nm excitation. This work presents a multi-wavelength PARS *in vivo* system with separate excitation paths for 532 nm and 558 nm excitation. This enables independent alignment, improving consistency in images between both wavelengths. Additionally, no optical changes are required to switch between excitation wavelengths, enabling the implementation of interlacing 532 nm and 558 nm excitation pulses in order to generate near-simultaneous images in both wavelengths.

3.3 Methods

3.3.1 558 nm Excitation Generation

The 558 nm excitation source is generated through SRS using a 532 nm 1.5 ns pulsed ytterbium-doped fiber laser (GLPN-16-1-10-M, IPG Photonics) as the pump source. The

pump source is coupled through a 5 m polarization-maintain fiber (PM-460-HP, Thorlabs) and interactions within the silica of the fiber generate Stokes wavelengths [72]. To maximize SRS gain, a half wave plate (WPMH05M-532, Thorlabs) is used to align the 532 nm laser polarization to the principle axis of the fiber. A spectrometer (CCS200, Thorlabs) is used to measure the resulting Stokes wavelengths and validate the polarization alignment. To cool the fiber, ∼4 m of fiber is placed inside an isolation chamber with dry ice which maintains a temperature of 195 K to improve SRS stability [13]. This process generates Stokes wavelengths of 532 nm, 545 nm and 558 nm. The output of the fiber is bandpass filtered (FB570-10, Thorlabs) to isolate for 558 nm.

This filter (FB570-10, Thorlabs) has a center wavelength of 570 ± 2 nm for an angle of incidence (AOI) of 0°. Varying the AOI lowers the filter's center wavelength of peak transmission [80], enabling the passband to be tuned for 558 nm. The SRS of 558 nm is a high power operation that generates high power byproducts of 532 nm and 545 nm. While it is possible to purchase filters with a passband of 558 nm at an AOI of 0°, this would reflect 532 nm and 545 nm directly back into the fiber and will cause damage. As a result, a higher passband filter was implemented on an angle that was tuned using a spectrometer.

3.3.2 Optical System Architecture

558 nm Excitation System

The optical architecture for the PARS multi-wavelength *in vivo* system is illustrated in Figure 3.2. The 558 nm excitation source is generated as described above, and the PM fiber output is collimated (C20FC-A, Thorlabs), filtered (FB570-10, Thorlabs) to isolate for 558 nm, and the beam size is adjusted using a Galiean beam expander (GBE02-A, Thorlabs). This 558 nm excitation then enters the 50:50 power-based beam splitter which optically combines the 558 nm and 532 nm excitation paths.

532 nm Excitation System

The second excitation wavelength uses an identical 532 nm 1.5 ns pulsed ytterbium-doped fiber laser (GLPN-16-1-10-M, IPG Photonics) in a free-space configuration. A Galilean beam expander (GBE02-A, Thorlabs) is used to adjust beam size, and the 532 nm excitation is passed into a 70:30 power-based beam splitter (BS023, Thorlabs). This enables excitation back-scattering contrast to be captured for both 532 nm and 558 nm. The 532 nm excitation then also passes through the 50:50 beam splitter, combining this path with the 558 nm path.

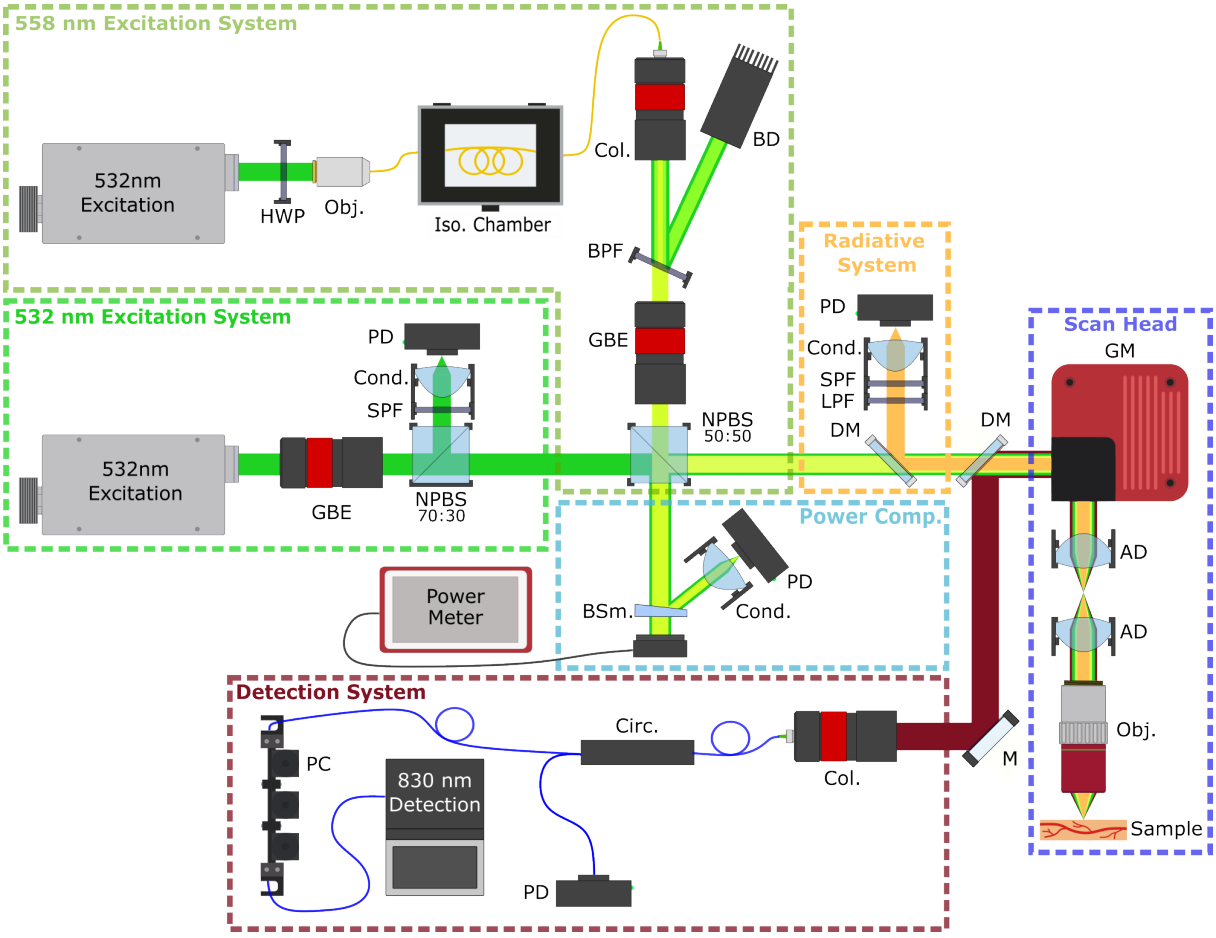


Figure 3.2: Multi-wavelength PARS *in vivo* system illustrating the 558 nm excitation (yellow-green), 532 nm excitation (green), detection (red) and radiative (orange) optical paths. Abbreviations for components are as follows: *HWP* half wave plate, *Obj.* objective lens, *Iso. Chamber* isolation chamber, *Col.* collimator, *BD* beam dump, *BPF* band-pass filter, *GBE* Galilean beam expander, *NPBS* non-polarizing (power-based) beam splitter, *BSm.* beam sampler, *Cond.* condenser lens, *PD* photodiode, *SPF* short-pass filter, *LPF* long-pass filter, *DM* dichroic mirror, *GM* galvanometer mirrors, *AD* achromatic doublet, *PC* polarization controller, *Circ.* circulator.

Power Compensation

The other output of the 50:50 beam splitter is used for power compensation by monitoring the incoming excitation for both 532 nm and 558 nm. A beam sampler (BSF10-A, Thorlabs) and photodiode (DET10A2, Thorlabs) are used to measure pulse-specific power for power compensation in post-processing. Additionally, an optical power meter (PM100D, Thorlabs) is used to match the power levels of 532 nm and 558 nm. Power meter measurements were calibrated with output pulse energy at the imaging head.

830 nm Detection System

The detection source is a 830 nm near-infrared (NIR) super-luminescent diode (SLD) laser (SLD830S-A20, Thorlabs). This is passed through a manual paddle polarization controller (FPC560, Thorlabs), a fiber circulator (VCIR-3-830-S-L-10-FA, Ascentta) and is collimated (C40APC-B, Thorlabs) before being optically combined with both excitation paths using a short pass dichroic mirror (DMSP605, Thorlabs).

Scan Head

A galvanometer mirror pair (GVS012/M, Thorlabs) optically scans the combined excitation and detection paths in a 2-dimensional raster pattern. A telecentric pair (AC254-050-AB-ML, Thorlabs) images the pivot point of the galvanometer mirror pair onto the pivot point of the 20x objective lens (Plan Apo NIR 20X, Mitutoyo) after which the excitation and detection paths interact with the sample.

Light Collection on the Back Path

On the back path, contrast is collected on three different photodiodes. First, detection scattering is captured before, during and after an excitation event on an avalanche photodiode (APD130A, Thorlabs). The back-scattered 830 nm light is directed onto the photodiode by reflecting off the dichroic mirror, coupling back into the fiber and is then re-directed by the circulator. This enables the capture of detection scattering contrast (before the excitation event) as well as the non-radiative contrast. The excitation event causes perturbations in detection scattering during and after the excitation event due to local temperature and pressure modulations.

Radiative contrast passes through the 805 nm dichroic mirror and is reflected off the 605 nm dichroic mirror (DMSP605, Thorlabs), and is filtered to avoid bleed-through of detection and excitation wavelengths. This radiative contrast is condensed (ACL25416U-A, Thorlabs) and captured on another avalanche photodiode (APD130A, Thorlabs). Finally, back-scattered light from both the 558 nm and 532 nm excitation wavelengths are condensed (ACL25416U-A, Thorlabs) and collected on a photodiode (PDB425A, Thorlabs) to capture excitation scattering.

3.3.3 Imaging System Characteristics

When imaging *in vivo*, a larger depth of focus is advantageous to accommodate for surface irregularities and motion. When an objective aperture is fully filled, a lower numerical aperture and lower collection angle are associated with a larger depth of focus. However, having a high numerical aperture benefits a PARS system by increasing the collection angle of back-scattered light. To accommodate for these competing requirements, a 20x objective is under-filled in order to achieve a large depth of focus without sacrificing the collection angle of the objective. A result of under-filling the objective is that the experimental resolution of the system is substantially larger than the theoretical resolution.

When under-filling an objective, the beam diameter of the collimated light going into the objective determines resolution (spot size) measured in meters. A beam profiler (BladeCam2-XHR, DataRay) was used to measure beam diameter. To experimentally measure resolution, the Gaussian line spread function of a USAF 1951 resolution target is used to determine a measurement of the full width half maximum (FWHM). This work uses the full-width at $1/e$-maximum as the definition for spot size ($2W_0$). Equation 3.1 is used to convert FWHM spot size ($2W_{FWHM}$) to full-width at $1/e$-maximum spot size ($2W_0$) [81]. The spot size ($2W_0$) is the diameter of the beam at its narrowest point and is defined as twice the beam waist (W_0).

$$2W_0 = \frac{1}{\sqrt{ln2}} \cdot 2W_{FWHM} \tag{3.1}$$

Depth of focus (DOF) of a system is not easily measured, thus a theoretical approximation is calculated using Equation 3.2 [81]. The depth of focus is defined as twice the Rayleigh range (z_0), where the Rayleigh range is the axial distance between the beam waist (W_0), which occurs at the narrowest point of the beam, and $\sqrt{2}W_0$ [81]. The wavelength of light (λ), beam waist (W_0) and Rayleigh range (z_0) are measured in meters.

$$DOF = 2z_0 = \frac{2\pi W_0^2}{\lambda} \tag{3.2}$$

The experimental beam diameter and resolution, as well as the theoretical depth of focus for all wavelengths are shown in Table 3.1. All wavelengths achieve close to 3 μm in spot size, however there are discrepancies in resolution. This is due to precision limitations of optomechanics when manually adjusting beam sizes from three separate laser sources. Depth of focus depends on both resolution and wavelength, thus variation will occur across wavelengths when resolution is matched. It is useful to have a theoretical approximation of depth of focus when interpreting results.

Wavelength	Beam Diameter	$2W_{FWHM}$	Spot Size ($2W_0$)	Depth of Focus ($2z_0$)
830 nm	1.504 mm	2.54 μm	3.05 μm	17.62 μm
532 nm	1.499 mm	2.47 μm	2.97 μm	25.99 μm
558 nm	1.420 mm	2.26 μm	2.71 μm	20.74 μm

Table 3.1: Experimental beam width, resolution, and theoretical depth of focus.

3.3.4 Interlacing and Image Extraction

In vivo studies present the challenge of imaging a target which is subject to bulk motion and heartbeat motion. In order to capture PARS images from two excitation wavelengths of the same vascular structure, excitation pulses of 532 nm and 558 nm were interlaced, such that the system alternated between 532 nm and 558 nm for each point in the raster-scanned of an image.

The 532 nm and 558 nm PARS images are separated in post-processing and image reconstruction. Engineering work for the interlacing of excitation pulses, including data acquisition software and imaging system control as well as the post-processing separation of 532 nm and 558 nm and image extraction, was implemented by James A. Tummon Simmons, and is described in this thesis solely to provide context for presented results.

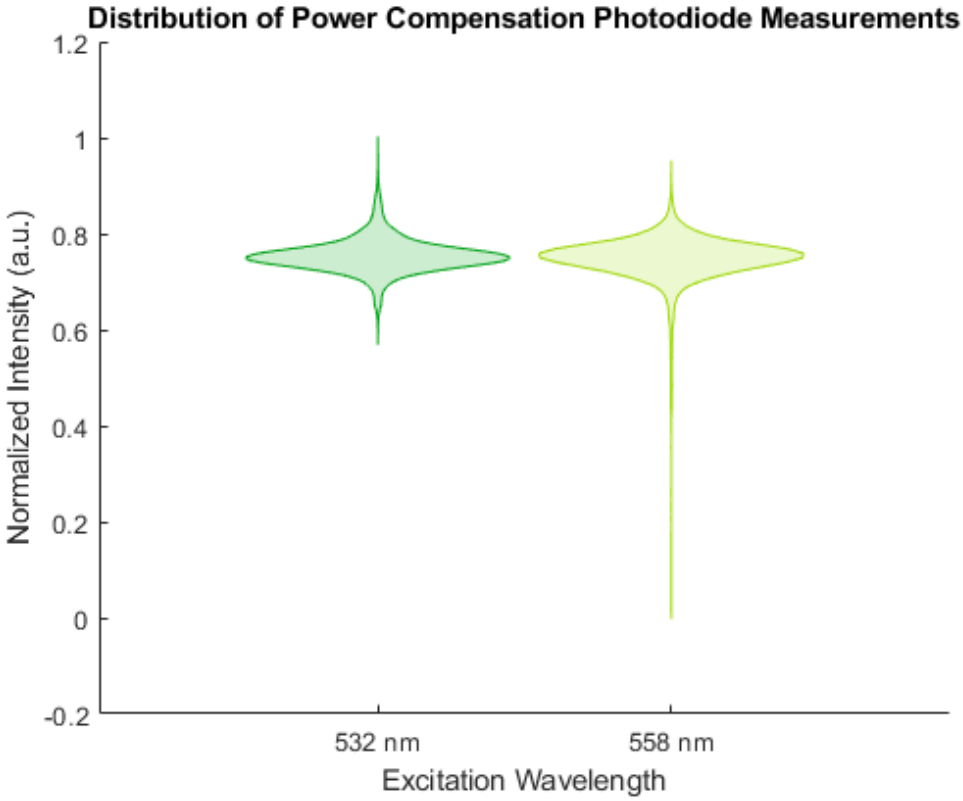


Figure 3.3: Comparison of the distribution of power compensation measurements of incoming excitation pulses for 532 nm and 558 nm across 3 independent experiments, containing 23 datasets total, each with 2,375,501 data points. The standard deviation (σ) shows variability for 532 nm ($\sigma = 0.0355$) and 558 nm ($\sigma = 0.0505$).

3.4 Results & Discussion

3.4.1 Power Compensation

SRS can cause instabilities and transients in power across an imaging session and a single data acquisition. While measures such as fiber cooling and polarization alignment are implemented to improve stability, fluctuations are not entirely eliminated. In cases such as SO_2, which require quantitative metrics, the impact of these fluctuations must be removed in order to achieve accurate non-radiative ratios between 532 nm and 558 nm excitation. It is critical that changes in measured SO_2 are due to physiological changes in true SO_2, not

fluctuations in laser source power. As a result, a power compensation photodiode measures incoming excitation pulses, as shown above in Figure 3.2, and is used to compensate for power fluctuations by re-scaling individual non-radiative signals in post processing.

The power compensation photodiode captures the intensity of incoming light for both 532 nm and 558 nm excitation. The variability of these two wavelengths is illustrated in Figure 3.3, wherein the distribution of normalized intensity data is displayed in a violin plot. This data is captured from three different experiments, all of which occurred on different days, by the same operator with the same equipment. The fiber coupling was re-aligned for each experiment.

Across the three experiments, the number of datasets in each are 11, 5, and 7. Each dataset contains 2,375,501 data points, each representing the intensity of a single excitation pulse. Standard deviation is represented by σ, and variability is present in both 532 nm ($\sigma = 0.0355$) and 558 nm ($\sigma = 0.0505$) excitation. However, the variability 558 nm is substantially larger as is shown in Figure 3.3. The large tail on the bottom of the 558 nm violin plot illustrates the tendency for 558 nm excitation intensity to decrease when power drift occurs, however fluctuations can cause an increase or a decrease in intensity. This variability in power highlights the importance of power compensation in the PARS multi-wavelength system, particularly for SRS generated excitation sources.

Figure 3.4 illustrates an extreme example of 558 nm fluctuations within a single data acquisition, which captured 7 sequential frames of static carbon fibers in mineral oil. In the first frame (a) the 558 nm excitation power was at a maximum, and then dropped substantially by frame 4 (b), as shown in (g). This results in a large difference in non-radiative signal from the same sample. The large absolute difference between images is illustrated in (c). When power compensation is applied, the impact of this power fluctuation is mitigated for both frame 1 (d) and 4 (e), reducing the difference between images as shown in (f).

An expected consequence of compensating for lower power signals is an increase in background noise which can be seen in (e). This effect can be managed with image segmentation which will be discussed further in subsequent chapters. Power compensation does not perfectly remove the differences between frames as shown in (f). A possible reason for these differences include heating of the stationary target during imaging, resulting in larger non-radiative signal for the same effective input power.

The plot in (g) showcases the variability of power for 558 nm when this dataset was captured. Both 532 nm and 558 nm experience overshoot when the laser is first turned on, however 532 nm settles to a steady state, while 558 nm is far more volatile. The start up of the laser sources is staggered with 532 nm always initialized first to facilitate separating the interlaced 532 nm and 558 nm in post processing.

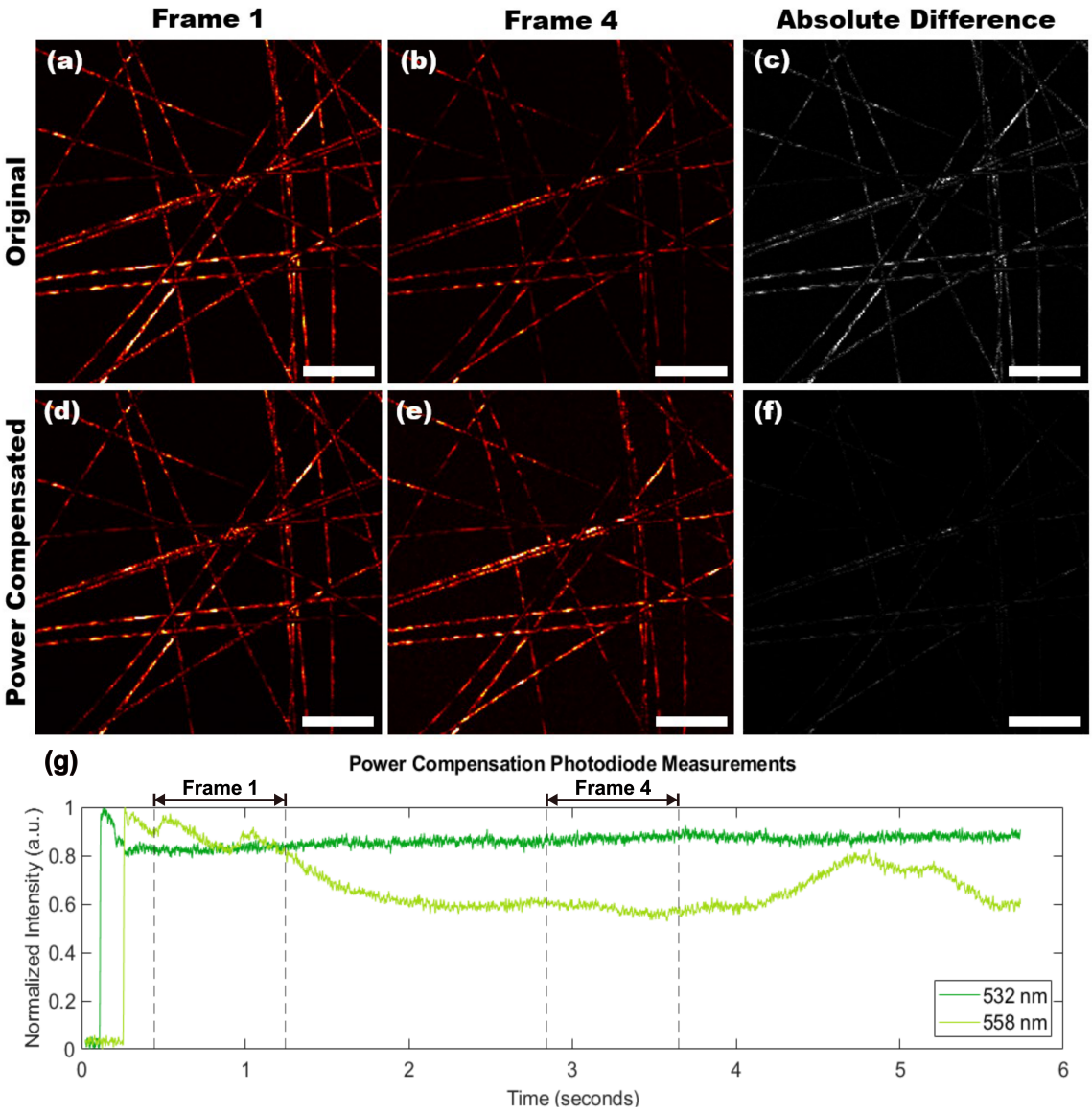


Figure 3.4: Illustration of power compensation for 558 nm excitation with carbon fibers in mineral oil. Images have a field of view of 512 x 512 μm and the scale bar represents 100 μm. The original non-radiative images for frames 1 and 4 are shown in (a) and (b) respectively. (c) shows the absolute difference between (a) and (b). (d) and (e) show the power compensated non-radiative images for frames 1 and 4 respectively, and (f) shows the absolute difference of (d) and (e). (g) shows the intensity of incoming excitation pulses for both 532 nm and 558 nm during the acquisition of this carbon fiber dataset.

3.4.2 558 nm Excitation Generation

Polarization Alignment

In order to generate sufficient 558 nm through SRS, the polarization of the 532 nm laser is aligned to the PM fiber using a HWP. This alignment is dependent on the orientation of the single mode fiber in the fiber launch, which will change and require re-alignment whenever the fiber is re-cleaved or re-seated.

As discussed in Chapter 2, Raman gain is maximized when the pump and Stokes are co-polarized, and minimized when the pump and Stokes are orthogonal [72]. When the polarization of the pump is aligned into either the fast or slow axis, the linear polarization is maintained across the fiber length. This creates a co-polarized state which maximizes Raman gain. However, when the pump polarization is not aligned to the fiber, both the polarization state and Raman gain become unpredictable.

Figure 3.5 illustrates the change in SRS spectra for various HWP angles and polarization alignments. Using the same 532 nm pump power, the HWP was rotated at increments of 5°. Using a 27% set point provides sufficient power for the generation of the 1st Stokes wavelength at 545 nm despite an unknown polarization state. However, the 2nd Stokes wavelength at 558 nm is only generated when the pump is correctly aligned to the PM fiber, which maximizes Raman gain.

Raman Threshold

As discussed in Chapter 2, Stokes wavelengths are only generated once the Raman threshold of power has been reached. This effect is shown in Figure 3.6 which illustrates the SRS spectra across increasing 532 nm pump power, this is controlled by increasing the laser set point. For a set point between 0-12% the pump power remains below the Raman threshold, thus no Stokes wavelength is generated. This threshold is surpassed at 15% wherein the 532 nm pump is converted to a 545 nm Stokes, as shown by the rapid decrease in 532 nm and increase in 545 nm. When a set point of 25% is reached, the 545 nm Stokes then becomes the pump for a secondary Stokes at 558 nm. This cascading of Stokes wavelengths can continue further with increasing power, however this was not necessary as 558 nm is the desired wavelength for this application.

Competing non-linear effects cause the broadening of each subsequent Stokes wavelength in an SRS cascade [72]. This effect can be observed in Figure 3.6 as the 532 nm pump has the narrowest spectral bandwidth, and spectral broadening is seen for both 545 nm and 558 nm.

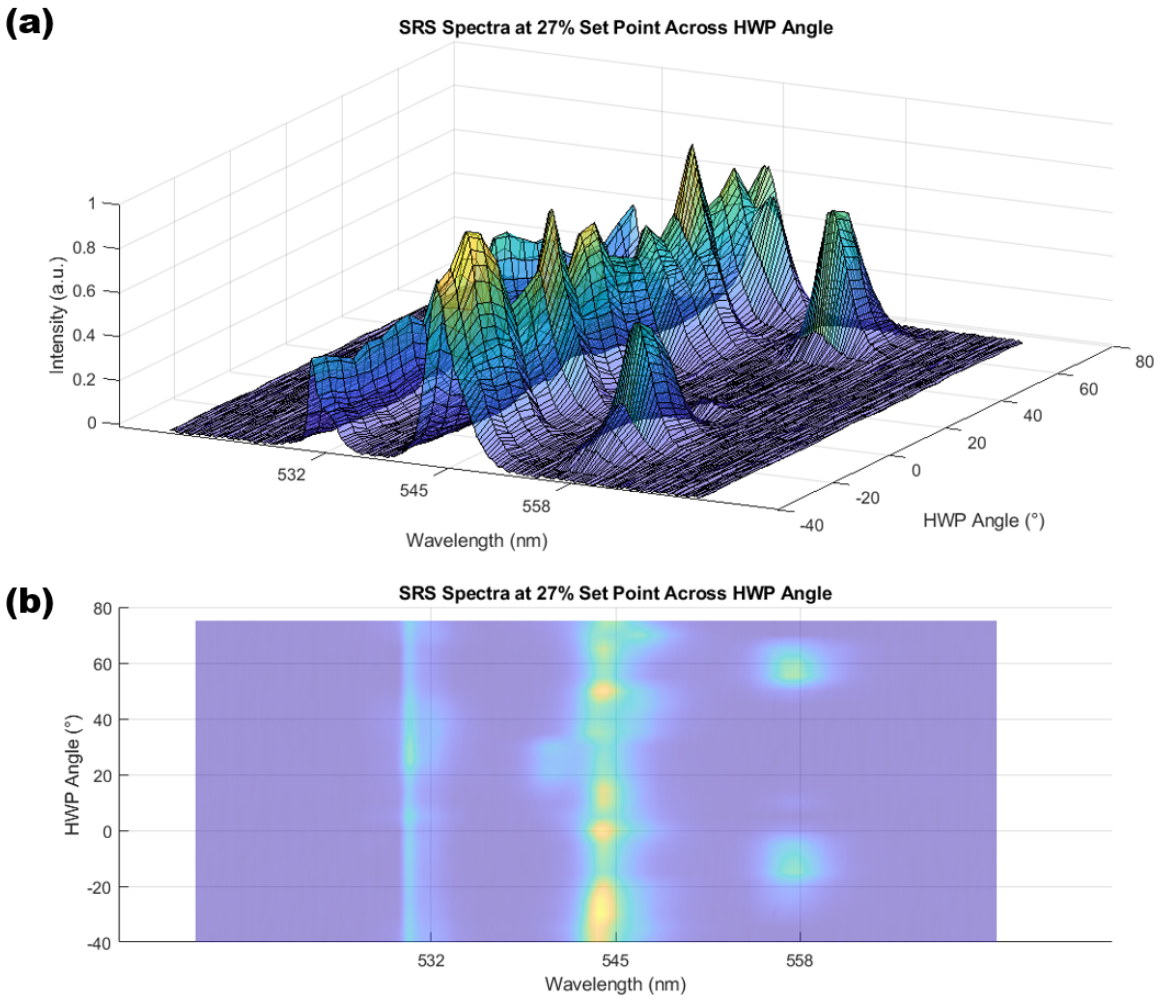


Figure 3.5: Illustration of the change in SRS spectra with variation in half-wave plate (HWP) angle shown in 3-dimensions (a) and 2-dimensions (b).

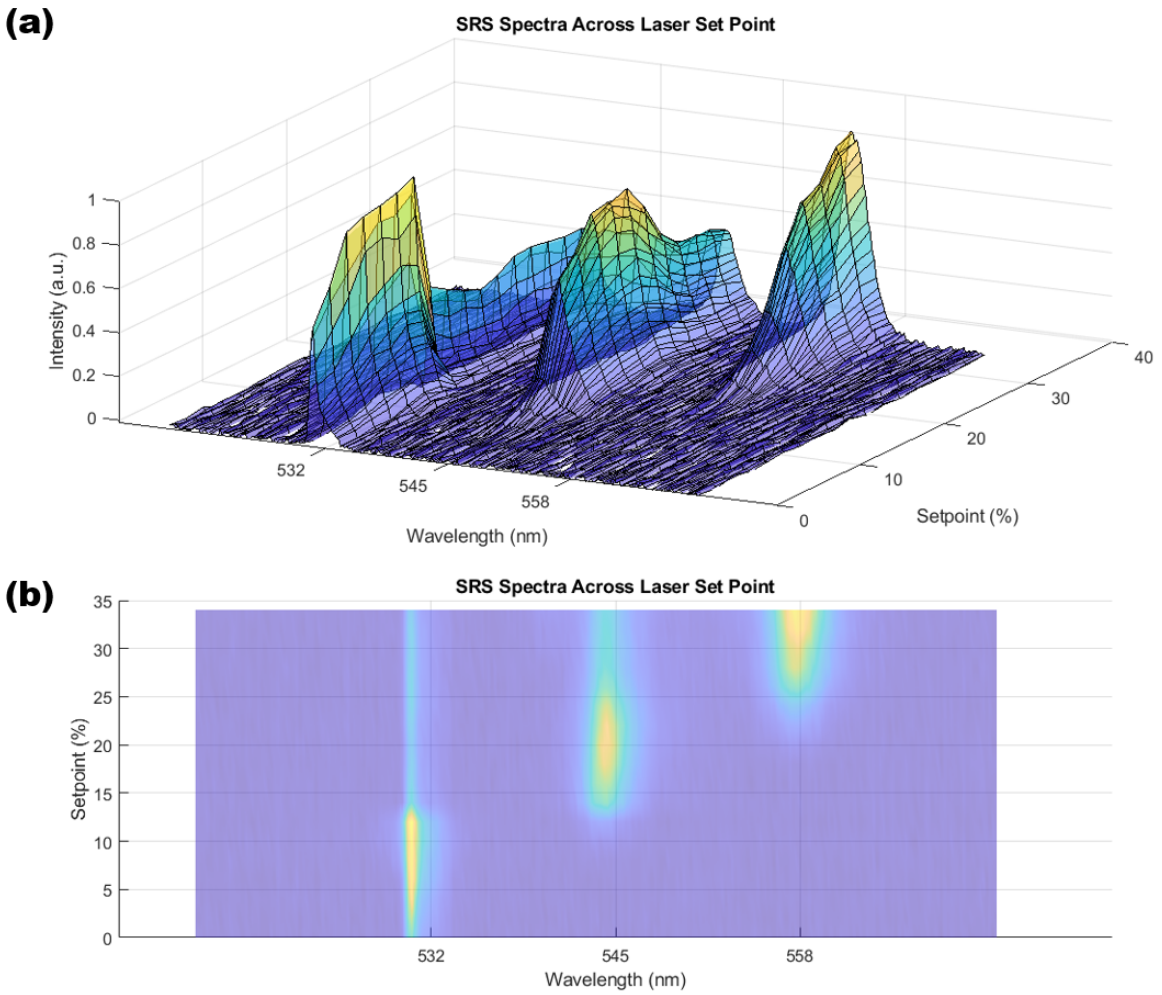


Figure 3.6: Illustration of the change in SRS spectra with variation in laser set point shown in 3-dimensions (a) and 2-dimensions (b).

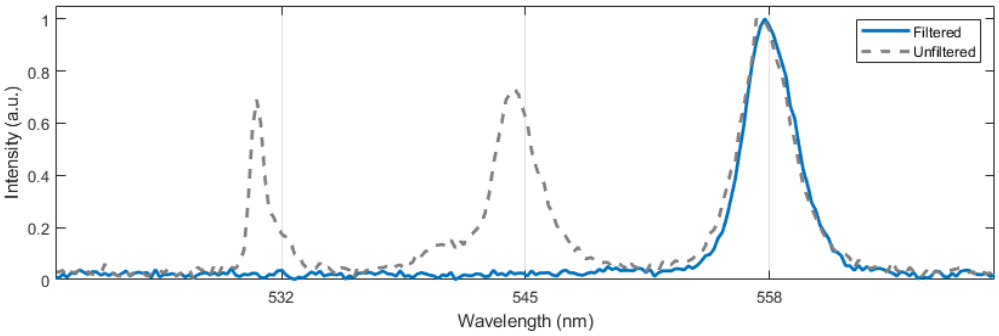


Figure 3.7: Illustration of the filtering of SRS spectra to isolate 558 nm.

Filtering

Figure 3.7 illustrates the spectra before and after filtering for 558 nm. A consideration when angling a bandpass filter is that large angles of incidence can distort the shape and transmission of the passband [80]. When comparing the shape of the 558 nm peak before and after filtering, both maintain a Gaussian shape centered at approximately 558 nm. It is possible that the filter angle is reducing transmission, however this setup is able to provide pulse energies up to 70 nJ. This is more than sufficient for the *in vitro* and *in vivo* imaging performed in this work (see Chapter's 5 and 6). Figures 3.5, 3.6, and 3.7 all show a downshifted frequency which is particularly prominent for 532 nm and 545 nm. While the exact cause is unclear, the output of this specific 532 nm laser peaks at 530 nm rather than 532 nm. This leads to a downshifting of SRS peaks, however the impact is limited at 558 nm due to SRS-induced spectral broadening. The resulting central wavelength is 557.8 nm as shown in Figure 3.7.

3.4.3 Multi-Wavelength *in vivo* PARS Images

The chorioallantoic membrane (CAM) in chicken embryo models provides a valuable *in vivo* imaging target due to the dense vasculature and capillary beds near the surface of the membrane. Recently, J. A. Tummons Simmons et al. [70] demonstrated single excitation PARS imaging of the CAM at video rate speeds capable of capturing the flow of red blood cells. The multi-wavelength system extends upon this work by adding 558 nm excitation.

Figure 3.8 illustrates an interlaced multi-wavelength PARS image for all four contrasts: detection scattering, excitation scattering, non-radiative and radiative. Detection and excitation scattering illustrate surface morphology and structure, and are important contrasts

for system alignment. Non-radiative contrast enables label-free vascular imaging due to the high optical absorption of hemoglobin at green wavelengths. Radiative contrast in a CAM illustrates the shadows of larger blood vessels underneath the capillary beds. These shadows are likely due to large vessels blocking radiative relaxation of fluorescent bio-molecules below the CAM [12]. Contrasts from 532 nm (top row) and 558 nm (bottom row) show high similarity in structure. This highlights the importance of independent excitation paths to enable both wavelengths to be co-aligned, improving the consistency between 532 nm and 558 nm images. All contrasts shown in Figure 3.8 are captured simultaneously.

This system images at video rates, capturing individual red blood cells moving through vessels. In order to provide a stronger sense of vessel location and structure, non-radiative angiography images are generated by averaging sequential non-radiative images to trace the path of red blood cells. Figure 3.8 illustrates these non-radiative angiography images in (c) and (g). As discussed previously in this chapter, there is slight variation in the resolution and depth of focus of 532 nm and 558 nm. The non-radiative contrast for 532 nm shows slightly wider vessels and lower signal intensity for optimally-focused vasculature. This is due to the larger spot size, resulting in lower fluence, and the larger depth of focus, which captures more signal across the volume of a blood vessel. 558 nm has a higher resolution and smaller depth of focus, leading to increased optical sectioning such that the vessels at lower depths appear narrower. Additionally, areas of optimal focus provide more signal intensity due to an increase in fluence. Overall these differences are subtle, and Figure 3.8 shows that the multi-wavelength *in vivo* PARS system is capable of capturing images which are consistent in structure between 532 nm and 558 nm. Further illustrations of images with consistent structure are shown in Chapter 6 Figure 6.5.

As discussed previously, to determine SO_2 it is crucial that the PARS multi-wavelength system can reliably capture images which are structurally consistent between 532 nm and 558 nm excitation. The ability to capture a large number of images which are structurally consistent in both wavelengths is shown in the *in vivo* hypoxia study which is discussed in detail in Chapter 6. In the first hypoxia experiment, ∼6,700 interlaced multi-wavelength images are captured from the same vascular location over the span 48 minutes. Additionally, relative change in SO_2 is shown in two separate experiments, performed by the same operator on different days, with different chicken embryos and the system was re-aligned before each experiment. In total, the first hypoxia experiment captured >9,000 interlaced images over 3 hours (Figure 6.9) and the second experiment captured >3,600 interlaced images over 1.5 hours (Figure 6.10). The high number of images which can be captured of the same vascular structure, and the success of the hypoxia study, illustrates the reliability of the PARS multi-wavelength system in capturing structurally consistent non-radiative images for both excitation wavelengths.

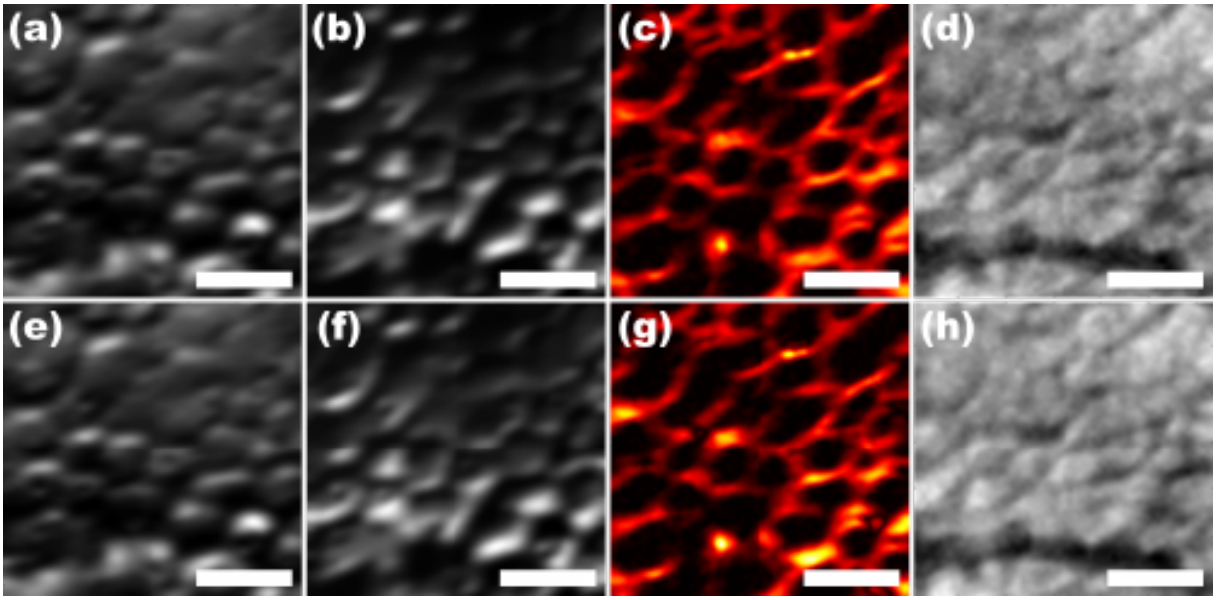


Figure 3.8: Multi-wavelength *in vivo* interlaced PARS images of chicken embryo CAM for 532 nm in the top row (a)-(d) and 558 nm in the bottom row (e)-(h). (a) and (e) shows detection scattering, (b) and (f) excitation scattering, (c) and (g) non-radiative contrast as well as (d) and (h) which show radiative contrast. The field of view is 128 μm x 128 μm with a scale bar of 40 μm.

3.5 Conclusions

The multi-wavelength PARS *in vivo* system is capable of capturing consistent *in vivo* PARS images for both 532 nm and 558 nm excitation. This is made possible by implementing independent excitation paths and interlacing images. Additionally, 558 nm excitation is improved by introducing polarization alignment through the addition of a half-wave plate. Power compensation is also implemented to account for pulse-specific power fluctuations in post-processing, which is critical for the quantitative measurement of SO_2. Future work on this system will address the slight discrepancies in resolution between 532 nm and 558 nm excitation by implementing higher sensitivity optomechanics. Overall, the capability to consistently image the same vascular structures between both excitation wavelengths is a valuable step towards the measurement of oxygen saturation with PARS, which will be discussed further in subsequent chapters.

Chapter 4

In vitro Blood Deoxygenation and Oxygenation

4.1 Introduction

In order to develop an empirical model to determine absolute measurements of SO_2 using multi-wavelength PARS, the ground truth SO_2 must be known and correlated with PARS SO_2 measurements. Gold standard CO-Oximetery devices such as the AVOXimeter [82] can be used to measure ground truth SO_2. In order to correlate and then validate absolute SO_2 measurements, a wide range of SO_2 levels must be used to test the system. This motivates the need to develop methods to oxygenate and deoxygenate blood for *in vitro* studies which can achieve intermediary SO_2 levels. It is crucial that approaches for modulating blood SO_2 do not introduce confounding factors which could limit the accuracy of both the empirical model and system validation. Ideally, methods should also be low-cost and time-efficient. This chapter presents a PARS-specific blood oxygenation and deoxygentaion protocol which achieves intermediary blood SO_2 levels for *in vitro* experiments.

4.2 Background

4.2.1 Blood Deoxygenation and Oxygenation

Blood is easily oxygenated when exposed to ambient air. As a result, the first challenge is to deoxygenate the blood. There are various deoxygenation approaches for this such as

nitrogen gas, sodium hydrosulfite and yeast.

The bubbling [83] or surface flowing [42] of nitrogen gas washes-out oxygen in blood through the process of diffusion. This approach is non-linear, costly, time consuming, requires an airtight deoxygenation set up, and cools the liquid. Additionally, bubbling gas through blood creates microbubbles which cause optical inhomogeneities [83].

Sodium hydrosulfite is a linear approach for blood deoxygenation [29][84][85], however this chemical is a fire and explosion risk when in contact with oxidizing agents [86]. Hydrogen peroxide (H_2O_2), a weak acid and strong oxidizing agent, is used for blood oxygenation, thus for safety reasons sodium hydrosulfite was avoided.

Yeast is widely used for blood deoxygenation [87][88][89][90] due to the ease of use, speed and low cost of this approach [83]. Deoxygenation occurs through the aerobic respiration of yeast, which consumes oxygen in the same process as human tissue [90]. Adding yeast introduces scattering particles, however the proportion of yeast to the volume of blood is small at 1:100 of yeast (g) to blood (mL). Additionally, PARS is an absorption-based method; as shown in this chapter, yeast does not provide non-radiative contrast at 532 nm and 558 nm excitation. Therefore it does not interfere with the primary contrast for determining oxygen saturation. This work uses instant baker's yeast for blood deoxygenation due to the ease of use and low cost of this approach.

Once deoxygenated, blood must be re-oxygenated to intermediary SO_2 levels. Exposing blood to ambient oxygen or bubbling oxygen gas causes blood re-oxygenation, however, it is difficult to control the resulting oxygen concentration with these approaches. Hydrogen peroxide can be used to re-oxygenate blood in a controlled manner [84]. When added to blood, hydrogen peroxide decomposes rapidly. This causes oxygen gas to bubble thorough the blood and re-oxygenates it to a controllable concentration [91]. Mircobubble generation can increase scattering, however this is of limited consequence as PARS is an absorption-based approach.

4.2.2 Methemoglobin & Carboxyhemoglobin

The primary derivatives of hemoglobin are deoxy- and oxy-hemoglobin, which contribute oxygen delivery and carbon dioxide removal from tissue. Dyshemoglobins are derivatives of hemoglobin which impede oxygen delivery and primarily take the form of Methemoglobin (MetHb) and Carboxyhemoglobin (COHb).

The ability for MetHb to transport oxygen is impaired by the oxidation of ferrous iron (Fe^{+2}) to ferric iron (Fe^{+3}). Typical physiological values of MetHb range from 0-2%.

Levels greater than 20% typically cause symptoms and levels above 70% can be fatal. Drugs containing oxidizing agents, such as topical anesthetics, are the most common cause in the formulation MetHb [92][93]. COHb is formed due to the inhalation of carbon monoxide, a poisonous gas which has a higher affinity to bind to hemoglobin than oxygen. The impaired oxygen carrying capacity has harmful effects which can be lethal. Typical values of COHb are 3% in non-smokers and 10% in smokers [94].

The importance of MetHb and COHb in this work is twofold. First, the *in vitro* blood deoxygenation and oxygenation exposes blood samples to processes atypical to those found in the body. It is important to monitor the effects of these protocols on all derivatives of hemoglobin. Since hydrogen peroxide is a strong oxidizing agent, the addition of this chemical into the blood can cause the creation of MetHb [92], thus this dyshemoglobin is particularly important to monitor. Second, the absorption of COHb and MetHb vary across 532 nm and 558 nm excitation [95]. This has the potential to interfere with the accuracy of PARS measurement of SO_2. MetHb and COHb are known to cause SO_2 measurement inaccuracies in pulse oximetry, which uses the scattering 660 nm and 940 nm light, due to the variation in absorption which confounds the measurement of deoxy- and oxy-hemoglobin [30][96].

4.3 Methods

4.3.1 Blood Selection

This work uses whole sheep blood anticoagulated with EDTA (Hemostat, SBE100). Sheep red blood cells (RBCs) have a diameter of 4 - 5 μm [97], which is smaller than human RBCs (7.5 - 8.7 μm) [98]. Despite differences in cell size, the absorption spectra of sheep and human oxy- and deoxy-hemoglobin have high similarity [29]. Due to the high cost and low availability of human blood, sheep blood was used in this work. A gold-standard clinical-grade CO-Oximetery device (Werfen, AVOXimeter 4000) is used for ground truth measurements of SO_2. This device requires the use of whole blood, and is only compatible with heparin or EDTA anticoagulants [82]. EDTA was selected as it best preserves RBC morphology and has excellent stability of hematological parameters [99].

4.3.2 Deoxygenation

The blood is stored at 4°C, as a result, the first step in deoxygenation is to raise the blood to body temperature and ensure it is well-mixed. A hot plate and stirrer (ONilab MS-

H280-Pro) is used to mix at 500 rpm and heat to 37°C [83][100] for 20 minutes. To improve dissolvability and prevent clumping, the yeast (Fleischmann's, Quick Rise Instant Yeast) is mixed into room temperature phosphate buffer solution (PBS). This deoxygenation uses 1:100 of yeast (g) to blood (mL) and 1:40 ratio of PBS (mL) to blood (mL). The yeast and PBS are combined separately, and the mixture is then added to the blood. The blood, yeast and PBS mixture is stirred continuously at 500 rpm and 37°C for an additional 40 minutes. During this time, the blood darkens in colour as deoxygenation occurs (see Figure 4.1). To prevent re-oxygenation from ambient oxygen, the blood is either aspirated into a syringe or sealed from ambient air with mineral oil. The yeast continues to consume oxygen after the 40 minute mixing period, and the sealed blood will continue to deoxygenate over time. As a result, the ground truth SO_2 is measured with the AVOXimeter immediately before experimental PARS measurements are taken.

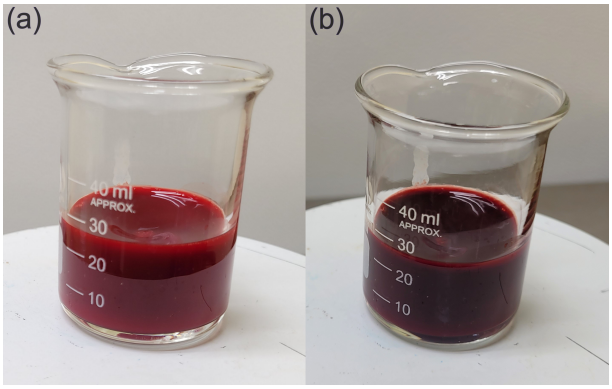


Figure 4.1: Whole sheep blood before and after yeast deoxygenation. (a) Blood before deoxygenation. (b) Blood after deoxygenation

4.3.3 Oxygenation

Small volumes of 30 wt.% H_2O_2 (Sigma-Aldrich, 216763) are used to re-oxygenate blood in a controlled manner [84][91]. The amount of H_2O_2 depends on both the initial SO_2 level, desired SO_2 and volume of blood. Typical H_2O_2 values range from 1-5 μL of 30 wt.% H_2O_2 (8.82-44.10 μmol of H_2O_2) per 3 mL of deoxygenated blood.

During blood re-oxygenation, exposure to ambient oxygen must be prevented in order to control oxygen concentration. This is executed with a syringe-to-syringe tubing adaptor assembly, shown in Figure 4.2 that consists of two luer lock syringe adaptors connected to one another with a short section of tubing (Saint-Gobain, Tygon S3™ E-3603).

To re-oxygenate the blood without exposure to ambient oxygen, the deoxygenated blood is aspirated into a 3 mL leur lock syringe. The plunger is removed from another 3 mL leur lock syringe, and a droplet of H_2O_2 is placed onto the plunger using a 0.2 - 2 μL pipette (Gilson, F144561). The plunger is reinserted into the syringe barrel, and both syringes are connected into the syringe adapter assembly. The two syringes and attaching adaptor are oriented such that the syringe containing deoxygenated blood is elevated above the syringe containing H_2O_2 to avoid air bubbles. The blood is quickly draw into the bottom syringe containing the H_2O_2. When exposed to blood, the H_2O_2 decomposes rapidly, creating microbubbles of oxygen gas. To ensure uniform oxygenation, the syringe assembly is held in place for 30 seconds, than inverted for another 30 seconds. For a total of 5 minutes, the assembly and syringes are inverted and re-inverted at 30 seconds intervals to ensure satisfactory mixing [91]. Since the H_2O_2 oxygenated blood still contains oxygen consuming yeast, the oxygenation level is transient. As a result, the ground truth SO_2 values are measured immediately before experimental data is collected.

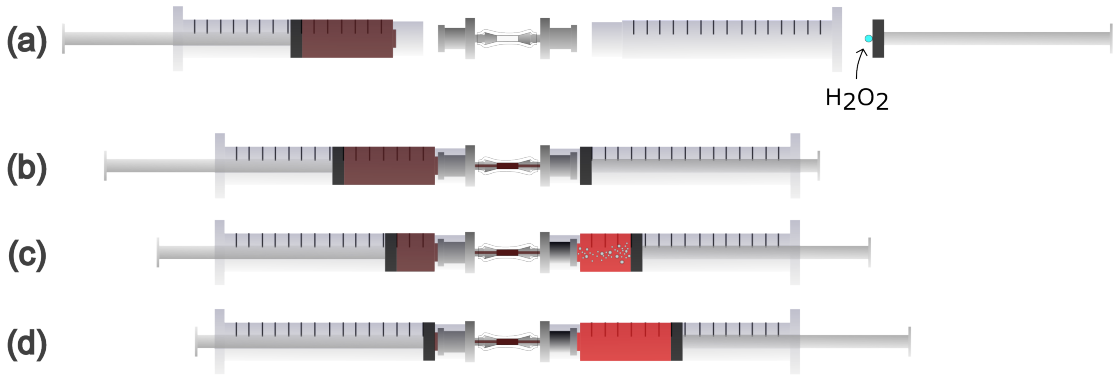


Figure 4.2: Blood chemical oxygenation. (a) Shows an exploded view of the deoxygenated blood syringe (left), the syringe adaptor assembly (center) and the H_2O_2 syringe and (b) shows the assembled system. (c) Shows the blood aspirated into the H_2O_2 syringe and reacting with H_2O_2. (d) illustrates the re-oxygenated blood after inversion.

4.4 Results & Discussion

4.4.1 Impact of Yeast on Non-Radiative Contrast

As discussed previously, the addition of yeast introduces scattering particles to the blood. Since blood oxygenation measurement relies on non-radiative signals, it was important to ensure that the addition of yeast would not impact this contrast. Two slide smears were prepared, one with red blood cells and the other with yeast as shown in Figure 4.3.

Multi-wavelength PARS images were collected for both slides at 45 nJ of excitation, this is the same pulse energy used for blood flow phantom imaging which will be discussed further in Chapter 5. At this excitation power, strong non-radiative signal is shown for both 532 nm and 558 nm for the red blood cells, and no signal is seen from the yeast. Instead, the yeast shows high scattering for both excitation wavelengths. The interference seen in (h) is a result of parasitic beams from the 70:30 beam splitter cube.

This figure also further illustrates the slight differences between 532 nm and 558 nm resolution. The higher resolution and smaller depth of focus of 558 nm causes the red blood cells to be optically sectioned into circles, whereas the 532 nm with its larger depth of focus portrays the expected doughnut shape of a red blood cell.

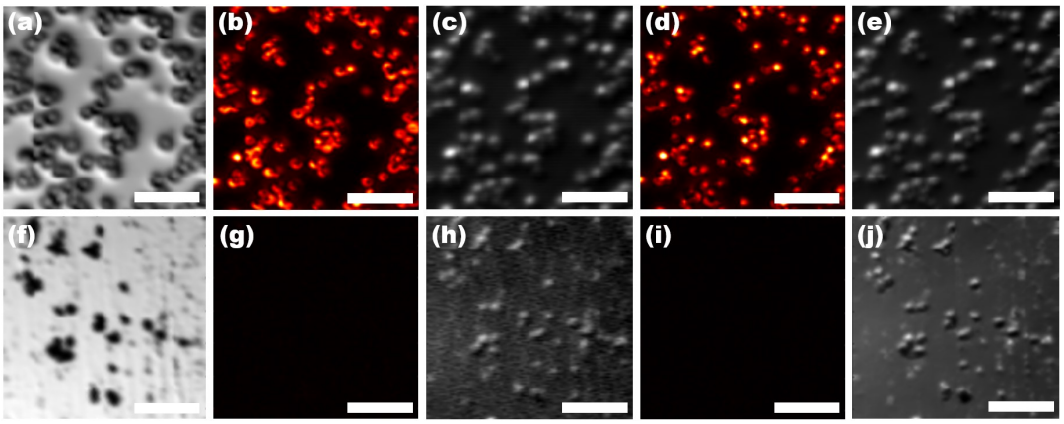


Figure 4.3: Red blood cells (top row) and yeast (bottom row) smears on a slide. Detection scattering (a),(f), 532 nm non-radiative (b),(g), 532 nm excitation scattering (c),(h), 558 nm non-radiative (d),(i) and 558 nm excitation scattering (e)(j). The field of view is 128 μm x 128 μm with a scale bar of 40 μm.

4.4.2 Blood Deoxygenation and Oxygenation

Using the methods described above, blood samples were successfully prepared across various blood oxygenation levels as shown in Table 4.1. SO_2, MetHb and COHb were measured using the gold standard AVOXimeter [82]. The presented results were collected on two separate days ($n = 2$), by the same operator, using the same equipment.

Experiment	Sample No.	SO_2 (%)	MetHb (%)	COHb (%)
A	1	29.50	0.00	2.00
	2	44.10	0.00	2.40
	3	53.10	0.00	3.50
	4	65.70	0.00	2.20
	5	77.10	1.40	1.50
	6	91.50	2.50	1.80
	7	99.90	3.80	0.60
B	1	20.20	0.00	2.20
	2	55.70	0.00	3.00
	3	75.70	0.00	2.90
	4	81.00	0.70	3.50
	5	91.10	2.90	2.00
	6	99.90	2.80	2.00

Table 4.1: *In vitro* whole sheep blood deoxygenation and oxygenation to achieve incremental SO_2 concentrations. COHb and MetHb concentrations are shown for all samples.

In experiment A, sample 1 was prepared using yeast deoxygenation and samples 2-6 where deoxygenated with yeast and re-oxygenated with H_2O_2. Sample 7 had no yeast or H_2O_2 added and was aspirated into a syringe after the 20 minute mixing and heating period to ensure full oxygenation. Sample 1 in experiment B was yeast deoxygenated, and samples 2-5 were deoxygenated with yeast and re-oxygenated with H_2O_2. Sample 6 was only mixed and heated. Examples of H_2O_2 volumes and resulting SO_2 are located in Appendix A.

Table 4.1 also illustrates changes in COHb and MetHb which occur for different samples. Samples with higher oxygenation have higher concentrations of COHb. However, untreated blood samples (experiment A sample 7 and experiment B sample 6) have the highest COHb and were not treated with hydrogen peroxide. This prevents the conclusion that COHb increase is due to the addition of H_2O_2. MetHb also varies between samples, however the direct cause of this is unclear. Typical physiological values of MetHb are 0-2% [93] and 3%

COHb for non-smokers [94]. In the results presented in Table 4.1 all values of MetHb and CoHb remain below 4%, which is slightly higher than typical.

Simulation Results

The impact of MetHb and COHb concentrations on the PARS multi-wavelength system is an important consideration to determine whether these dyshemoglobins will prevent the system from differentiating between oxygenation levels. As discussed previously, MetHb and COHb also have varying absorption spectra in the visible range and can cause confounding effects on the outcomes of two-wavelength SO_2 measurement.

This was addressed through the simulation of absorption for each sample. Non-radiative PARS contrast is an absorption-based metric, and the ratio of non-radiative contrast between 532 nm and 558 nm demonstrates a change in absorption. The wavelength-specific absorption of a mixture of hemoglobin derivatives is demonstrated in Equation 4.1 [30]. $A(\lambda)$ represents the absorption of a mixture at a particular wavelength, C represents the concentrations of each hemoglobin derivative and $\epsilon(\lambda)$ is the wavelength-specific extinction coefficient per hemoglobin derivative. This simulation assumes a unity light path length l.

$$A(\lambda) = l(C_{HbO2} \cdot \epsilon_{HbO2}(\lambda) + C_{Hb} \cdot \epsilon_{Hb}(\lambda) + C_{MetHb} \cdot \epsilon_{MetHb}(\lambda) + C_{COHb} \cdot \epsilon_{CoHb}(\lambda)) \quad (4.1)$$

The objective of this simulation was to compare the ratio of absorption of 532 nm and 558 nm with and without MetHb and COHb to determine if the presence of these dyshemoglobins would impair *in vitro* blood oxygenation results. For each sample, the absorption of 532 nm and 558 nm was calculated using the concentrations of hemoglobin derivatives shown in Table 4.1. When simulating absorption without MetHb and COHb, these proportions were assumed as O_2Hb since these dyshemoglobins limit oxygen carrying capacity. Tabulated extinction coefficients for all derivatives of adult sheep hemoglobin used in this simulation are courtesy of Zijlstra et al. [29]. The ratio of absorption of 532 nm and 558 nm is calculated using Equation 4.2, which represents a proportional ratio and will be discussed further in Chapter 6.

$$Ratio = \frac{I_{558}}{I_{532} + I_{558}} \quad (4.2)$$

Figure 4.4 shows the difference between simulated absorption with and without MetHb and COHb. For both experiment A and B, only very subtle differences can be observed between ratios with and without MetHb and COHb. Despite these small variations, the

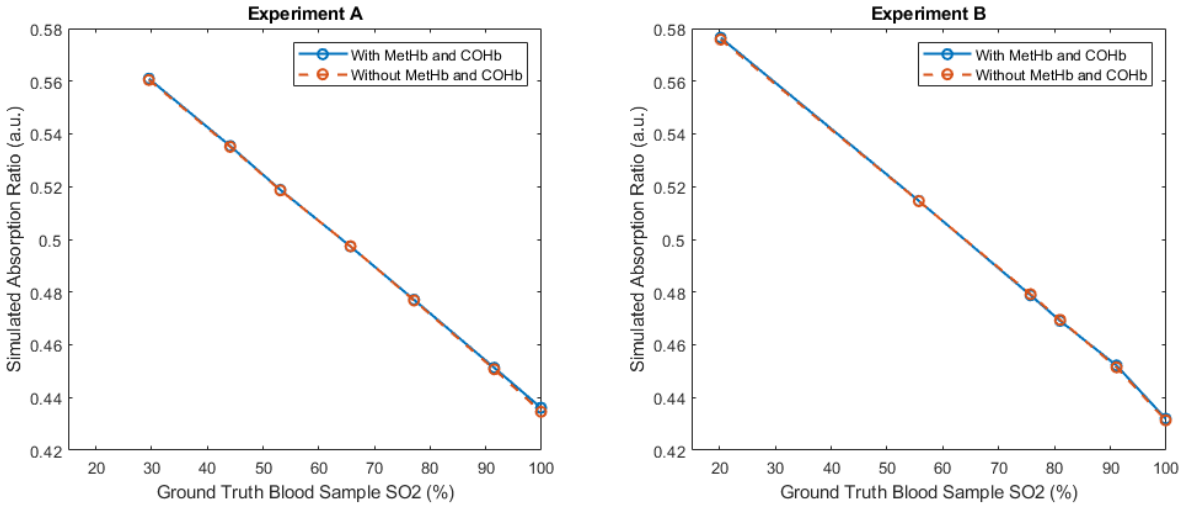


Figure 4.4: Simulated absorption ratio of 532 nm and 558 nm of blood oxygenation and deoxygenation with and without MetHb and COHb.

overall trend of deoxy- and oxy-hemoglobin remains clear, such that small concentrations of MetHb and COHb will not obstruct the differentiation between oxygenation levels. However, it remains important to account for the concentrations of MetHb and COHb when determining a PARS empirical SO_2 model and when validating the accuracy of SO_2 measurement.

4.5 Conclusion

This chapter presents a unique protocol for blood oxygenation and deoxygenation specifically designed for PARS. Yeast is leveraged for the deoxygenation of blood, and hydrogen peroxide is used for the controllable and incremental re-oxygenation. These approaches are relatively low-cost and time-efficient compared with the use of nitrogen gas. By comparing slides of red blood cells and yeast, it is determined that yeast does not contribute non-radiative signal at 532 nm and 558 nm excitation, thus the addition of yeast will not negatively impact PARS SO_2 measurement. Data from two experiments show the capability of this deoxygenation and re-oxygenation approach to prepare blood samples at a wide range of SO_2 levels from 20% to 99.9%. The MetHb and COHb concentrations are also presented for these samples. The absorption of each excitation wavelength, for a mixture of hemoglobin derivatives, is simulated to ensure that the presence of MetHb and COHb in

these prepared samples will not prevent expected absorption ratio trends to be observed. Due to the slight, or non-existent, differences between simulations with and without MetHb and COHb, it can be determined that this sample preparation is suitable for *in vitro* blood oxygenation and deoxygenation studies. This chapter presents a low-cost, time-efficient method for blood oxygenation modulation which is well-suited for PARS *in vitro* phantom studies.

4.6 Future Work

When working towards accurate SO_2 measurement using PARS, the impacts of MetHb and COHb are important to consider. Future work could involve the development of a blood preparation protocol to modulate MetHb and COHb. This would enable further studies to determine the allowable thresholds of these dyshemoglobins and their impact on measurement accuracy. An additional extension of this work includes applying blood oxygenation and deoxygenation studies to human blood, to work towards the goal of accurate SO_2 in humans.

Chapter 5

In vitro Flow Phantom

5.1 Introduction

Imaging *in vivo* has many complications, such as motion artifacts, which can cause challenges while imaging and interpreting results. Phantom studies provide a valuable platform to test imaging methods in a controlled environment in order to validate the performance and accuracy of a system. The blood oxygenation and deoxygenation protocol described in Chapter 4 is designed to control SO_2 levels within *in vitro* blood. However, a system was also needed to contain and flow the blood such that it can be imaged. This motivated the design of a flow phantom system, which is the focus of this chapter.

5.2 Background

5.2.1 Optical Properties of a Single Red Blood Cell

A normal red blood cell (RBC) has a flat, biconcave form, and the absorbing protein hemoglobin is concentrated within the cell [27]. Due to this irregular shape, the back-scattering of an RBC is known to be impacted by the size and orientation of the cell. The impact of cellular orientation is substantial enough that scattering-based methods for SO_2 determination cannot rely on the back-scattering of a single RBC. Instead, back-scattered signal from multiple RBCs must be averaged to remove the effects of orientation and size [101][43]. Work by Liu et al. determined that 147 $\pm$ 3 RBCs must be averaged in order for blood oxygenation contrast to be determined for their vis-OCT system [101].

The optical absorption properties of RBCs is also impacted by parameters of structure, osmolarity and flow. Hemolysis of blood occurs when the cell membrane of RBCs is ruptured and hemoglobin is distributed throughout the solution. The absorption coefficient of blood decreases significantly due to hemolysis. This is attributed to the multiple internal reflections occurring within a whole RBC cell, which increase the path length through the absorbing material and results in increased absorption. Hemolyzed blood lacks cell boundaries, preventing internal reflections and decreasing the absorption coefficient [27][102].

The osmolarity affects the shape of RBCs, wherein RBCs can swell or shrink. This change in shape impacts the absorption coefficient of the RBC, such that when a cell shrinks the absorption coefficient increases. Shrinkage increases the concentration of hemoglobin within the cell, which increases the refractive index of the RBC. This causes an increase in internal reflections, and results in an increased absorption [27]. The size, shape and orientation of RBCs also impacts the amount of internal reflections within the cell, which influences absorption [102].

Finally, shear force due to the flow of RBCs causes deformation in the cell. This shear force decreases the absorption property of RBCs, such that the optical properties of blood are impacted by flow velocity and shear [27]. This flow velocity work by Roggan et al. also demonstrated the importance of flowing blood for reproducible and exact measurements of optical properties of blood samples [27]. Overall, the optical properties of RBCs are influenced by structure, orientation and flow. This variation in optical properties necessitates the averaging of signal from individual RBCs to measure aggregate properties of blood.

5.2.2 Phantom Models

Stationary phantoms, such as embedding RBCs in agar, have been used to validate signal difference between oxy- and deoxy-hemoglobin [53]. However, there are some challenges with this approach. Embedded RBCs are useful for showing relative SO_2, but CO-Oximetery techniques cannot be used to measure ground truth SO_2 of the sample when it is embedded in agar. These measurement can be taken before the embedding process, but oxygen exposure or the time delay for agar to cure could impact the accuracy of the measurement.

A system that enables direct ground truth SO_2 measurement of the sample is necessary to move beyond relative SO_2 measurement, this requires the use of liquid blood. The work by Roggan et al. [27] demonstrates that flow conditions are critical for reproducible and exact measurements of the optical properties of blood samples, and the flow of RBCs impacts their absorption. This motivates the use of flowing blood in a phantom. A variety

of flow phantoms have been implemented to accomplish SO_2 system validation. Approaches have implemented cuvettes [22], capillary tubes [84][20] and custom flow phantoms which have been designed to simulate the optical properties of tissue [103].

As a result, the design of a flow phantom is important to enable ground truth SO_2 measurement and facilitate imaging the blood while it is flowing, which is a better representation of how the blood will behave *in vivo*. Additionally, the design of a flow phantom also provides value for validating future work on measuring blood flow with PARS.

5.3 Design Requirements

The multi-wavelength *in vivo* PARS system operates in reflection-mode, which is necessary for *in vivo* imaging due to sample thickness and the high scattering coefficient of biological tissue [16]. In order to measure non-radiative PARS signal, sufficient reflections of detection scattering are required. *In vivo* models are highly scattering, however the idealize optical properties of phantoms can result in reduced back-scattering, preventing the collection of sufficient non-radiative signal. The development of a successful flow phantom will require the selection of materials and a channel depth which facilitates back-scattering.

A common approach to measure ground truth blood flow is the use of capillary tubes [84][20]. The challenge with this approach is the lack of uniformity across the imaging region due to the curvature of the tube. Capillary tubes were initially tested, however the non-radiative signal was limited to the edges of the capillary tube where the glass to blood refractive mismatch caused enough back-scattered light to capture non-radiative signal. As a result, the first design requirement for the flow phantom was uniformity in depth, to ensure signal could be achieved across the entire imaging region.

Next, when imaging in a phantom, it can be challenging to determine imaging depth. Additionally, when imaging with two different excitation wavelengths it is important to ensure that both are co-focused at the same depth. Thus, a requirement of this design was to provide a mechanism to check the alignment and depth of imaging in the sample, and to validate that both excitation wavelengths are co-focused.

Finally, the ultimate goal of the multi-wavelength *in vivo* PARS system is to use both non-radiative and radiative contrast for SO_2 imaging in the context of surrounding bio-molecules. The absorption of blood is derived from non-radiative contrast due to the low quantum yield of blood [70]. The simultaneous capture of radiative contrast in the PARS architecture enables the potential for bio-molecules with a higher quantum yield, such that they fluorescence, to be un-mixed from blood. A design consideration was the ability to

add other bio-molecules, such as synthetic melanin [103] into the flow phantom. This would enable future experiments to test capabilities for un-mixing other bio-molecules.

These design requirements were determined through the iterative process of testing a variety of flow phantom designs. The unsuccessful flow phantom designs are summarized in Appendix B.

5.4 Material Selection

Polydimethylsiloxane (PDMS) is a polymer commonly used in phantom development [104][103] [105] due to its flexibility and durability. Molds are designed as the negative of the desired shape, allowing a wide range of form factors to be achieved. Once cured, PDMS is stable. Additionally, additives can be incorporated to adjust the absorption and scattering properties [103]. As a result, this material was selected for flow phantom development.

As discussed above, sufficient back-scattering is required to capture non-radiation signal in reflection-mode PARS. The refractive index of PDMS is <1.43 at 830 nm [106], which is similar to the refractive index of whole blood which ranges from 1.36 to 1.44 [107]. To increase the PDMS refractive index, titanium dioxide (TiO_2) is added in proportions which match the optical scattering of human tissue [103]. Initial iterations of this flow phantom did not contain TiO_2 and non-radiative signal could not be captured from blood.

5.5 Methods

5.5.1 Flow Phantom Preparation

The flow phantom consists of PDMS (Sylgard 184, Dow), 50 μm tape (IS214, SUNjin Lab) and a glass coverslip as show in Figure 5.1. A PDMS mold was designed in SolidWorks and 3D printed as shown in Figure 5.2, and the mold design was inspired by work from Galyastiv et al. [105]. When cured, the molded PDMS enables external tubing to be connected into the flow channel through inflow and outflow elbow joint ports which are formed using removable pins.

The PDMS is prepared using the following procedure. First, a 1:10 ratio of soap to isopropanol mixture is sprayed onto the mold and allowed to evaporate to improve delamination of the cured PDMS [103]. PDMS is prepared at a ratio of 1:10 of PDMS curing agent (g) to PDMS base (g). To increase the refractive index of the PDMS and

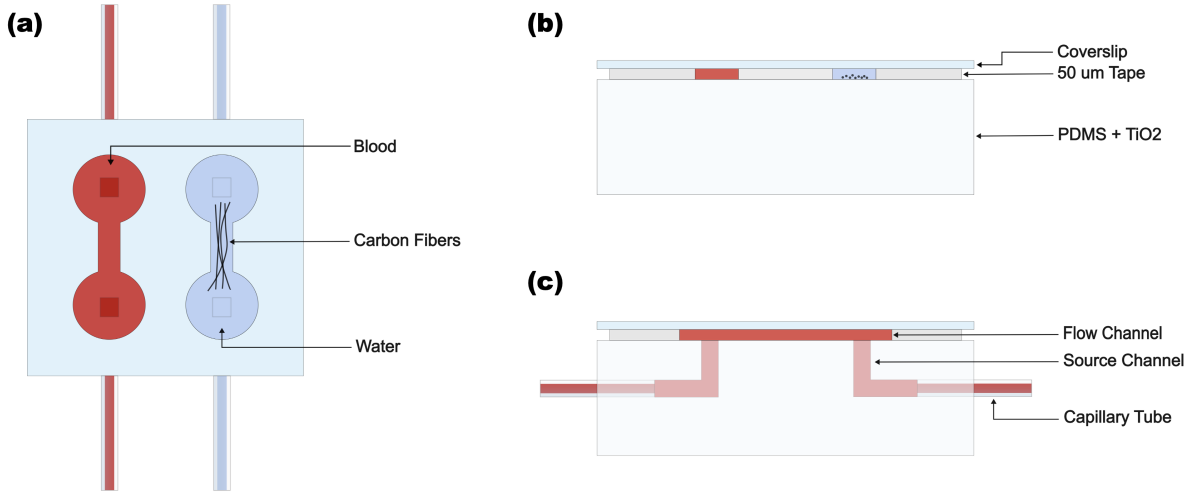


Figure 5.1: Flow phantom diagram of the top view (a), front cross-section (b) and side cross-section (c), of the flow phantom.

mimic the optical scattering of tissue, the ratio ∼8.55 mg of TiO_2 per gram of PDMS base is used [103]. In order to avoid clumping of the TiO_2 powder in the PDMS, the TiO_2 is mixed into the curing agent using a magnetic stirrer (11-300-49SHP, Fisherbrand Isotemp) at 500 rpm for 20 minutes. The curing agent and TiO_2 solution is then well-mixed into the PDMS base and de-gassed for 30 minutes to reduce mircobubbles created during mixing. The PDMS mixture is poured into the mold and allowed to cure for 48 hours at room temperature.

Upon curing the PDMS, it is removed from the mold and the soap delamination layer is removed by cleaning with deionized water and a kim wipe. An exacto knife is used to cut a channel between the two circular cutouts of the 50 μm tape. This will become the flow channel. The tape is placed onto the PDMS mold, and a coverslip is placed on top to create the flow channel. This design creates two channels, one for the flow of samples and the other for alignment. Before the coverslip is added, carbon fibers are placed into the alignment channel. A weight is placed on top of the coverslip for ∼12 hours to ensure an effective seal is created.

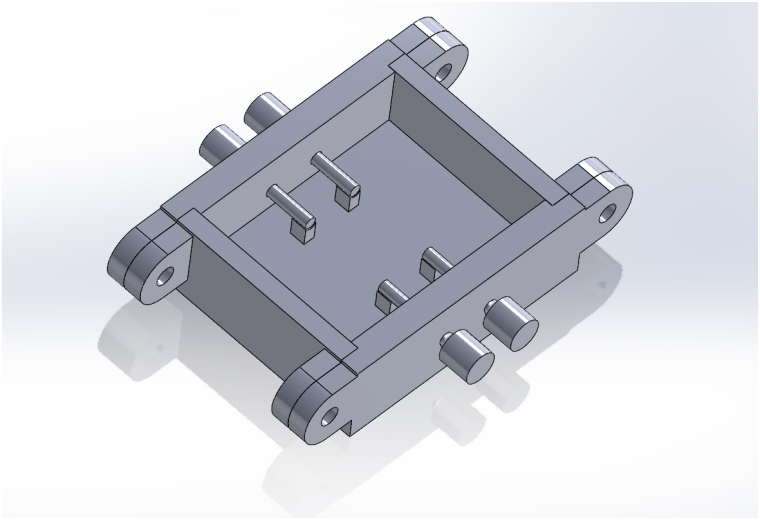


Figure 5.2: Flow Phantom PDMS Mold

5.5.2 Flow Phantom Experimental Procedure

Tubing (Saint-Gobain, Tygon S3™ E-3603) is inserted into the inflow and outflow elbow joints. The inflow is connected to a syringe through a syringe adaptor, and the outflow goes to a liquid waste beaker. In order to maintain consistent flow throughout the experiment, a syringe pump (NE-4000, New Era Pump Systems Inc) flows the sample at a constant speed of 1 μL/min.

Using the blood oxygenation and deoxygenation protocol described in Chapter 4, blood samples are prepared at intermittent levels of SO_2. Ground truth SO_2 measurements are collected immediately before flowing the sample through the flow phantom. Datasets of sequential, interlaced multi-wavelength PARS images are captured at the same imaging region in the phantom at both 45 nJ and 50 nJ excitation pulse energies. Images are 128 x 128 μm in size and each dataset included ~600 images.

5.6 Results & Discussion

Figure 5.3 shows the individual frames from three different blood oxygenation levels in detection scattering, and non-radiative contrast for 532 nm and 558 nm. While the pulse energies of both excitation wavelengths are the same, 558 nm has a higher fluence due to the smaller resolution, as discussed in Chapter 3. This is evident in Figure 5.3 wherein

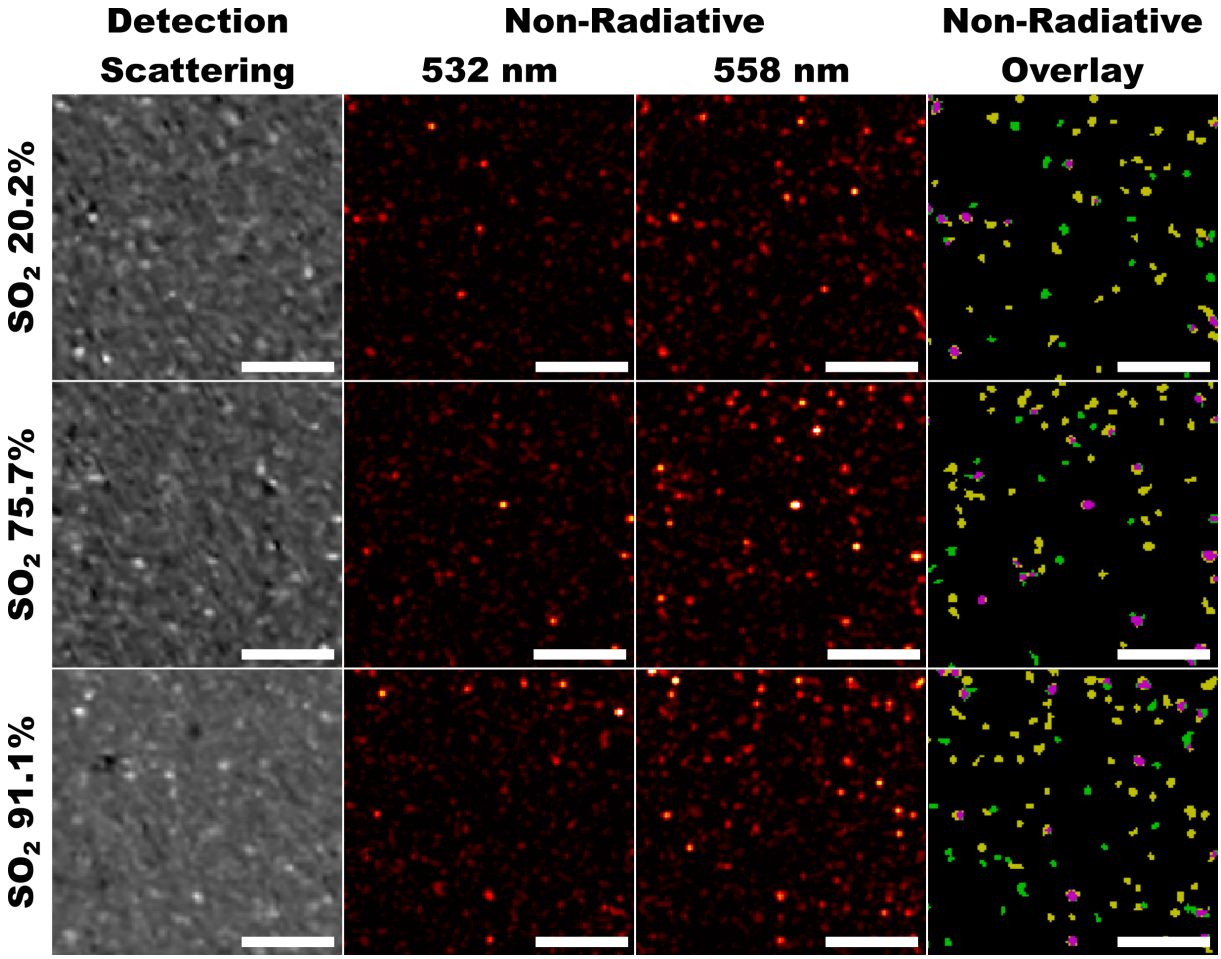


Figure 5.3: Multi-wavelength images of blood at various oxygenation levels in the flow phantom. The field of view is 128 μm x 128 μm with a scale bar of 40 μm. The non-radiative overlay shows a binary mask of RBCs, particles which appear only in 532 nm non-radiative are shown in green. Particles only in 558 nm non-radiative are shown in yellow, and particles which appear in both images are shown in magenta.

excitation is concentrated in a smaller depth of focus and at a higher fluence, enabling more signal to be captured in 558 nm. This causes differences in the RBCs which appear in 558 nm compared to 532 nm.

In order to visualized which RBCs appear in the images from one, or both excitation wavelengths, thresholding was used to remove the background of the non-radiative images which were than converted into a binary mask. False colours were applied to highlight which images the RBCs were found in. Particles which occur in both images are labeled in magenta, particles only in 532 nm are labeled in green and particles only in 558 nm are labeled in yellow.

Without knowing the locations of each particle relative to one another, it is difficult to determine the exact cause of certain RBCs appearing in both images, while others appear in only one wavelength. The higher fluence in 558 nm explains why more RBCs are seen in the non-radiative images of 558 nm excitation. However, there are a considerable number of particles which only appear in 532 nm. It is possible that the larger depth of focus in 532 nm is the cause. It is also possible that chromatic aberrations occur when imaging in a volume of liquid blood that are not seen during alignment in water. Sheep RBCs are 4 - 5 μm in diameter [97]. While the thickness of a sheep RBC has not been reported, to the best knowledge of the author, human RBCs have a diameter of 7.5 - 8.7 μm and a thickness of 1.7 - 2.2 μm [98]. Due to the small size of these cells, both in diameter and thickness, slight discrepancies in focal conditions between 558 nm and 532 nm excitation could result in the loss of certain particles in one excitation which appear in another. Determining the exact source of this discrepancy is particularly challenging in a flow channel where the depth of an individual RBC is unconstrained within a 50 μm channel and flow cannot be assumed as laminar.

To avoid the need for smaller channels to constrain depth and prevent the movement of particles in and out of optimal focus, it may appear advantageous to image a uniform liquid in the phantom, such as hemolyzed blood. Early work explored this, wherein the RBC cell membrane is ruptured and filtered out, leaving a uniform solution of hemoglobin. This would have resolved challenges of individual RBCs moving in and out of optimal focus, however three main limitations prevented the use of hemolyzed blood. First, the CO-Oximetry device is only compatible with whole blood, using hemolyzed blood would necessitate finding a different device for ground truth measurement. The procedure is also labour intensive and results in small yields of hemoglobin. Finally, the primary limiting factor is the decreased absorption of hemolyzed blood as discussed above [27][108], making this approach unsuitable for determining an empirical model which is intended to be applied to whole blood *in vivo*.

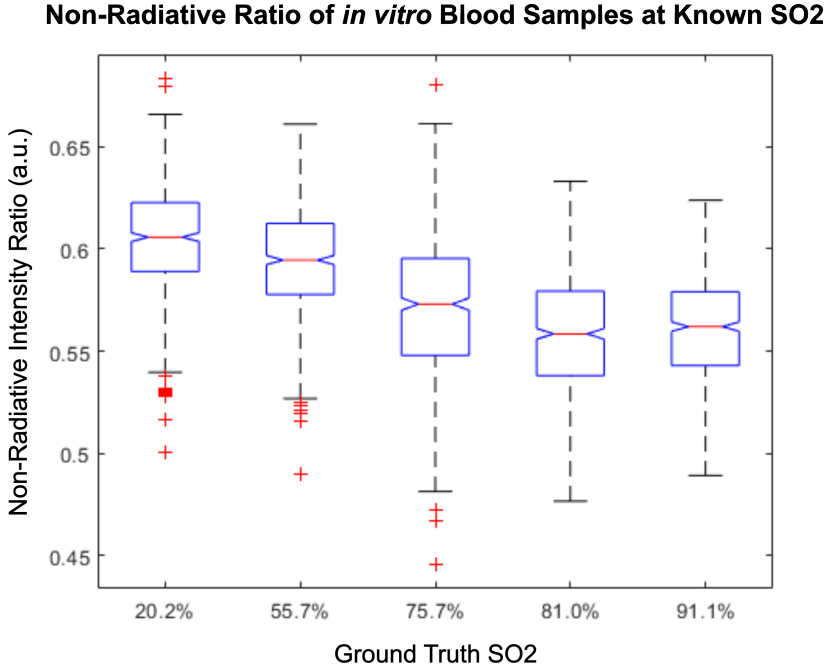


Figure 5.4: Image-based average ratio of non-radiative intensities of blood samples at known SO_2 levels in the flow phantom using 50 nJ excitation pulse energy. Datasets for each blood sample contain ~610 data points. Ground truth SO_2 values are determined with the AVOXimeter.

To analyze the change in absorption across blood samples with known oxygenation, the fractional ratio of non-radiative signal was determined using Equation 4.2. Image thresholding is used to remove the background and isolate signals from the RBCs, and binary masks are created for both 532 nm and 558 nm. The union of these binary masks is then used to further isolate RBCs which appeared in both 532 nm and 558 nm images, as shown in Figure 5.3 with the RBCs highlighted in magenta. The ratio of non-radiative intensities is taken in the image space (using Equation 4.2). Then, the binary mask is applied to the ratio image such that only the ratio from RBCs appearing in both images remain. The average ratio is calculated for each image in a dataset, representing a singular data point. Each dataset contains ~610 images per blood sample and this data is visualized using box plots (box and whisker plots) in Figure 5.4. The median is denoted by the central red line, and the 25th and 75th percentile is represented with the bottom and top of the blue box. When notches in the box do not overlap, this indicates a 95% confidence that the true medians differ. Outliers are shown with red '+' markers [109].

As discussed in Figure 3.1, 532 nm excitation is a near isosbestic point, such that absorption is the same for oxy- and deoxy-hemoglobin. For 558 nm excitation, deoxy-hemoglobin has a higher absorption than oxy-hemoglobin. As a result, the expected behaviour is for the ratio of non-radiative intensity to decrease as SO_2 increases. The data in Figure 5.4 shows a slight decrease in the median as ground truth SO_2 increases, with the exception of the dataset at 91.1% SO_2. A significant challenge with this flow phantom result is the lack of separability between datasets. It is expected that blood samples from such a wide range of SO_2 values should be easily separable. When this experiment was repeated the same issues arose and no substantial trend could be observed. The influence of hemoglobin derivatives MetHb and COHb on total absorption were considered as a potential cause of this unsuccessful result. However, the simulations presented in Chapter 4 disprove this, as the small quantities of MetHb and COHb in the samples have a small impact on overall absorption of the sample. Results presented in the following chapter illustrate that a change in absorption can be observed by the PARS multi-wavelength system *in vivo*. As a result, the flow phantom is suspected to be the cause of these unsuccessful results.

As discussed previously, averaging signal across multiple individual RBCs is important to remove the variability in absorption introduced by factors such as orientation and size. When averaging signal within an *in vivo* blood vessel, the path of the RBCs is constrained in depth. In the current design of the flow phantom, this degree of depth constraint does not occur in a 50 μm channel. Additionally, this flow phantom does not guarantee laminar flow. Since not all particles appear in both 558 nm and 532 nm, and the path of RBC flow is not constrained, this creates challenges in temporal averaging to remove the effects of absorption variation of a single RBC. Averaging across a frame may reduce some variation, however, the RBCs within a frame are not guaranteed to be at the same depth when averaged. When temporally averaging the signal from one blood vessel, the signal from all RBCs passing through that vessel are guaranteed to be at the same depth. The lack of separability between datasets, and the inability to reproduce the result presented in Figure 5.4 in a secondary experiment prevent the use of this flow phantom data to determine an empirical model of SO_2, or assess the accuracy of this system.

5.7 Conclusion

Flow phantom experiments are valuable to test the system in a controlled environment, however it can be challenging to replicate intricate structures found in nature such as capillary beds. After various design iterations and testing, a flow phantom design is presented which achieves a flow phantom channel of 50 μm. Using this flow phantom design,

the PARS multi-wavelength system is capable of capturing non-radiative signal for blood flowing through the channel at various oxygenation levels for both 532 nm and 558 nm excitation. Unfortunately, this flow phantom model did not achieve the ultimate goal of enabling the determination of a PARS-SO_2 empirical model or assessing SO_2 accuracy. However, important knowledge was gained in the course of this work, such as the importance of back-scattering light and constraining RBC flow in depth. These lessons are valuable in the future efforts which work towards the design and implementation of a flow phantom system which can be used to determine SO_2 accuracy.

5.8 Future Work

Next steps would involve using a smaller channel which would further constrain depth. Single cell flow channels can be fabricated through collaboration with external microfluidic manufacturers. This would be valuable for constraining RBC orientation, and would prevent RBCs from moving in and out of focus. Alternately, a flow phantom could be designed to ensure laminar flow of blood [27]. This would also prevent RBCs from moving in and out of focus, and if designed correctly, the PARS multi-wavelength system could capture videos following the flow of an individual RBC. This provides value for blood flow validation, as well as averaging of RBC signal. Additionally, other species with larger RBCs can be used, such as bovine or canine whole blood [97] to constrain the depth of RBC flow in a larger flow channel by increasing cell size, in order to accommodate for manufacturing limitations of channel depth.

Chapter 6

In vivo Blood Oxygenation

6.1 Introduction

To further technology towards the ultimate goal of clinical application, *in vivo* imaging is crucial in demonstrating capability beyond phantom and *in vitro* studies. However, *in vivo* studies present the challenge of obtaining ground truth bio-metrics with which to compare results. Ground truth *in vivo* SO_2 measurement requires invasive blood gas analysis or comparison with a gold standard SO_2 measurement approach [20][21]. Measuring relative change in blood oxygenation is a valuable tool to demonstrate *in vivo* feasibility.

6.2 Background

Demonstrating relative change in blood oxygenation involves varying the oxygen available to the *in vivo* target. The difference in signal ratio between states of hypoxia (low oxygen) and normoxia (normal oxygen) is compared. Relative *in vivo* blood oxygen experiments have been implemented with zebrafish embryos [53] and mouse models [78].

Recent work by J.A. Tummons Simmons et al. [70] demonstrated the use of PARS for imaging blood flow in the chorioallantoic membrane (CAM) in chicken embryo models. Through video rate imaging, the flow of individual red blood cells was captured with one excitation wavelength. The multi-wavelength PARS system aims to extend the capabilities of this system to include oxygen saturation measurement. The ultimate goal is to combine blood flow and oxygen saturation for the first ever demonstration of metabolic rate of

oxygenation (MRO_2) with PARS. To further these efforts, a relative *in vivo* blood SO_2 experiment was designed using a chicken embryo model.

The respiration of a chicken embryo occurs through gas exchange in the highly vascularized CAM [110]. This experiment was designed to vary the ambient oxygen available to the CAM for gas exchange to induce a state of hypoxia, and then recovery (normoxia) for the demonstration of relative blood oxygenation. A similar experiment by Ferrer Ortas et al. [53] accomplished hypoxia and recovery by mounting zebrafish embryos in agarose gel and sealing them from oxygen with a coverslip to induce hypoxia. The coverslip was then removed to allow for recovery [53]. A similar approach was not possible with CAM as the capillary beds are fragile, and the weight of a coverslip causes vessel occlusion over time. This motivated the need to design a custom holder to modulate ambient oxygen, referred to as a 'hypoxia holder' in this work. Additionally, it was important to design the holder such that all elements in the optical path remain constant throughout the experiment. As a result, the holder was designed with static imaging windows. The hypoxia holder enabled the manipulation of the internal ambient oxygen content in order to induce hypoxia and recovery in the chicken embryo for relative blood SO_2 measurement.

6.3 Methods

6.3.1 Hypoxia Holder

The hypoxia holder (shown in Figure 6.1) was built using a waterproof ABS project box (Zulkit, Waterproof IP65 ABS Project Box). Three circular imaging windows are sealed with glass coverslips and four ventilation holes are opened to allow for airflow, or sealed with silicon plugs (T Tulead, 16mm/0.63 Hole Plug). One food grade oxygen absorber packet (Brensten, 300cc Oxygen Absorbers) is placed inside the hypoxia holder to reduce ambient oxygen gas through the rusting of iron powder. This oxidization reaction generates heat, as a result, condensation can form on the glass imaging windows and prevent imaging. This was resolved by adding moisture absorbing food grade silica beads (Fonday, Silica Gel Desiccant) into the hypoxia holder. Figure 6.2 illustrates a 17 day old chicken embryo within the hypoxia holder surrounded by the oxygen absorber, silica gel beads and sensors, as well the holder in an open and closed configuration.

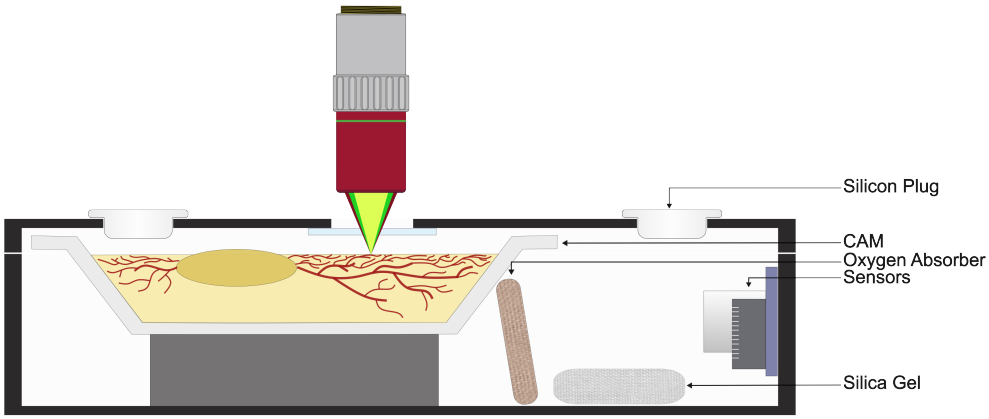


Figure 6.1: Diagram of the hypoxia holder.

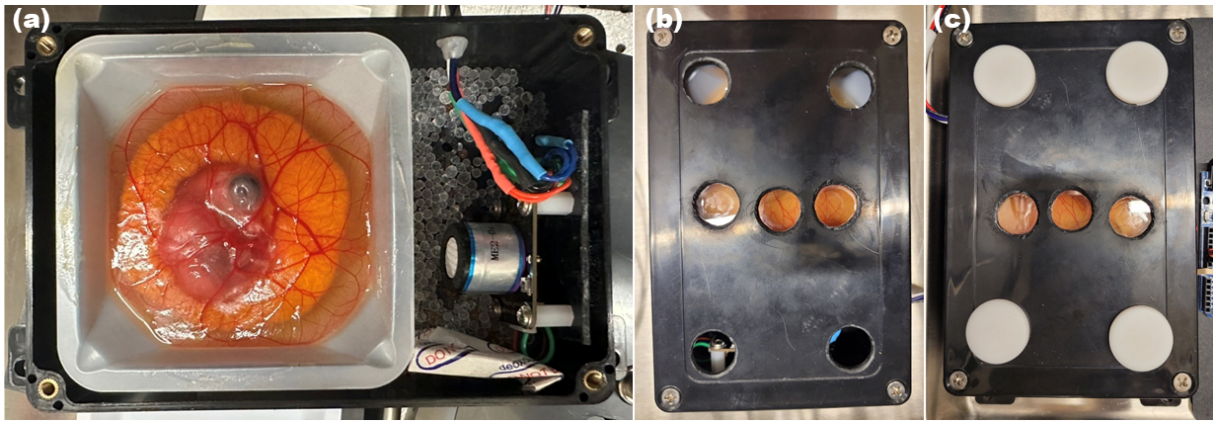


Figure 6.2: Photos of the hypoxia holder in use. (a) shows a 17 day old chicken embryo within the holder, with the oxygen absorber packet, silica gel beads, and sensors. (b) shows the closed holder with open airflow vents, and (c) shows the closed vents. The CAM is visible in (b) and (c) through the imaging windows.

6.3.2 Hypoxia Holder Sensors

During an experiment, it was important to monitor the internal environment of the hypoxia holder. Therefore, an oxygen sensor (DFRobot, SEN0322) as well as a temperature and humidity sensor (Sparkfun, SEN-18364) were implemented. Data was logged at 30 second intervals using an Arduino Uno and monitored throughout the experiment. The oxygen sensor data was used to determine intervals for data collection. In early iterations of this experiment, the temperature and humidity data was valuable to determine the amount of oxygen and moisture-absorbing materials to avoid condensation on the imaging windows.

Both sensors used I2C communication protocols with open source Arduino libraries [111][112] which facilitated ease of implementation when interfacing with the sensors. The temperature and humidity sensors did not require calibration, and the oxygen sensor was calibrated using the open source library and protocol specified by the data sheet [113]. The primary purpose of the sensors was to catalog the relative change in the environment throughout the experiment. Table 6.1 highlights relevant specifications of the sensors. The most notable specification is the $\leq$ 15 second response time of the oxygen sensor. This defines the maximum time the sensor requires for changes in the ambient oxygen to be reflected in the sensor readings. This has the potential to create slight delays in sensor readings, particularly when the ambient oxygen changes rapidly when the seals of the hypoxia holder are opened for recovery. Using a 30 second polling interval of the sensor was designed to reduce the impacts of a $\leq$ 15 second response time.

Sensor	Resolution	Accuracy	Range	Response Time
Oxygen	0.15%	Not Specified	0 - 25%	$\leq$ 15 s
Temperature	0.01 °C	±0.5 °C	-15 - 50 °C	Not Specified
Relative Humidity	0.024%	±4%	0 - 80%	<8 s

Table 6.1: Hypoxia holder sensor specifications [114][113].

6.3.3 Experimental Methods

According to the Canadian Council on Animal Care (CCAC), scientific work using embryos do not require ethics protocols to be approved by an animal care committee [115]. Bird embryos demonstrate sustained EEG activity at >80% incubation time, suggesting consciousness and pain perception [116]. In this work, the maximum age of imaging is day 17, which is 80% of mortality, to avoid conscious suffering and enable imaging of

developed vasculature in the CAM which occurs in older chicken embryos. This is the recommended approach based on discussion with animal care and research ethics personnel at the University of Waterloo.

A series of multi-wavelength PARS images are collected of the same capillary bed structure to ensure variation in the ratio of non-radiative signal is a result of changing oxygen saturation, and not variation in oxygen diffusion or supply based on the capillary location. Imaging the same 128 μm x 128 μm area of capillary beds poses challenges due to the motion of the unanaesthetized CAM and the slowing or stopping of blood flow of the chosen imaging region as the CAM enters hypoxia. As a result, the same capillary beds could not be imaged across a >3 hr experiment. The most dramatic change in ambient oxygen occurs during the recovery from hypoxia when the holder is opened and room oxygen fills the holder, allowing the blood to re-oxygenate. The results presented below contain eleven datasets total, with seven datasets from the same capillary bed location before and during recovery.

6.3.4 Image Processing

Angiography Images

When imaging at video rates, individual red blood cells are captured moving through vessels. Averaging sequential images of flowing red blood cells enables the generation of angiography images, which trace the path of the red blood cells through vessels and provides a stronger sense of vessel structure than individual frames. Angiography images also mitigate absorption variation of individual red blood cells, as discussed in Chapter 5.

Due to the confocal nature of PARS, the heartbeat of the chicken embryo causes the CAM vessels to move in and out of focus. To address this, the CAM was aligned such that optimal focus occurs when the heart beats, and the flow of red blood cells is increased. The improved focus and increased number of red blood cells in the frame results in the average non-radiative intensity of the frame to increase cyclically with heartbeat. Angiography images are generated by detecting the frame with maximum average non-radiative intensity and averaging this frame with the 5 frames on either side of the maximum. This generates angiography images which are centered around the maximum of a heartbeat event.

Ratio of Non-Radiative Images

Initially, the ratio of the angiography images was determined using the equation 6.1, which divides the 558 nm non-radiative intensity by the 532 nm non-radiative intensity, along

with a relaxation parameter (γ). When taking the ratio of images, background and noise can become magnified if near-zero values occur in the denominator, introducing substantial outliers. The intention of the relaxation parameter is to reduce the impacts of these infinite outliers by adding a small scalar value to the denominator. Unfortunately, the relaxation parameter was insufficient. While the expected trends could be observed, data distributions were highly overlapping due to the lack of robustness of Equation 6.1 against outliers.

$$Ratio = \frac{I_{558}}{I_{532} + \gamma} \tag{6.1}$$

Equation 6.2 is a proportional (fractional) ratio, which is bounded between 0 and 1. This approach is robust against infinite outliers since the denominator contains both 558 nm and 532 nm non-radiative intensity. This ratio approach was implemented for the results presented later in this chapter. The robustness of this approach reduced the impacts of noise and background, and enabled separability between data distributions.

$$Ratio = \frac{I_{558}}{I_{532} + I_{558}} \tag{6.2}$$

Otsu's Method for Image Segmentation

Another approach for noise reduction is segmenting images to remove the background. This is implemented using Otsu's Method [117], which is a well-established approach in image processing to separate an image into objects and background. Briefly, this method converts the image into a gray-scale histogram of pixel intensity and determines a scalar threshold to optimally separate the histogram without *a priori* knowledge. Then the threshold is used to separate objects from background in the image space through image binarization based on pixel intensity. Otsu's method is non-parametric and unsupervised, enabling ease of use in a wide variety of applications. For each angiography image, Ostu's method is used to determine a threshold. This threshold is used to generate a binary mask from the angiography image, which is applied to the ratio image to remove the background.

Overall Image Processing Workflow

Non-radiative angiography images are generated for both 558 nm and 532 nm excitation using the chicken embryo heartbeat. The ratio of these images is then taken using Equation 6.2. In parallel, Otsu's segmentation is used to generate binary masks for both 558 nm

and 532 nm angiography images. The union of these masks is taken, and this combined mask is applied to the ratio image to remove background pixels. The remaining pixels in the ratio image are averaged to determine an average intensity of non-radiative ratio per image. This value represents a single data point in a dataset.

6.4 Results & Discussion

6.4.1 Hypoxia Holder Results

Figure 6.3 shows the oxygen, temperature and relative humidity throughout a hypoxia and recovery experiment. Deoxygenation within the hypoxia holder occurs over ∼2.5 hours as the ambient oxygen within the holder drops from from ∼21% (typical room oxygen content) to ∼3%. The rate of deoxygenation can be increased by adding more oxygen absorbing material, however this introduces more heat to the holder which can cause condensation.

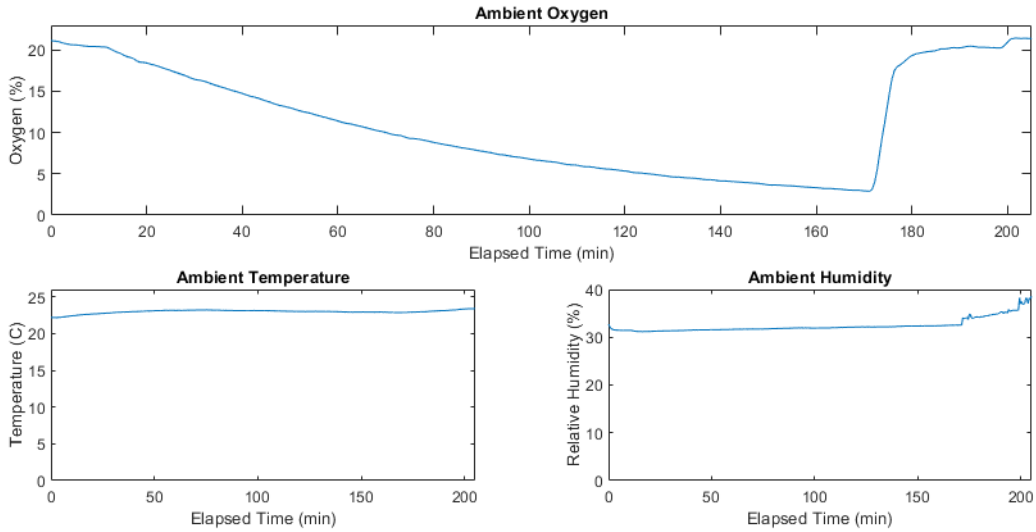


Figure 6.3: Illustration of the ambient oxygen, temperature and relative humidity inside the hypoxia holder throughout an *in vivo* CAM experiment.

Figure 6.3 illustrates the stability of temperature, with a slight increase near the end of the experiment. This increase corresponds with the increase in relative humidity. It is hypothesized that when the hypoxia holder seals are removed, the oxygen absorber rapidly

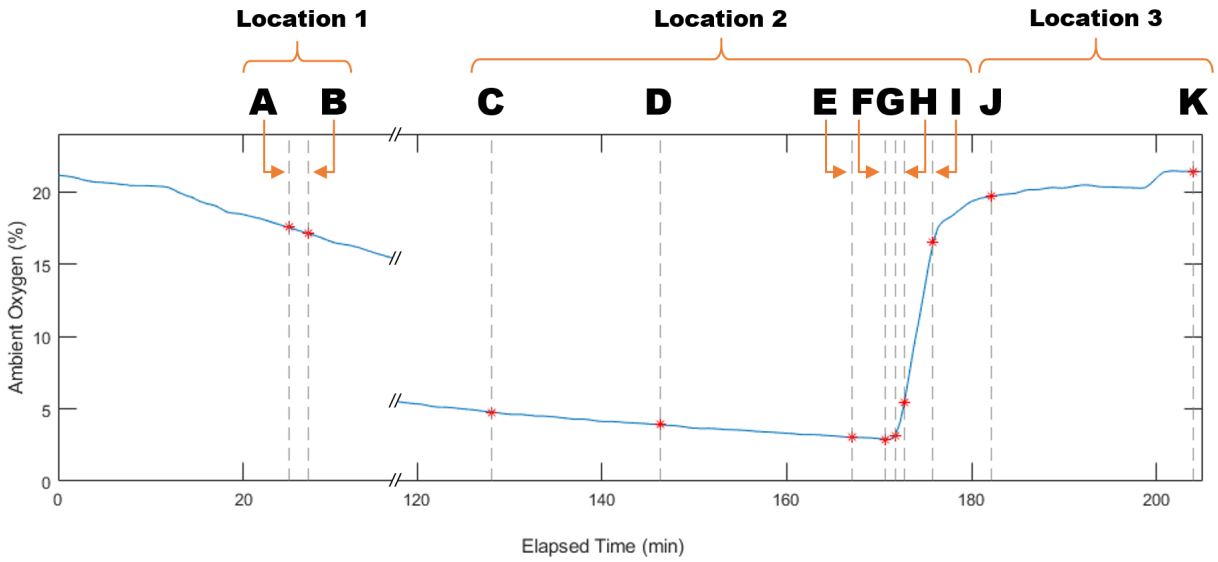


Figure 6.4: Datasets of multi-wavelength PARS images (A-K) are captured at three adjacent locations in the CAM. The occurrence of datasets are labeled across the ambient oxygen of the hypoxia holder.

begins to oxidize and generate heat. Since the hypoxia holder is no longer sealed, external moisture can enter the holder and humidity increases with the additional heat. Fortunately, this slight increase in humidity did not impact the imaging window.

6.4.2 *In vivo* Blood Oxygenation Results

Figure 6.4 illustrates the eleven different datasets which were acquired throughout the hypoxia and recovery of a chicken embryo at three different locations within the same region of the CAM. Datasets A-E and J-K each contain ∼610 interlaced images at various points in hypoxia and normoxia. Datasets F-I contain ∼1220 interlaced images captured while the seals are removed and during the recovery from hypoxia. All datasets contain images of 128 μm x 128 μm using 20 nJ of excitation pulse energy for both 532 nm and 558 nm.

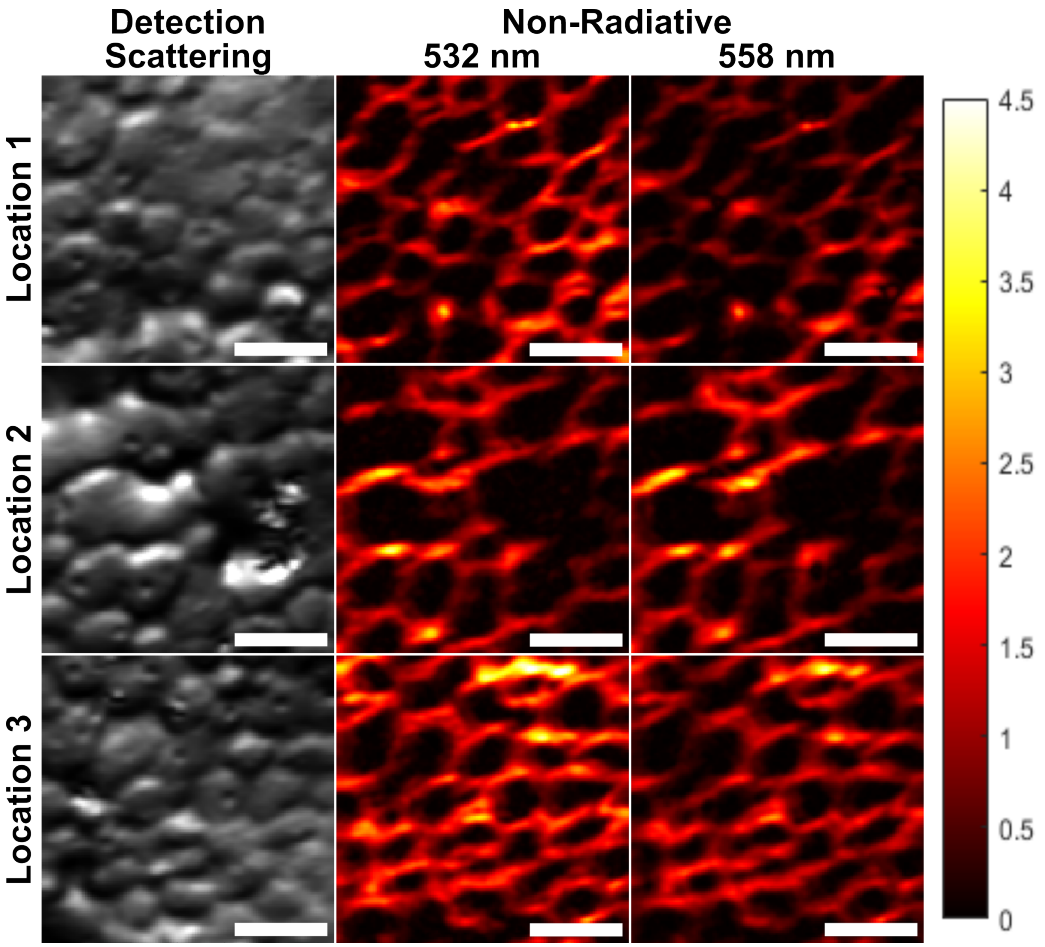


Figure 6.5: Detection scattering and non-radiative angiography images of all three captured CAM locations during the hypoxia experiment. The field of view is 128 μm x 128 μm with a scale bar of 40 μm.

Imaging Location

As mentioned previously, challenges arise when imaging the identical vascular region of an unanaesthetized CAM. Throughout this experiment, the CAM was imaged at three different locations shown in Figure 6.5, illustrates detection scattering and non-radiative angiography images.

To ensure that changes in non-radiative intensity were not caused by a change in location, it was important to show a change in intensity across the same location. In an ideal case, this would be achieved across the entire experiment, however this was not possible for reasons discussed previously. Seven datasets (C-I) were captured in the same location, as illustrated by Figure 6.6. While slight motion is inevitable, the same key structural features can be seen in all images. This illustrates that these results capture data from the same vascular structures.

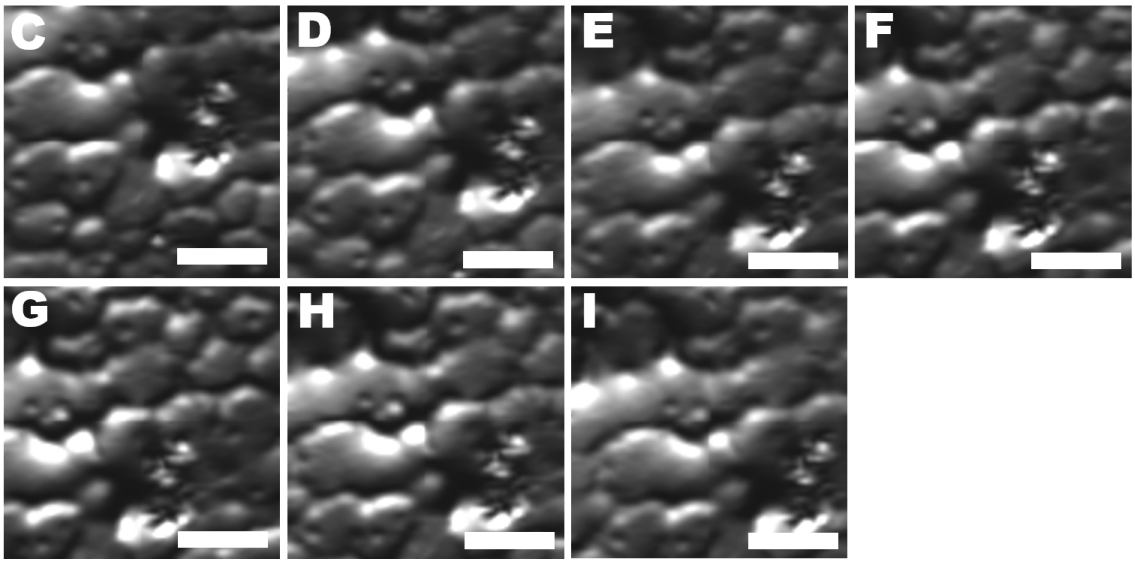


Figure 6.6: Detection scattering across hypoxia datasets C-I illustrating the imaging of the same region based on structural features. The field of view is 128 μm x 128 μm with a scale bar of 40 μm.

Angiography Images and Segmentation

Figure 6.7 shows examples of individual heartbeat angiography images for 558 nm and 532 nm excitation, as well as their image segmentation masks. White illustrates the vessels and black the background. This matches the vessel structure in the non-radiative images. All non-radiative images use the same colour scale.

Figure 6.7 illustrates differing connectivity of vessel structures between the individual heartbeat angiography images from datasets F and G. This is due to the randomness of red blood cell flow throughout the capillaries. Highly connected vessels have higher red blood cell flow than sparsely connected vessels.

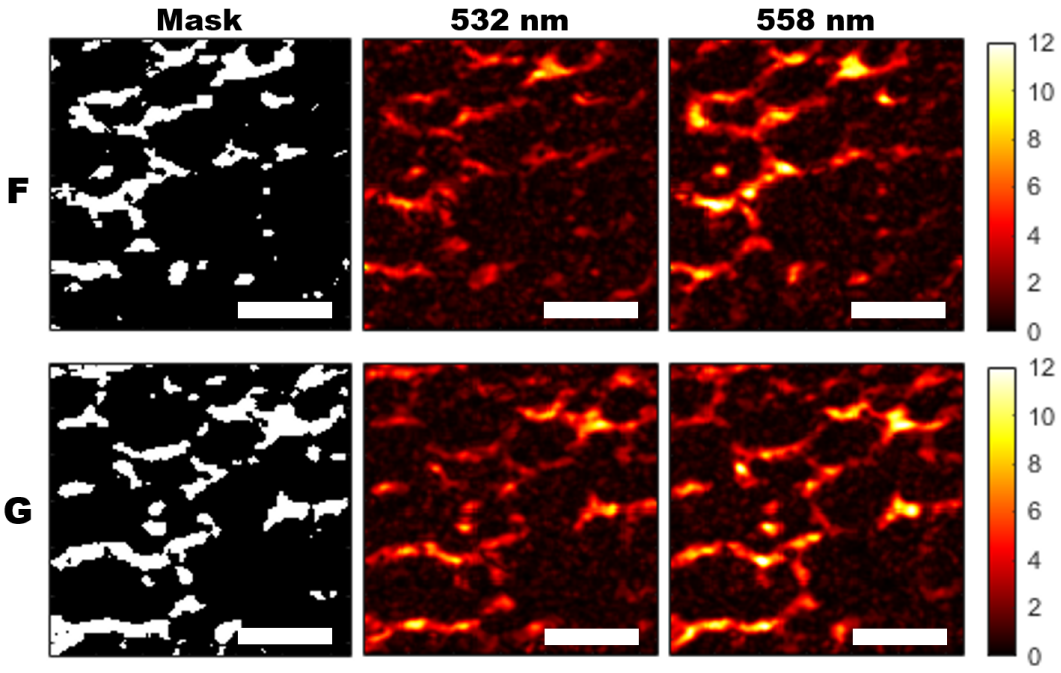


Figure 6.7: Segmented mask and non-radiative angiography images for 532 nm and 558 nm for datasets F and G. The field of view is 128 μm x 128 μm with a scale bar of 40 μm.

These angiography images also highlight the ability of both excitation wavelengths to image the same vascular structures. As discussed in Chapter 3, 558 nm has a slightly higher resolution and thus higher fluence than 532 nm. This is noticeable in Figure 6.7 as both 532 nm images have overall lower intensity when using the same colour scale as 558 nm. Since this experiment focuses on demonstrating relative change of absorption across oxygenation levels, the effect of this variation in fluence is mitigated.

Non-radiative Ratio During Hypoxia and Recovery

As shown in Figure 2.2, 532 nm is a near-isosbestic point such that the change in absorption between oxy- and deoxy-hemoglobin is minimal. However, 558 nm has a high absorption for deoxy-hemoglobin and a decreased absorption for oxy-hemoglobin. As a result, the expected behaviour for non-radiative signals is that the ratio of $\frac{I_{558}}{I_{532}+I_{558}}$ will increase in a state of hypoxia and decrease during normoxia (recovery).

Figure 6.8 illustrates the average non-radiative intensity ratio captured across all eleven datasets. The distributions of non-radiative ratio for each dataset is visualized using box plots (box and whisker plots). The central red line indicates the median, and the bottom and top of the blue box indicates the 25th and 75th percentile. When notches in the box do not overlap, this indicates a 95% confidence that the true medians differ. Outliers are represented with red '+' markers [109]. The ambient oxygen within the holder is illustrated at the time points which these datasets were captured. Overall, the expected trend is shown, such that higher oxygenation corresponds with a lower non-radiative ratio, and a higher ratio corresponds with hypoxia.

The importance of power compensation is illustrated in Figure 6.8 particularly when comparing the non-radiative ratio of datasets A and B. The time difference between A and B was two minutes, and the ambient oxygen for both was 17%. However, the non-radiative ratio is substantially higher in B compared to A. The incoming excitation power is captured on the power compensation photodiode as discussed in Chapter 3. Figure 6.8 compares these excitation powers, and it is evident that dataset B has a higher 558 nm excitation power than surrounding datasets, and a slightly lower 532 nm excitation power. This artificially increases the non-radiative ratio.

When power compensation is applied, the excitation power data is normalized with respect to all eleven datasets. This enables the variation of input power to be compensated for both individual excitation pulses as well as bulk power variation between datasets which can be caused by SRS power drift or operator error. Figure 6.9 shows the change in non-radiative ratio across hypoxia and recovery with power compensation applied, which corrects the artificial increase of ratio in dataset B. With power compensation, the distributions of A and B are highly overlapping which is expected from datasets both captured at 17% ambient oxygen two minutes apart. This result highlights the importance of power compensation to properly capture relative blood SO_2.

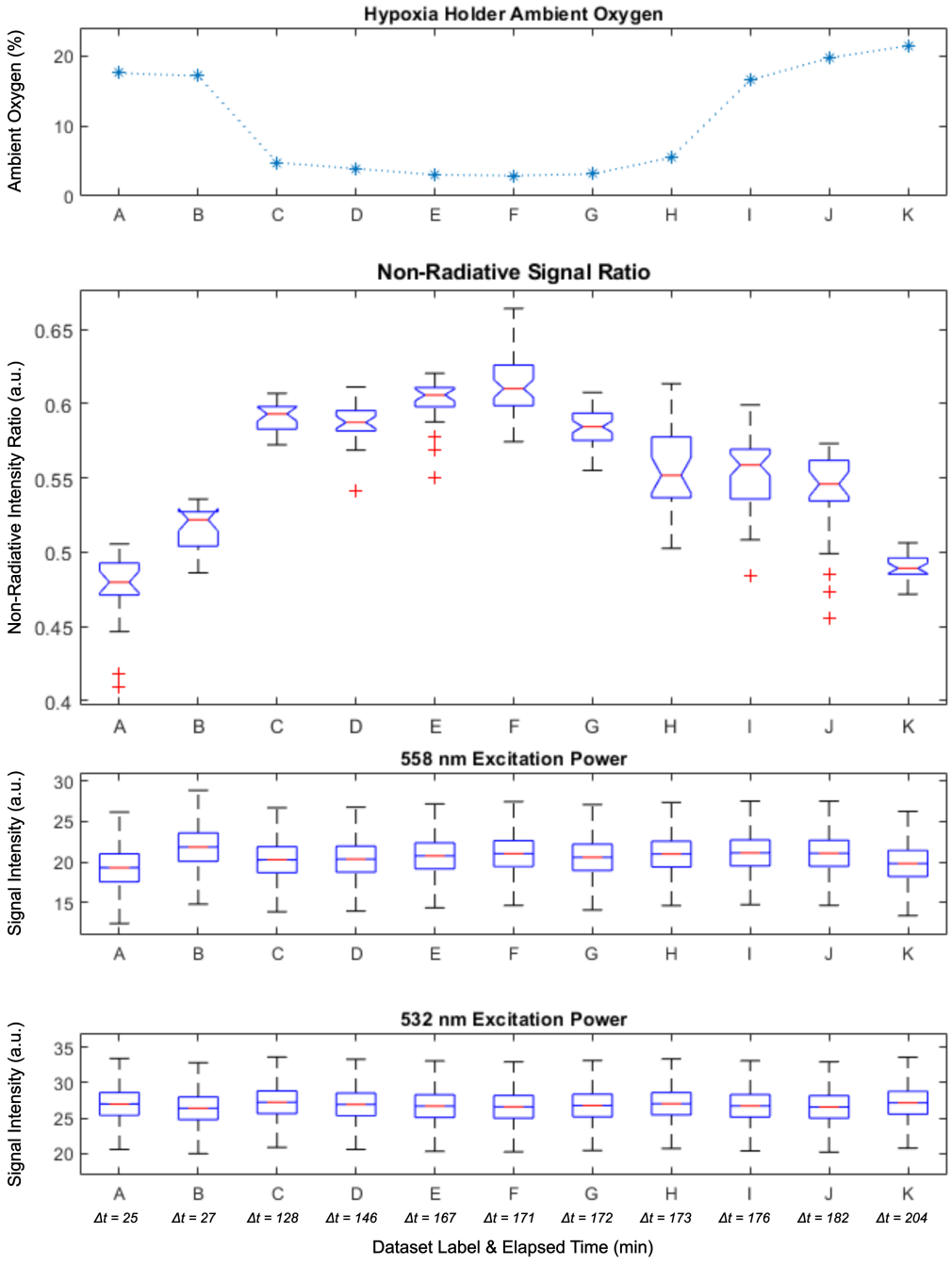


Figure 6.8: CAM hypoxia and recovery experimental results without power compensation. For each dataset labeled A-K, the ambient oxygen, non-radiative ratio and input excitation power for 558 nm and 532 nm are illustrated.

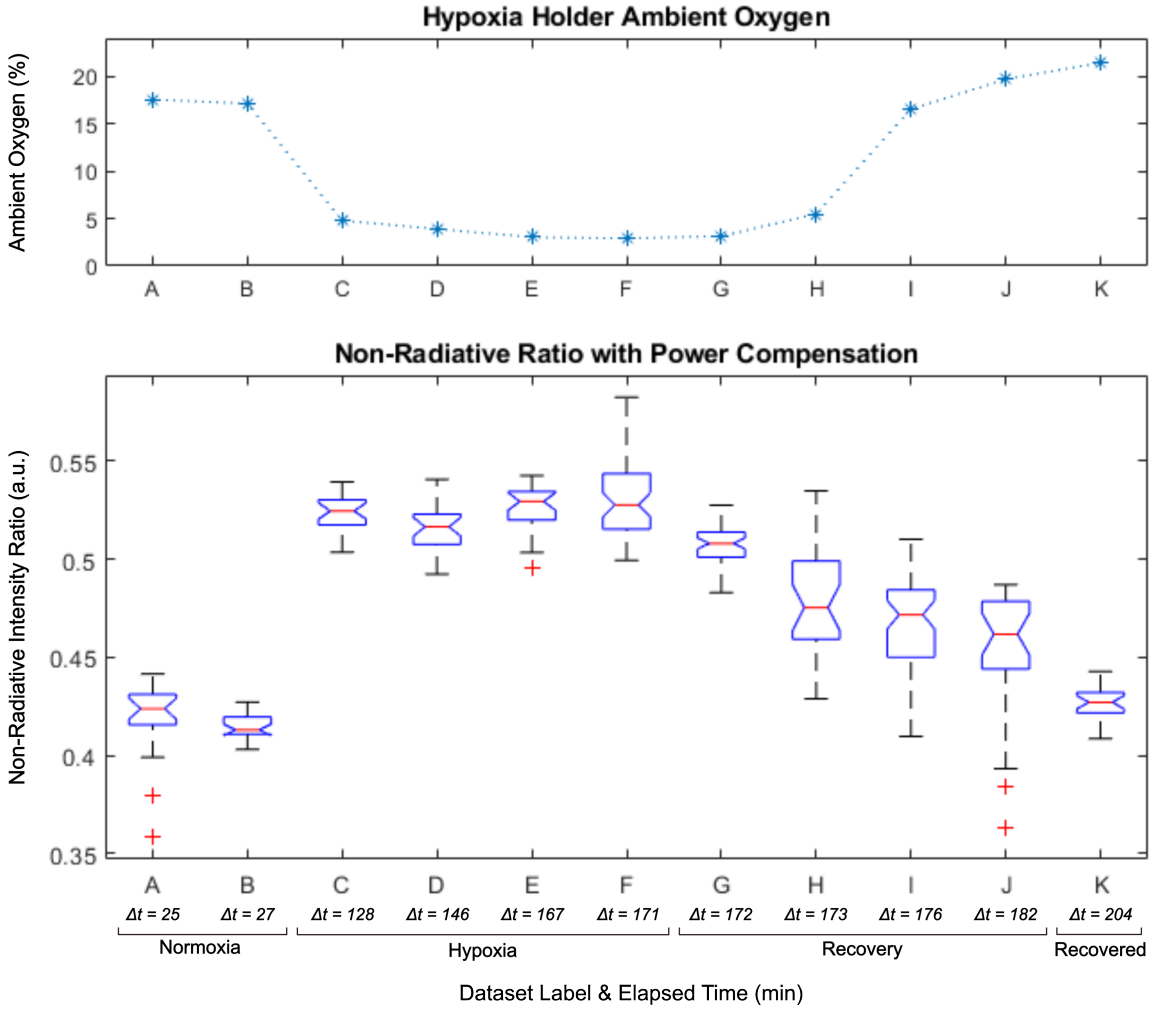


Figure 6.9: CAM hypoxia and recovery experimental results with power compensation. For each dataset labeled A-K, the ambient oxygen and power compensated non-radiative ratio are illustrated.

This experiment captured data across a range of ambient oxygen levels, starting from 17% which is reduced to ∼3%, and is then returned to 21% during recovery. The first two datasets were captured at 17% ambient oxygen. The current design of the hypoxia holder requires that the silicon plugs are installed before the lid is put in place to minimize the force needed to remove the plugs. This ensures the imaging location is not lost during the critical recovery phase of the experiment. As a result, there is a time delay between the decrease in ambient oxygen and the capture of the first dataset as time is required to locate a suitable imaging area.

During regular chicken embryo development, respiration occurs within a shell (*in ovo*) that has limited diffuse conductance. Oxygen consumption increases as the embryo grows, and peaks in the final days of development. *In ovo* chicken embryos naturally experience a degree of hypoxia when incubated in 21% ambient oxygen, which prompts pipping and hatching. Additionally, the oxygen affinity of embryonic hemoglobin varies throughout development to account for oxygen limitations [118]. However, in this work the chicken embryo is removed from the shell (*ex ovo*) and gas exchange in the CAM occurs directly with ambient air. Work by Reeves [118] suggests that chicken embryos in the second phase of development (day 8-18) attain 100% SO_2 at 100 mmHg of partial pressure oxygen (PO_2). Assuming dry, atmospheric air at sea level with a pressure of 760 mmHg (1 atm), 100 mmHg of PO_2 occurs at 13.15% oxygen. This suggests that 17% ambient oxygen does not induce hypoxia *ex ovo*, and the datasets captured in this range can be used to establish a baseline of normoxia. Additionally, ambient oxygen below 13.15% is expected to induce hypoxia.

The ability to capture the relative change in blood oxygenation *in vivo* with the multi-wavelength PARS system is shown in Figure 6.9. The ratio distributions of normoxia (A,B and K) show clear separability from the ratio distributions of hypoxia (C-G). Additionally, the change in ratio is illustrated as the chicken embryo recovers from the state of hypoxia as shown in the decrease of ratio between G and K. Datasets with wider distributions, such as F, H, I and J are due to an increase of bulk motion.

Another success of these result is the ability to compare the non-radiative ratio across adjacent locations in the CAM. Three different imaging locations within the same region of the CAM are presented in these results as discussed previously, and results follow the expected trend irregardless of the location. Relative SO_2 is determined by taking an image-based ratio of the intensity of non-radiative signal from two different wavelengths of excitation. A strength of this approach is that the system does not rely directly on signal magnitude. When imaging at different locations, variables such as the number of vessels, as well as their size and depth can impact the magnitude of non-radiative signal. However, these structural factors introduce the same variation in intensity for

both excitation wavelengths. Taking an image-based ratio of both wavelengths is expected to mitigate substantial variation caused by structural factors when imaging at different locations. Another concern is the variation in SO_2 between the major vessels which supply the CAM [119], and rate of oxygen diffusion. Imaging small 128 μm x 128 μm adjacent locations all in the same small region ensure that the imaged capillaries are supplied by the same major vessel. Also, this work images capillary beds at the surface of the CAM where respiration occurs, and the ambient oxygen is uniform across this surface. This does not entirely mitigate variation which could arise from variability in capillary transit time of individual RBCs [119], which impacts oxygen diffusion. It is possible for this to be location dependent, however this random variation will also occur within a single location, which suggests that trends over a large range of oxygenation levels should still be detectable. Further experimentation is required to determine the accuracy of measurements compared between multiple locations, however present results show feasibility.

Finally, a second experiment was conducted where a different chicken embryo of 17 days old was imaged on a different day with pulse energies of 20 nJ. The imaging system was re-aligned and the same experimental procedure was followed, with the exception that the minimum ambient oxygen concentration was 9% and the experiment lasted only 1.5 hours. As shown in Figure 6.10 the absorption ratio follows the expected trend based on the ambient oxygen concentration. Unfortunately, data from the beginning of this experiment could not be reconstructed due to a data acquisition bug, therefore these datasets were excluded. Although this experiment captured data from a smaller range of oxygenation, the hypoxia and recovery of the chicken embryo remains evident. This demonstrates feasibility of these results across different chicken embryos, on different days and with different system alignments.

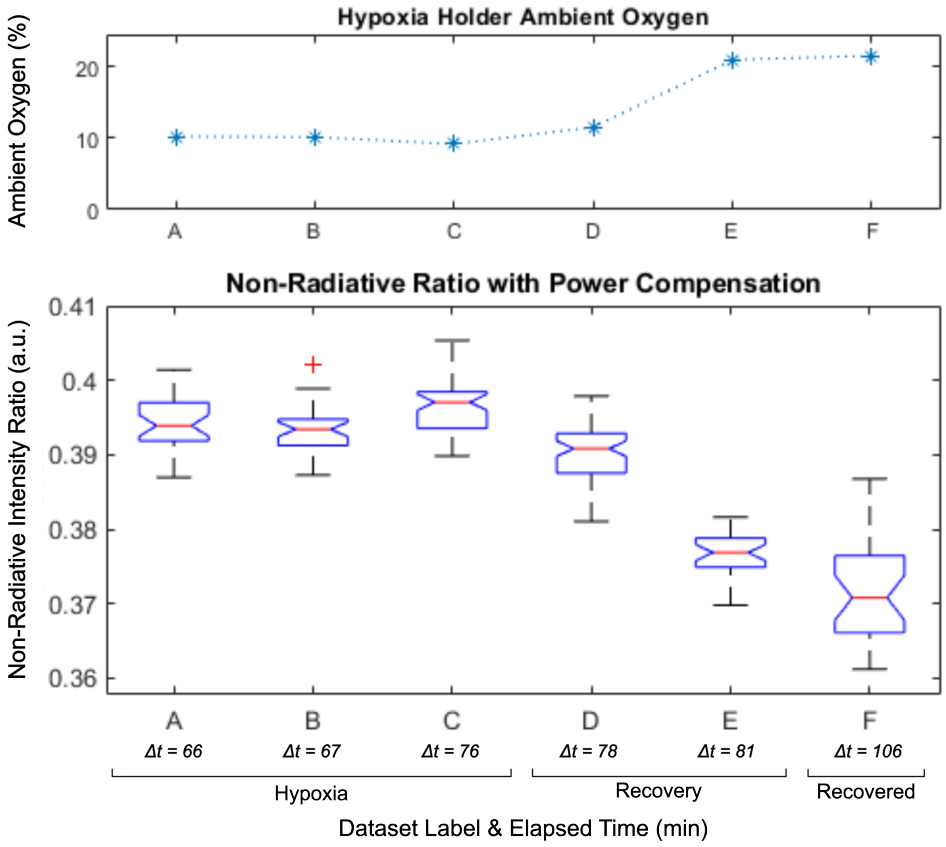


Figure 6.10: Results from a second CAM hypoxia and recovery experiment, conducted on a different day, with a different chicken embryo and a different system alignment. For each dataset labeled A-F, the ambient oxygen and power compensated non-radiative ratio are illustrated.

6.5 Conclusion

In vivo work in animal models is a critical stepping stone towards the application of technology in humans. The CAM of a chicken embryo provides a valuable imaging target due to the dense surface-level vascular networks. Building on the work by J.A. Tummons Simmons et al. [70], video rate multi-wavelength *in vivo* PARS images were captured at various points during the hypoxia and recovery of a chicken embryo.

This chapter highlights the success of the custom hypoxia holder to modulate the ambient oxygen concentration available to the chicken embryo. Reducing ambient oxygen through the use of iron powder oxidation (oxygen absorbers) and a confined space induced a controllable state of hypoxia, and sensors were implemented to log the state of the internal environment. This was used to determine the expected trends in optical absorption of deoxy- and oxy-hemoglobin measured by the non-radiative PARS contrast from 532 nm and 558 nm excitation.

The multi-wavelength PARS *in vivo* system was successful in showing relative SO_2 in the CAM of a chicken embryo, as the non-radiative ratio followed the expected trends of hypoxia and recovery. The ability to separate between deoxy- and oxy-hemoglobin is illustrated through the lack of overlap between distributions of datasets of hypoxia and normoxia, however the small number of replicates in this study limits the statistical definitiveness of these results. Additionally, the importance of power compensation is highlighted in this data through the adjustment of an artificially inflated ratio as a result of increased excitation power. These experimental methods lay the groundwork for further applications of multi-wavelength PARS for functional vascular imaging which work toward accurate SO_2 and the demonstration of MRO_2.

6.6 Future Work

The presented results examine the overall variation of non-radiative absorption for each dataset. However, future work can also examine the subtle changes in oxygen saturation within a single dataset, particularly during recovery from hypoxia. Another metric that can be extracted from this dataset is the change in heartbeat, which could provide an additional biomarker of the physiological change occurring during hypoxia.

To reduce bulk motion of the chicken embryo, which causes noise and makes imaging the same vessels challenging, anaesthetic can be applied through injection or by modifying the hypoxia holder for an inhalable anesthetic. Additionally, the application of advanced

image processing algorithms has the possibility to remove heartbeat and bulk motion artifacts. Both these efforts would remove outliers and improve accuracy. Advanced image segmentation approaches and denoising also have the potential for improving accuracy.

Red blood cell motion can be seen in the video rate images collected from this experiment. Current efforts in the lab are working towards the application of particle velocimetry such that red blood cell flow can also be extracted from this data. Combining blood flow and blood oxygenation lays the groundwork for the first demonstration of metabolic rate of oxygenation (MRO_2) with PARS.

Future work also involves increasing the number of replicates in this experiment to assess the repeatability of the results on a large number of different chicken embryos. This would enable a statistical analysis to be performed to determine if the change in non-radiative ratio is statistically different between normoxia and hypoxia, and assess the statistical sameness between ratios of the baseline normoxia and the recovered state. The first trial captures two baseline normoxia datasets, however a baseline could not be captured in the second trial. Additionally, it would be valuable to capture data at fixed ambient oxygen levels (eg. 21%, 15%, 10%, 5%) during hypoxia to statistically assess differences in measurements at smaller ambient oxygen level increments.

To determine the number of replicates needed for these future studies, a power analysis is implemented based on the mean (μ) and standard deviation (σ) of the data presented in figure 6.9 and 6.10 using the free G*Power software [120]. Given the different levels of hypoxia (3% and 9% ambient oxygen) in each experiment, resulting in differing means, the power analysis is performed on experiment 1 and 2 separately. To analyze the differentiation between hypoxia and normoxia, these datasets were combined such that in experiment 1 hypoxia of 3% ambient oxygen is shown in datasets C-F ($\mu = 0.526$, $\sigma = 0.0169$) and normoxia in A, B, and K ($\mu = 0.4202$, $\sigma = 0.0135$). The effect size was determined based on these statistics, and this analysis assumes a paired t-test which uses a required power level ($1-\beta$) of 0.95 and a significance level (α) of 0.05. Based on experiment 1 statistics, a replicate size of 3 is necessary to demonstrate a statistical difference between hypoxia (3%) and normoxia. Experiment 2 only reached a hypoxia level of 9%, combining datasets A-C for hypoxia ($\mu = 0.3959$, $\sigma = 0.0207$) and dataset F is normoxia ($\mu = 0.377$, $\sigma = 0.0074$). The G*Power analysis using the same assumptions and experiment 2 statistics determined a replicate size of 15. While the hypoxia experiment to 3% ambient oxygen takes twice the time of the 9% experiment, it requires only 3 replicates. Overall, a 3 replicate study to 3% ambient oxygen is the most time efficient approach to be used in future work. However, subsequent studies will need to assess smaller increments of hypoxia, and the power analysis of experiment 2 highlights that required sample size is expected to increase when demonstrating the statistical difference between smaller increments of hypoxia.

Chapter 7

Conclusion

The implementation of independent excitation paths enabled improved alignment of 532 nm and 558 nm in order to achieve consistent and reliable multi-wavelength *in vivo* PARS imaging in the CAM vasculature of a chicken embryo. Separate excitation paths also enabled the interlacing of both excitation wavelengths for near-simultaneous imaging of the same structures. The introduction of polarization alignment improves the 558 nm generation using SRS, which is important for successful, and quantitative, *in vivo* imaging. Power compensation is implemented to account for pulse-to-pulse variation in excitation power, as well as power drift which is critical for comparing quantitative measurements used for SO_2 determination. The multi-wavelength system achieves the objectives of consistency and reliability in multi-wavelength *in vivo* PARS vascular imaging.

The goal of the *in vitro* blood and flow phantom work was to validate results from the multi-wavelength PARS system with blood at known oxygenation levels. In the absence of suitable results from the *in vitro* phantom study, an accuracy metric is currently unavailable. However, this thesis work has furthered efforts towards achieving this through the development of a low-cost, time-efficient blood oxygenation and deoxygenation protocol, and through the knowledge gained in the iterative design of flow phantoms. Further work is required to implement a successful flow phantom, however the blood oxygenation and deoxygenation protocol serves as a valuable contribution to future experiments.

Finally, the ability to measure a relative change in SO_2 was successfully shown *in vivo* through the hypoxia study. A custom hypoxia holder was developed which could modulate the internal ambient oxygen levels, inducing a state of hypoxia, and then recovery in the CAM of a chicken embryo. These results successfully illustrate a relative change in the ratio of non-radiative intensity which followed expected trends of hypoxia and recovery.

These results were also shown in a second experiment. The successful results showing relative change in absorption ratio *in vivo*, but the unsuccessful results in the flow phantom validate that the issues with the *in vitro* experiments are a result of challenges with the flow phantom, not the multi-wavelength PARS system. The successful *in vivo* results shown in chicken embryos serve as a valuable stepping stone towards imaging more complex *in vivo* targets such as mouse retina.

Limitations of this work include the slight variation in resolution and depth of focus between the 532 nm and 558 nm excitation wavelengths. This does not limit the ability to capture relative change in SO_2, however, this will be an important system improvement in future work to capture absolute SO_2 measurement. The lack of results in the flow phantom limited the determination of a PARS-SO_2 empirical model or the ability to assess SO_2 measurement accuracy against a gold standard ground truth. Finally, the *in vivo* results shown in chicken embryo are limited due to the small number of trials of this experiment. In order to perform statistical analysis to definitively determine difference between measurements of non-radiative ratio in normoxia, hypoxia and recovery, a larger number of trials is required. Increasing the number of replicates is also necessary to assess repeatability. As well, a chicken embryo is a highly idealized imaging target, the CAM is flat and has blood vessels that are at, or close to the surface. Future work will need to explore more complex *in vivo* imaging targets.

PARS is a unique imaging platform that can capture non-contact, label-free, absorption-based images. This technology has strong potential to provide an SO_2 imaging platform which can simultaneously capture non-radiative and radiative relaxation, with the hopes of leveraging radiative contrasts to un-mix confounding bio-molecules and provide complimentary structural information. The ultimate goal of this work is to further efforts towards accurate PARS SO_2 imaging which achieves ISO accuracy standards [15]. This was accomplished by improving reliability and consistency of the multi-wavelength *in vivo* PARS imaging system, advancing efforts for *in vitro* phantom studies, and showing relative SO_2 *in vivo*.

Letters of Copyright Permission

JOHN WILEY AND SONS LICENSE
TERMS AND CONDITIONS

Oct 11, 2024

This Agreement between Sarah J. Werezak ("You") and John Wiley and Sons ("John Wiley and Sons") consists of your license details and the terms and conditions provided by John Wiley and Sons and Copyright Clearance Center.

License Number	5886160465065
License date	Oct 11, 2024
Licensed Content Publisher	John Wiley and Sons
Licensed Content Publication	Wiley Books
Licensed Content Title	Introduction
Licensed Content Date	Oct 2, 2012
Licensed Content Pages	15
Type of use	Dissertation/Thesis
Requestor type	University/Academic
Format	Electronic
Portion	Figure/table
Number of figures/tables	1
Will you be translating?	No

Title of new work	Multi-wavelength Photon Absorption Remote Sensing: Towards Functional Vascular Imaging
Institution name	University of Waterloo
Expected presentation date	Oct 2024
Portions	Figure 1.2
The Requesting Person / Organization to Appear on the License	Sarah J. Werezak
Requestor Location	University of Waterloo 200 University Ave W Waterloo, ON N2L 3G1 Canada Attn: University of Waterloo
Publisher Tax ID	EU826007151
Total	0.00 CAD

Terms and Conditions

TERMS AND CONDITIONS

This copyrighted material is owned by or exclusively licensed to John Wiley & Sons, Inc. or one of its group companies (each a"Wiley Company") or handled on behalf of a society with which a Wiley Company has exclusive publishing rights in relation to a particular work (collectively "WILEY"). By clicking "accept" in connection with completing this licensing transaction, you agree that the following terms and conditions apply to this transaction (along with the billing and payment terms and conditions established by the Copyright Clearance Center Inc., ("CCC's Billing and Payment terms and conditions"), at the time that you opened your RightsLink account (these are available at any time at http://myaccount.copyright.com).

Terms and Conditions

- The materials you have requested permission to reproduce or reuse (the "Wiley Materials") are protected by copyright.

Marketplace

This is a License Agreement between Sarah J. Werezak ("User") and Copyright Clearance Center, Inc. ("CCC") on behalf of the Rightsholder identified in the order details below. The license consists of the order details, the Marketplace Permissions General Terms and Conditions below, and any Rightsholder Terms and Conditions which are included below.

All payments must be made in full to CCC in accordance with the Marketplace Permissions General Terms and Conditions below.

Order Date	08-Oct-2024	Type of Use	Republish in a thesis/dissertation
Order License ID	1533887-1		
ISSN	1083-3668	Publisher	SPIE; S P I E (INTL SOC FOR OPTICAL)
		Portion	Image/photo/illustration

LICENSED CONTENT

Publication Title	Journal of Biomedical Optics	Rightsholder	SPIE
Article Title	Hyperspectral imaging of hemoglobin saturation in tumor microvasculature and tumor hypoxia development.	Publication Type	Journal
		Start Page	44004
		Issue	4
		Volume	10
Author / Editor	Society of Photo-optical Instrumentation Engineers., International Biomedical Optics Society.	URL	https://www.spiedigitallibrary.org/journals/Journal-of-Biomedical-Optics
Date	01/01/1996		
Language	English		
Country	United States of America		

REQUEST DETAILS

Portion Type	Image/photo/illustration	Distribution	Canada
Number of Images / Photos / Illustrations	1	Translation	Original language of publication
Format (select all that apply)	Electronic	Copies for the Disabled?	No
		Minor Editing Privileges?	No
Who Will Republish the Content?	Academic institution	Incidental Promotional Use?	No
Duration of Use	Life of current edition	Currency	CAD
Lifetime Unit Quantity	Up to 499		
Rights Requested	Main product		

NEW WORK DETAILS

Title	Multi-Wavelength in-vivo Photon Absorption Remote Sensing: Towards Non-Contact Label-Free Functional Vascular Imaging	**Institution Name**	University of Waterloo
		Expected Presentation Date	2024-10-31
Instructor Name	Parsin Haji Reza		

ADDITIONAL DETAILS

The Requesting Person / Organization to Appear on the License	Sarah J. Werezak

REQUESTED CONTENT DETAILS

Title, Description or Numeric Reference of the Portion(s)	Figure 10	**Title of the Article / Chapter the Portion Is From**	Hyperspectral imaging of hemoglobin saturation in tumor microvasculature and tumor hypoxia development.
Editor of Portion(s)	Sorg, Brian S; Moeller, Benjamin J; Donovan, Owen; Cao, Yiting; Dewhirst, Mark W	**Author of Portion(s)**	Sorg, Brian S; Moeller, Benjamin J; Donovan, Owen; Cao, Yiting; Dewhirst, Mark W
Volume / Edition	10		
Page or Page Range of Portion	44004	**Publication Date of Portion**	2005-07-01

Marketplace Permissions General Terms and Conditions

The following terms and conditions ("General Terms"), together with any applicable Publisher Terms and Conditions, govern User's use of Works pursuant to the Licenses granted by Copyright Clearance Center, Inc. ("CCC") on behalf of the applicable Rightsholders of such Works through CCC's applicable Marketplace transactional licensing services (each, a "Service").

1) **Definitions.** For purposes of these General Terms, the following definitions apply:

"License" is the licensed use the User obtains via the Marketplace platform in a particular licensing transaction, as set forth in the Order Confirmation.

"Order Confirmation" is the confirmation CCC provides to the User at the conclusion of each Marketplace transaction. "Order Confirmation Terms" are additional terms set forth on specific Order Confirmations not set forth in the General Terms that can include terms applicable to a particular CCC transactional licensing service and/or any Rightsholder-specific terms.

"Rightsholder(s)" are the holders of copyright rights in the Works for which a User obtains licenses via the Marketplace platform, which are displayed on specific Order Confirmations.

"Terms" means the terms and conditions set forth in these General Terms and any additional Order Confirmation Terms collectively.

"User" or "you" is the person or entity making the use granted under the relevant License. Where the person accepting the Terms on behalf of a User is a freelancer or other third party who the User authorized to accept the General Terms on the User's behalf, such person shall be deemed jointly a User for purposes of such Terms.

"Work(s)" are the copyright protected works described in relevant Order Confirmations.

SPRINGER NATURE LICENSE
TERMS AND CONDITIONS

Oct 07, 2024

This Agreement between Sarah J. Werezak ("You") and Springer Nature ("Springer Nature") consists of your license details and the terms and conditions provided by Springer Nature and Copyright Clearance Center.

License Number	5883820403235
License date	Oct 07, 2024
Licensed Content Publisher	Springer Nature
Licensed Content Publication	Nature Nanotechnology
Licensed Content Title	Oxyhaemoglobin saturation NIR-IIb imaging for assessing cancer metabolism and predicting the response to immunotherapy
Licensed Content Author	Zhiguo Fang et al
Licensed Content Date	Sep 11, 2023
Type of Use	Thesis/Dissertation
Requestor type	academic/university or research institute
Format	electronic
Portion	figures/tables/illustrations
Number of figures/tables/illustrations	1

Would you like a high resolution image with your order?	no
Will you be translating?	no
Circulation/distribution	1 - 29
Author of this Springer Nature content	no
Title of new work	Multi-wavelength Photon Absorption Remote Sensing: Towards Functional Vascular Imaging
Institution name	University of Waterloo
Expected presentation date	Oct 2024
Portions	Figure 3
The Requesting Person / Organization to Appear on the License	Sarah J. Werezak
Requestor Location	University of Waterloo 200 University Ave W Waterloo, ON N2L 3G1 Canada Attn: University of Waterloo
Billing Type	Invoice
Billing Address	University of Waterloo 200 University Ave W Waterloo, ON N2L 3G1 Canada Attn: University of Waterloo
Total	0.00 CAD

RightsLink

Sign in/Register

Quantitative Optical Imaging of Oxygen in Brain Vasculature

Author: Emily Rathbone, Dan Fu

Publication: The Journal of Physical Chemistry B

Publisher: American Chemical Society

Date: Jul 1, 2024

Copyright © 2024, American Chemical Society

PERMISSION/LICENSE IS GRANTED FOR YOUR ORDER AT NO CHARGE

This type of permission/license, instead of the standard Terms and Conditions, is sent to you because no fee is being charged for your order. Please note the following:

- Permission is granted for your request in both print and electronic formats, and translations.
- If figures and/or tables were requested, they may be adapted or used in part.
- Please print this page for your records and send a copy of it to your publisher/graduate school.
- Appropriate credit for the requested material should be given as follows: "Reprinted (adapted) with permission from {COMPLETE REFERENCE CITATION}. Copyright {YEAR} American Chemical Society." Insert appropriate information in place of the capitalized words.
- One-time permission is granted only for the use specified in your RightsLink request. No additional uses are granted (such as derivative works or other editions). For any uses, please submit a new request.

If credit is given to another source for the material you requested from RightsLink, permission must be obtained from that source.

BACK CLOSE WINDOW

© 2024 Copyright - All Rights Reserved | Copyright Clearance Center, Inc. | Privacy statement | Data Security and Privacy | For California Residents | Terms and ConditionsComments? We would like to hear from you. E-mail us at customercare@copyright.com

Bibliography

[1] J. M. Cochran, D. R. Busch, A. Leproux, *et al.*, "Tissue oxygen saturation predicts response to breast cancer neoadjuvant chemotherapy within 10 days of treatment," *Journal of Biomedical Optics*, vol. 24, no. 02, p. 1, Oct. 2018, ISSN: 1083-3668.

[2] O. Falou, H. Soliman, A. Sadeghi-Naini, *et al.*, "Diffuse Optical Spectroscopy Evaluation of Treatment Response in Women with Locally Advanced Breast Cancer Receiving Neoadjuvant Chemotherapy," en, *Translational Oncology*, vol. 5, no. 4, pp. 238–246, Aug. 2012, ISSN: 19365233.

[3] M. Suyama, Y. Yoda, Y. Yamamoto, *et al.*, "Oxygen saturation imaging as a useful tool for visualizing the mode of action of photodynamic therapy for esophageal cancer," en, *VideoGIE*, vol. 5, no. 10, pp. 496–499, Oct. 2020, ISSN: 24684481.

[4] M. R. Tomaszewski, M. Gehrung, J. Joseph, I. Quiros-Gonzalez, J. A. Disselhorst, and S. E. Bohndiek, "Oxygen-Enhanced and Dynamic Contrast-Enhanced Optoacoustic Tomography Provide Surrogate Biomarkers of Tumor Vascular Function, Hypoxia, and Necrosis," en, *Cancer Research*, vol. 78, no. 20, pp. 5980–5991, Oct. 2018, ISSN: 0008-5472, 1538-7445.

[5] P. S. Silva, D. M. Marcus, D. Liu, *et al.*, "Association of Ultra-Widefield Fluorescein Angiography–Identified Retinal Nonperfusion and the Risk of Diabetic Retinopathy Worsening Over Time," en, *JAMA Ophthalmology*, vol. 140, no. 10, p. 936, Oct. 2022, ISSN: 2168-6165.

[6] G. Mahmoudinezhad, S. Moghimi, E. Micheletti, *et al.*, "Relationship Between Retinal Oxygen Saturation and the Severity of Visual Field Damage in Glaucoma," en, *Journal of Glaucoma*, vol. 33, no. 10, pp. 728–734, Oct. 2024, ISSN: 1057-0829.

[7] H. Sung, J. Ferlay, R. L. Siegel, *et al.*, "Global Cancer Statistics 2020: GLOBOCAN Estimates of Incidence and Mortality Worldwide for 36 Cancers in 185 Countries," en, *CA: A Cancer Journal for Clinicians*, vol. 71, no. 3, pp. 209–249, May 2021, ISSN: 0007-9235, 1542-4863.

[8] A. Kulkarni, N. Masarkar, S. K. Ray, and S. Mukherjee, "Hypoxia's Function in Cancer," en, in *Hypoxia in Cancer: Significance and Impact on Cancer Therapy*, S. Mukherjee and J. R. Kanwar, Eds., Singapore: Springer Nature Singapore, 2023, pp. 19–39, ISBN: 978-981-9903-12-2 978-981-9903-13-9.

[9] "The cost of vision loss and blindness in Canada," Canadian Council of the Blind, Tech. Rep., May 2021. [Online]. Available: https://www.fightingblindness.ca/wp-content/uploads/2021/05/Deloitte-Final-Acc-of-VL-and-Blindness-in-Canada-May-2021.pdf (visited on 01/14/2024).

[10] W. Liu and H. F. Zhang, "Photoacoustic imaging of the eye: A mini review," en, *Photoacoustics*, vol. 4, no. 3, pp. 112–123, Sep. 2016, ISSN: 22135979.

[11] A. K. Garg, D. Knight, L. Lando, and D. L. Chao, "Advances in Retinal Oximetry," en, *Translational Vision Science & Technology*, vol. 10, no. 2, p. 5, Feb. 2021, ISSN: 2164-2591.

[12] J. A. T. Simmons, S. J. Werezak, B. R. Ecclestone, J. E. D. Tweel, H. Gaouda, and P. H. Reza, *Label-Free Non-Contact Structural and Functional Vascular Imaging using Photon Absorption Remote Sensing*, arXiv:2310.05260 [physics], Oct. 2023.

[13] Z. Hosseinaee, B. Ecclestone, N. Pellegrino, *et al.*, "Functional photoacoustic remote sensing microscopy using a stabilized temperature-regulated stimulated Raman scattering light source," en, *Optics Express*, vol. 29, no. 19, p. 29 745, Sep. 2021, Publisher: Optica Publishing Group, ISSN: 1094-4087.

[14] Z. Hosseinaee, N. Pellegrino, N. Abbasi, *et al.*, "In-vivo functional and structural retinal imaging using multiwavelength photoacoustic remote sensing microscopy," en, *Scientific Reports*, vol. 12, no. 1, p. 4562, Mar. 2022, ISSN: 2045-2322.

[15] *Medical electrical equipment — Part 2-61: Particular requirements for basic safety and essential performance of pulse oximeter equipment*, Geneva, Switzerland, 2017.

[16] L. V. Wang and H.-i. Wu, *Biomedical optics: principles and imaging*, eng. Hoboken, N.J: Wiley-Interscience, 2007, ISBN: 978-0-470-17701-3 978-0-470-17700-6.

[17] L. Hacker, J. Joseph, L. Lilaj, *et al.*, "Tutorial on phantoms for photoacoustic imaging applications," *Journal of Biomedical Optics*, vol. 29, no. 08, Aug. 2024, ISSN: 1083-3668.

[18] T. R. Else, L. Hacker, J. Gröhl, E. V. Bunce, R. Tao, and S. E. Bohndiek, "Effects of skin tone on photoacoustic imaging and oximetry," *Journal of Biomedical Optics*, vol. 29, no. S1, Dec. 2023, ISSN: 1083-3668.

[19] *Medical electrical equipment — Part 2-61: Particular requirements for basic safety and essential performance of pulse oximeter equipment (Adopted ISO 80601-2-61:2017, second edition, 2017-02, with Canadian deviations)*, 2021.

[20] I. Rubinoff, R. V. Kuranov, R. Fang, *et al.*, "Adaptive spectroscopic visible-light optical coherence tomography for clinical retinal oximetry," en, *Communications Medicine*, vol. 3, no. 1, p. 57, Apr. 2023, ISSN: 2730-664X.

[21] S. Liu, R. Zhang, T. Han, *et al.*, "Validation of photoacoustic/ultrasound dual imaging in evaluating blood oxygen saturation," en, *Biomedical Optics Express*, vol. 13, no. 10, p. 5551, Oct. 2022, ISSN: 2156-7085, 2156-7085.

[22] J. Laufer, C. Elwell, D. Delpy, and P. Beard, "*In vitro* measurements of absolute blood oxygen saturation using pulsed near-infrared photoacoustic spectroscopy: Accuracy and resolution," *Physics in Medicine and Biology*, vol. 50, no. 18, pp. 4409–4428, Sep. 2005, ISSN: 0031-9155, 1361-6560.

[23] Y. Jiang, C. Spies, J. Magin, S. J. Bhosai, L. Snyder, and J. Dunn, "Investigating the accuracy of blood oxygen saturation measurements in common consumer smartwatches," en, *PLOS Digital Health*, vol. 2, no. 7, B. Rush, Ed., e0000296, Jul. 2023, ISSN: 2767-3170.

[24] M. W. Sjoding, R. P. Dickson, T. J. Iwashyna, S. E. Gay, and T. S. Valley, "Racial Bias in Pulse Oximetry Measurement," en, *New England Journal of Medicine*, vol. 383, no. 25, pp. 2477–2478, Dec. 2020, ISSN: 0028-4793, 1533-4406.

[25] D. Martin, C. Johns, L. Sorrell, *et al.*, "Effect of skin tone on the accuracy of the estimation of arterial oxygen saturation by pulse oximetry: A systematic review," en, *British Journal of Anaesthesia*, vol. 132, no. 5, pp. 945–956, May 2024, ISSN: 00070912.

[26] S. Prahl, W. B. Gratzer, and N. Kollias, *Tabulated Molar Extinction Coefficient for Hemoglobin in Water*, Mar. 1998.

[27] A. Roggan, M. Friebel, K. Dörschel, A. Hahn, and G. Müller, "Optical Properties of Circulating Human Blood in the Wavelength Range 400–2500 nm," en, *Journal of Biomedical Optics*, vol. 4, no. 1, p. 36, 1999, ISSN: 10833668.

[28] M. Taylor-Williams, G. Spicer, G. Bale, and S. E. Bohndiek, "Noninvasive hemoglobin sensing and imaging: Optical tools for disease diagnosis," *Journal of Biomedical Optics*, vol. 27, no. 08, Aug. 2022, ISSN: 1083-3668.

[29] W. G. Zijlstra, A. Buursma, and O. W. v. Assendelft, *Visible and near infrared absorption spectra of human and animal haemoglobin: determination and application*, eng, 1. publ. Utrecht: VSP International Science Publ, 2000, ISBN: 978-90-6764-317-7.

[30] S. J. Barker, K. K. Tremper, and J. Hyatt, "Effects of Methemoglobinemia on Pulse Oximetry and Mixed Venous Oximetry," en, *Anesthesiology*, vol. 70, no. 1, pp. 112–117, Jan. 1989, ISSN: 0003-3022.

[31] J. B. Hickam, H. O. Sieker, and R. Frayser, "Studies of retinal circulation and A-V oxygen difference in man," eng, *Transactions of the American Clinical and Climatological Association*, vol. 71, pp. 34–44, 1959, ISSN: 0065-7778.

[32] O. B. Olafsdottir, E. Vandewalle, L. Abegão Pinto, *et al.*, "Retinal oxygen metabolism in healthy subjects and glaucoma patients," en, *British Journal of Ophthalmology*, vol. 98, no. 3, pp. 329–333, Mar. 2014, ISSN: 0007-1161, 1468-2079.

[33] B. Khoobehi, K. Firn, H. Thompson, M. Reinoso, and J. Beach, "Retinal Arterial and Venous Oxygen Saturation Is Altered in Diabetic Patients," en, *Investigative Opthalmology & Visual Science*, vol. 54, no. 10, p. 7103, Oct. 2013, ISSN: 1552-5783.

[34] D. J. Mordant, I. Al-Abboud, G. Muyo, *et al.*, "Spectral imaging of the retina," en, *Eye*, vol. 25, no. 3, pp. 309–320, Mar. 2011, ISSN: 0950-222X, 1476-5454.

[35] M. Desjardins, J.-P. Sylvestre, R. Jafari, *et al.*, "Preliminary investigation of multispectral retinal tissue oximetry mapping using a hyperspectral retinal camera," en, *Experimental Eye Research*, vol. 146, pp. 330–340, May 2016, ISSN: 00144835.

[36] B. S. Sorg, B. J. Moeller, O. Donovan, Y. Cao, and M. W. Dewhirst, "Hyperspectral imaging of hemoglobin saturation in tumor microvasculature and tumor hypoxia development," en, *Journal of Biomedical Optics*, vol. 10, no. 4, p. 044 004, 2005, ISSN: 10833668.

[37] B. S. Sorg, M. E. Hardee, N. Agarwal, B. J. Moeller, and M. W. Dewhirst, "Spectral imaging facilitates visualization and measurements of unstable and abnormal microvascular oxygen transport in tumors," en, *Journal of Biomedical Optics*, vol. 13, no. 1, p. 014 026, 2008, ISSN: 10833668.

[38] X. Shu, L. Beckmann, and H. F. Zhang, "Visible-light optical coherence tomography: A review," *Journal of Biomedical Optics*, vol. 22, no. 12, p. 1, Dec. 2017, ISSN: 1083-3668.

[39] F. E. Robles, C. Wilson, G. Grant, and A. Wax, "Molecular imaging true-colour spectroscopic optical coherence tomography," en, *Nature Photonics*, vol. 5, no. 12, pp. 744–747, Dec. 2011, ISSN: 1749-4885, 1749-4893.

[40] S. P. Chong, C. W. Merkle, C. Leahy, H. Radhakrishnan, and V. J. Srinivasan, "Quantitative microvascular hemoglobin mapping using visible light spectroscopic Optical Coherence Tomography," en, *Biomedical Optics Express*, vol. 6, no. 4, p. 1429, Apr. 2015, ISSN: 2156-7085, 2156-7085.

[41] S. Chen, J. Yi, and H. F. Zhang, "Measuring oxygen saturation in retinal and choroidal circulations in rats using visible light optical coherence tomography angiography," en, *Biomedical Optics Express*, vol. 6, no. 8, p. 2840, Aug. 2015, ISSN: 2156-7085, 2156-7085.

[42] J. Yi, W. Liu, S. Chen, *et al.*, "Visible light optical coherence tomography measures retinal oxygen metabolic response to systemic oxygenation," en, *Light: Science & Applications*, vol. 4, no. 9, e334–e334, Sep. 2015, ISSN: 2047-7538.

[43] R. Liu, J. A. Winkelmann, G. Spicer, *et al.*, "Single capillary oximetry and tissue ultrastructural sensing by dual-band dual-scan inverse spectroscopic optical coherence tomography," en, *Light: Science & Applications*, vol. 7, no. 1, p. 57, Aug. 2018, ISSN: 2047-7538.

[44] S. Pi, T. T. Hormel, X. Wei, *et al.*, "Retinal capillary oximetry with visible light optical coherence tomography," en, *Proceedings of the National Academy of Sciences*, vol. 117, no. 21, pp. 11 658–11 666, May 2020, ISSN: 0027-8424, 1091-6490.

[45] W. Song, W. Shao, W. Yi, *et al.*, "Visible light optical coherence tomography angiography (vis-OCTA) facilitates local microvascular oximetry in the human retina," en, *Biomedical Optics Express*, vol. 11, no. 7, p. 4037, Jul. 2020, ISSN: 2156-7085, 2156-7085.

[46] A. Javed, A. Khanna, E. Palmer, *et al.*, "Optical coherence tomography angiography: A review of the current literature," en, *Journal of International Medical Research*, vol. 51, no. 7, p. 03 000 605 231 187 933, Jul. 2023, ISSN: 0300-0605, 1473-2300.

[47] S. S. Hayreh, "Ocular vascular occlusive disorders: Natural history of visual outcome," en, *Progress in Retinal and Eye Research*, vol. 41, pp. 1–25, Jul. 2014, ISSN: 13509462.

[48] M. Laouri, E. Chen, M. Looman, and M. Gallagher, "The burden of disease of retinal vein occlusion: Review of the literature," en, *Eye*, vol. 25, no. 8, pp. 981–988, Aug. 2011, ISSN: 0950-222X, 1476-5454.

[49] Z. Fang, C. Wang, J. Yang, *et al.*, "Oxyhaemoglobin saturation NIR-IIb imaging for assessing cancer metabolism and predicting the response to immunotherapy," en, *Nature Nanotechnology*, vol. 19, no. 1, pp. 124–130, Jan. 2024, ISSN: 1748-3387, 1748-3395.

[50] E. Rathbone and D. Fu, "Quantitative Optical Imaging of Oxygen in Brain Vasculature," en, *The Journal of Physical Chemistry B*, vol. 128, no. 29, pp. 6975–6989, Jul. 2024, ISSN: 1520-6106, 1520-5207.

[51] D. G. Lyons, A. Parpaleix, M. Roche, and S. Charpak, "Mapping oxygen concentration in the awake mouse brain," en, *eLife*, vol. 5, e12024, Feb. 2016, ISSN: 2050-084X.

[52] J. Lecoq, A. Parpaleix, E. Roussakis, *et al.*, "Simultaneous two-photon imaging of oxygen and blood flow in deep cerebral vessels," en, *Nature Medicine*, vol. 17, no. 7, pp. 893–898, Jul. 2011, ISSN: 1078-8956, 1546-170X.

[53] J. Ferrer Ortas, P. Mahou, S. Escot, *et al.*, "Label-free imaging of red blood cells and oxygenation with color third-order sum-frequency generation microscopy," en, *Light: Science & Applications*, vol. 12, no. 1, p. 29, Jan. 2023, ISSN: 2047-7538.

[54] A. M. Larson, "Multiphoton microscopy," en, *Nature Photonics*, vol. 5, no. 1, pp. 1–1, Jan. 2011, ISSN: 1749-4885, 1749-4893.

[55] M. Li, Y. Tang, and J. Yao, "Photoacoustic tomography of blood oxygenation: A mini review," en, *Photoacoustics*, vol. 10, pp. 65–73, Jun. 2018, ISSN: 22135979.

[56] F. Zhong and S. Hu, "Thin-film optical-acoustic combiner enables high-speed wide-field multi-parametric photoacoustic microscopy in reflection mode," en, *Optics Letters*, vol. 48, no. 2, p. 195, Jan. 2023, ISSN: 0146-9592, 1539-4794.

[57] R. Bi, U. Dinish, C. C. Goh, *et al.*, "In vivo label-free functional photoacoustic monitoring of ischemic reperfusion," en, *Journal of Biophotonics*, vol. 12, no. 7, e201800454, Jul. 2019, ISSN: 1864-063X, 1864-0648.

[58] H. F. Zhang, K. Maslov, G. Stoica, and L. V. Wang, "Functional photoacoustic microscopy for high-resolution and noninvasive in vivo imaging," en, *Nature Biotechnology*, vol. 24, no. 7, pp. 848–851, Jul. 2006, ISSN: 1087-0156, 1546-1696.

[59] C. Liu, Y. Liang, and L. Wang, "Optical-resolution photoacoustic microscopy of oxygen saturation with nonlinear compensation," en, *Biomedical Optics Express*, vol. 10, no. 6, p. 3061, Jun. 2019, ISSN: 2156-7085, 2156-7085.

[60] S.-W. Cho, H. Kang, S. M. Park, *et al.*, "Optimal Generation of Ten Individual Green-to-Red Raman Source for Wavelength-Dependent Real-Time OR-PAM Images," *IEEE Journal of Selected Topics in Quantum Electronics*, vol. 25, no. 1, pp. 1–9, Jan. 2019, ISSN: 1077-260X, 1558-4542.

[61] X. Wang, Z. Xie, J. Zhang, Y. Huang, L. Dong, and X. Gong, "Single-wavelength sO2 measurement based on Grüneisen-relaxation photoacoustic effect," en, *Journal of Biophotonics*, vol. 16, no. 8, e202300084, Aug. 2023, ISSN: 1864-063X, 1864-0648.

[62] Y. Liang, W. Fu, Q. Li, *et al.*, "Optical-resolution functional gastrointestinal photoacoustic endoscopy based on optical heterodyne detection of ultrasound," en, *Nature Communications*, vol. 13, no. 1, p. 7604, Dec. 2022, ISSN: 2041-1723.

[63] W. Song, Q. Wei, W. Liu, *et al.*, "A combined method to quantify the retinal metabolic rate of oxygen using photoacoustic ophthalmoscopy and optical coherence tomography," en, *Scientific Reports*, vol. 4, no. 1, p. 6525, Oct. 2014, ISSN: 2045-2322.

[64] T. Shiina, M. Toi, and T. Yagi, "Development and clinical translation of photoacoustic mammography," en, *Biomedical Engineering Letters*, vol. 8, no. 2, pp. 157–165, May 2018, ISSN: 2093-9868, 2093-985X.

[65] J. Yao, K. I. Maslov, Y. Zhang, Y. Xia, and L. V. Wang, "Label-free oxygen-metabolic photoacoustic microscopy in vivo," en, *Journal of Biomedical Optics*, vol. 16, no. 7, p. 076 003, 2011, ISSN: 10833668.

[66] T. Mitcham, H. Taghavi, J. Long, *et al.*, "Photoacoustic-based s O 2 estimation through excised bovine prostate tissue with interstitial light delivery," en, *Photoacoustics*, vol. 7, pp. 47–56, Sep. 2017, ISSN: 22135979.

[67] Z. Hosseinaee, Nima Abbasi, N. Pellegrino, L. Khalili, L. Mukhangaliyeva, and P. Haji Reza, "Functional and structural ophthalmic imaging using noncontact multimodal photoacoustic remote sensing microscopy and optical coherence tomography," en, *Scientific Reports*, vol. 11, no. 1, Jun. 2021, Publisher: Springer Science and Business Media LLC, ISSN: 2045-2322.

[68] J. E. D. Tweel, B. R. Ecclestone, H. Gaouda, *et al.*, "Photon Absorption Remote Sensing Imaging of Breast Needle Core Biopsies Is Diagnostically Equivalent to Gold Standard H&E Histologic Assessment," en, *Current Oncology*, vol. 30, no. 11, pp. 9760–9771, Nov. 2023, ISSN: 1718-7729.

[69] B. R. Ecclestone, K. Bell, S. Sparkes, D. Dinakaran, J. R. Mackey, and P. Haji Reza, "Label-free complete absorption microscopy using second generation photoacoustic remote sensing," en, *Scientific Reports*, vol. 12, no. 1, p. 8464, May 2022, ISSN: 2045-2322.

[70] J. A. Tummon Simmons, S. J. Werezak, B. R. Ecclestone, J. E. D. Tweel, and P. Haji Reza, "Label-free in vivo imaging using photon absorption remote sensing," in *SPIE BiOS*, San Francisco, CA: SPIE, Jan. 2024.

[71] James A. Tummon Simmons, Sarah Werezak, Benjamin R. Ecclestone, Parsin Haji Reza, and Nima Abbasi, "Label-free vasculature imaging using total absorption photoacoustic remote sensing," vol. PC12379, Mar. 2023, PC1237913.

[72] G. P. Agrawal, "Stimulated Raman scattering," eng, in *Nonlinear fiber optics*, Sixth edition, London: Academic Press, an imprint of Elsevier, 2019, ISBN: 978-0-12-817042-7.

[73] R. C. Prince, R. R. Frontiera, and E. O. Potma, "Stimulated Raman Scattering: From Bulk to Nano," en, *Chemical Reviews*, vol. 117, no. 7, pp. 5070–5094, Apr. 2017, ISSN: 0009-2665, 1520-6890.

[74] R. Paschotta, "Polarization-Maintaining Fibers," English, in *Field guide to optical fiber technology*, Bellingham, Wash. (1000 20th St. Bellingham WA 98225-6705 USA): SPIE, Jan. 2010, ISBN: 978-0-8194-8090-3 978-0-8194-8091-0 0-8194-8090-8.

[75] C. Emslie, "Polarization Maintaining Fibers," en, in *Specialty Optical Fibers Handbook*, Elsevier, 2007, pp. 243–277, ISBN: 978-0-12-369406-5.

[76] E. Collett, "Wave Plates," English, in *Field guide to polarization*, Bellingham, Wash. (1000 20th St. Bellingham WA 98225-6705 USA): SPIE, 2005, ISBN: 978-0-8194-5868-1 978-0-8194-7820-7 0-8194-5868-6.

[77] Thorlabs, *Mounted Achromatic Wave Plates*. [Online]. Available: https://www.thorlabs.com/newgrouppage9.cfm?objectgroup_id=854 (visited on 10/10/2024).

[78] E. W. Stein, K. Maslov, and L. V. Wang, "Noninvasive, in vivo imaging of blood-oxygenation dynamics within the mouse brain using photoacoustic microscopy," en, *Journal of Biomedical Optics*, vol. 14, no. 2, p. 020 502, 2009, ISSN: 10833668.

[79] A. Asadollahi, H. Latifi, M. Pramanik, *et al.*, "Axial accuracy and signal enhancement in acoustic-resolution photoacoustic microscopy by laser jitter effect correction and pulse energy compensation," en, *Biomedical Optics Express*, vol. 12, no. 4, p. 1834, Apr. 2021, ISSN: 2156-7085, 2156-7085.

[80] Thorlabs, *Hard-Coated UV/VIS Bandpass Filters*. [Online]. Available: https://www.thorlabs.com/newgrouppage9.cfm?objectgroup_id=1860&pn=FBH570-10 (visited on 09/27/2024).

[81] B. E. A. Saleh and M. C. Teich, "Beam Optics," eng, in *Fundamentals of photonics*, ser. Wiley series in pure and applied optics, Third edition, Hoboken, NJ: Wiley, 2019, ISBN: 978-1-119-50687-4.

[82] Werfen, *Avoximeter 4000*. [Online]. Available: https://www.werfen.com/na/en/point-of-care-testing-devices/avoximeter-4000-co-oximetry-assessment (visited on 02/02/2024).

[83] H. Isler, S. Kleiser, D. Ostojic, F. Scholkmann, T. Karen, and M. Wolf, "Liquid Blood Phantoms to Validate NIRS Oximeters: Yeast Versus Nitrogen for Deoxygenation," en, in *Oxygen Transport to Tissue XL*, O. Thews, J. C. LaManna, and D. K. Harrison, Eds., vol. 1072, Series Title: Advances in Experimental Medicine and Biology, Cham: Springer International Publishing, 2018, pp. 381–385, ISBN: 978-3-319-91285-1 978-3-319-91287-5.

[84] M. Gehrung, S. E. Bohndiek, and J. Brunker, "Development of a blood oxygenation phantom for photoacoustic tomography combined with online pO2 detection and flow spectrometry," *Journal of Biomedical Optics*, vol. 24, no. 12, p. 1, Oct. 2019, ISSN: 1083-3668.

[85] K. Briely-Sabo and A. Bjornerud, "Accurate de-oxygenation of ex vivo whole blood using sodium Dithionite," in *Proc. Intl. Sot. Mag. Reson. Med*, vol. 8, 2000, p. 2025.

[86] ThermoFisher, *Safety Data Sheet: Sodium hydrosulfite*, Oct. 2023.

[87] M. T. Ghijsen, G. R. Lentsch, S. Gioux, *et al.*, "Quantitative real-time optical imaging of the tissue metabolic rate of oxygen consumption," *Journal of Biomedical Optics*, vol. 23, no. 03, p. 1, Mar. 2018, ISSN: 1083-3668.

[88] I. Fredriksson, R. B. Saager, A. J. Durkin, and T. Strömberg, "Evaluation of a pointwise microcirculation assessment method using liquid and multilayered tissue simulating phantoms," *Journal of Biomedical Optics*, vol. 22, no. 11, p. 1, Nov. 2017, ISSN: 1083-3668.

[89] M. Majedy, R. B. Saager, T. Strömberg, M. Larsson, and E. G. Salerud, "Spectral characterization of liquid hemoglobin phantoms with varying oxygenation states," *Journal of Biomedical Optics*, vol. 27, no. 07, Dec. 2021, ISSN: 1083-3668.

[90] F. Lange, L. Dunne, L. Hale, and I. Tachtsidis, "MAESTROS: A Multiwavelength Time-Domain NIRS System to Monitor Changes in Oxygenation and Oxidation State of Cytochrome-C-Oxidase," *IEEE Journal of Selected Topics in Quantum Electronics*, vol. 25, no. 1, pp. 1–12, Jan. 2019, ISSN: 1077-260X, 1558-4542.

[91] D. White and P. Teasdale, "The oxygenation of blood by hydrogen peroxide: In vitro studies," en, *British Journal of Anaesthesia*, vol. 38, no. 5, pp. 339–344, May 1966, ISSN: 00070912.

[92] R. O. Wright, W. J. Lewander, and A. D. Woolf, "Methemoglobinemia: Etiology, Pharmacology, and Clinical Management," en, *Annals of Emergency Medicine*, vol. 34, no. 5, pp. 646–656, Nov. 1999, ISSN: 01960644.

[93] H. U. Rehman, "Methemoglobinemia," *Western Journal of Medicine*, vol. 175, no. 3, pp. 193–196, Sep. 2001, ISSN: 00930415.

[94] R. Palmeri and V. Gupta, "Carboxyhemoglobin Toxicity," eng, in *StatPearls*, Treasure Island (FL): StatPearls Publishing, 2023.

[95] O. Siggaard-Andersen, B. Nørgaard-Pedersen, and J. Rem, "Hemoglobin pigments. spectrophotometric determination of oxy-, carboxy-, met-, and sulfhemoglobin in capillary blood," en, *Clinica Chimica Acta*, vol. 42, no. 1, pp. 85–100, Nov. 1972, ISSN: 00098981.

[96] S. J. Barker and K. K. Tremper, "The Effect of Carbon Monoxide Inhalation on Pulse Oximetry and Transcutaneous Po2," en, *Anesthesiology*, vol. 66, no. 5, pp. 677–679, May 1987, ISSN: 0003-3022.

[97] N. Adili, M. Melizi, and H. Belabbas, "Species determination using the red blood cells morphometry in domestic animals," *Veterinary World*, vol. 9, no. 9, pp. 960–963, Sep. 2016, ISSN: 09728988, 22310916.

[98] M. Diez-Silva, M. Dao, J. Han, C.-T. Lim, and S. Suresh, "Shape and Biomechanical Characteristics of Human Red Blood Cells in Health and Disease," en, *MRS Bulletin*, vol. 35, no. 5, pp. 382–388, May 2010, ISSN: 0883-7694, 1938-1425.

[99] G. Banfi, G. L. Salvagno, and G. Lippi, "The role of ethylenediamine tetraacetic acid (EDTA) as in vitro anticoagulant for diagnostic purposes," *Clinical Chemical Laboratory Medicine*, vol. 45, no. 5, Jan. 2007, ISSN: 14346621, 14374331.

[100] A. Sudakou, H. Wabnitz, A. Liemert, M. Wolf, and A. Liebert, "Two-layered blood-lipid phantom and method to determine absorption and oxygenation employing changes in moments of DTOFs," en, *Biomedical Optics Express*, vol. 14, no. 7, p. 3506, Jul. 2023, ISSN: 2156-7085, 2156-7085.

[101] R. Liu, G. Spicer, S. Chen, H. F. Zhang, J. Yi, and V. Backman, "Theoretical model for optical oximetry at the capillary level: Exploring hemoglobin oxygen saturation through backscattering of single red blood cells," en, *Journal of Biomedical Optics*, vol. 22, no. 2, p. 025 002, Feb. 2017, ISSN: 1083-3668.

[102] K. Kramer, J. O. Elam, G. A. Saxton, and W. N. Elam, "Influence of Oxygen Saturation, Erythrocyte Concentration and Optical Depth Upon the Red and Near-Infrared Light Transmittance of Whole Blood," en, *American Journal of Physiology-Legacy Content*, vol. 165, no. 1, pp. 229–246, Mar. 1951, ISSN: 0002-9513.

[103] S. Jenne and H. Zappe, "Multiwavelength tissue-mimicking phantoms with tunable vessel pulsation," *Journal of Biomedical Optics*, vol. 28, no. 04, Apr. 2023, ISSN: 1083-3668.

[104] A. M. Goldfain, P. Lemaillet, D. W. Allen, K. A. Briggman, and J. Hwang, "Polydimethylsiloxane tissue-mimicking phantoms with tunable optical properties," *Journal of Biomedical Optics*, vol. 27, no. 07, Nov. 2021, ISSN: 1083-3668.

[105] A. A. Galyastov, D. D. Stavtsev, I. O. Kozlov, A. N. Konovalov, A. Y. Gerasimenko, and D. V. Telyshev, "Determination of the Flow Parameters of a Scattering Liquid in a Microfluidic Blood Vessel Phantom Based on Laser Speckle Contrast Imaging," en, *Biomedical Engineering*, vol. 57, no. 2, pp. 127–131, Jul. 2023, ISSN: 0006-3398, 1573-8256.

[106] A. S. Cruz-Félix, A. Santiago-Alvarado, J. Márquez-García, and J. González-García, "PDMS samples characterization with variations of synthesis parameters for tunable optics applications," en, *Heliyon*, vol. 5, no. 12, e03064, Dec. 2019, ISSN: 24058440.

[107] S. Liu, Z. Deng, J. Li, J. Wang, and N. Huang, "Measurement of the refractive index of whole blood and its components for a continuous spectral region," *Journal of Biomedical Optics*, vol. 24, no. 03, p. 1, Mar. 2019, ISSN: 1083-3668.

[108] N. Bosschaart, G. J. Edelman, M. C. G. Aalders, T. G. Van Leeuwen, and D. J. Faber, "A literature review and novel theoretical approach on the optical properties of whole blood," en, *Lasers in Medical Science*, vol. 29, no. 2, pp. 453–479, Mar. 2014, ISSN: 0268-8921, 1435-604X.

[109] MATLAB, *Boxplot*. [Online]. Available: https://www.mathworks.com/help/stats/boxplot.html.

[110] P. Nowak-Sliwinska, T. Segura, and M. L. Iruela-Arispe, "The chicken chorioallantoic membrane model in biology, medicine and bioengineering," en, *Angiogenesis*, vol. 17, no. 4, pp. 779–804, Oct. 2014, ISSN: 0969-6970, 1573-7209.

[111] F. Li, *DFRobot DHT20*, Jun. 2021. [Online]. Available: https://github.com/DFRobot/DFRobot_DHT20 (visited on 09/08/2024).

[112] Z. Liu, *DFRobot Oxygen Sensor*, Oct. 2021. [Online]. Available: https://github.com/DFRobot/DFRobot_OxygenSensor (visited on 09/08/2024).

[113] DFRobot, *SEN0322*. [Online]. Available: https://wiki.dfrobot.com/Gravity_I2C_Oxygen_Sensor_SKU_SEN0322 (visited on 09/08/2024).

[114] ASAIR, *Data Sheet DHT20*, May 2021. [Online]. Available: https://cdn.sparkfun.com/assets/8/a/1/5/0/DHT20.pdf.

[115] Ronald Charbonneau, Lee Niel, Ernest Olfert, Marina von Keyserlingk, and Gilly Griffin, *CCAC guidelines on: Euthanasia of animals used in science*, 2010.

[116] *AVMA Guidelines for the Euthanasia of Animals: 2020 Edition*, 2020.

[117] N. Otsu, "A Threshold Selection Method from Gray-Level Histograms," *IEEE Transactions on Systems, Man, and Cybernetics*, vol. 9, no. 1, pp. 62–66, Jan. 1979, ISSN: 0018-9472, 2168-2909.

[118] R. B. Reeves, "Blood oxygen affinity in relation to yolk-sac and chorioallantoic gas exchange in the developing chick embryo," en, in *Respiration and metabolism of embryonic vertebrates*, R. S. Seymour, Ed., Dordrecht: Springer Netherlands, 1984, pp. 231–244, ISBN: 978-94-009-6538-6 978-94-009-6536-2.

[119] R. Baumann and H. J. Meuer, "Blood oxygen transport in the early avian embryo," en, *Physiological Reviews*, vol. 72, no. 4, pp. 941–965, Oct. 1992, ISSN: 0031-9333, 1522-1210.

[120] F. Faul, E. Erdfelder, A.-G. Lang, and A. Buchner, "G*Power 3: A flexible statistical power analysis program for the social, behavioral, and biomedical sciences," en, *Behavior Research Methods*, vol. 39, no. 2, pp. 175–191, May 2007, ISSN: 1554-351X, 1554-3528.

APPENDICES

Appendix A

In vitro Blood Preparation Additional Information

A.1 H_2O_2 Volumes for Blood Re-oxygenation

The method for re-oxygenation of blood uses small volumes of 30 wt.% H_2O_2 (Sigma-Aldrich, 216763) mixed into blood deoxygenated with yeast. Table A.1 provides examples of H_2O_2 volumes used to re-oxygenate blood. H_2O_2 volumes depend on the initial SO_2 value, blood volume and the desired SO_2 value.

Initial SO_2	Blood (mL)	H_2O_2 (μL)	Resulting SO_2
20.20%	3	2.0	55.7%
20.20%	3	3.0	75.7%
20.20%	3	4.5	81.0%

Table A.1: Blood re-oxygenation to intermediate SO_2 values.

Appendix B

Initial Phantom Designs

This section summarizes the previous iterations of phantom designs which preceded the design presented in Chapter 5.

B.1 Design A: Liquid Sample Holder

The first design for imaging liquid samples such as blood was designed in SolidWorks and 3D printed. This device contained a liquid chamber, as well as an alignment chamber. Carbon fibers were glued to the staircase for the determination of depth and alignment in a sample. Both chambers were sealed with a coverslip and superglue. Inflow and outflow ports enabled the flow of liquid and additional ports were designed at the corner of each chamber to allow for a syringe to be inserted for air bubble removal. The biggest takeaway from this design was the importance of reflective surfaces for back-scattering. Since the chambers were relatively deep, no non-radiative signal could be measured.

B.2 Design B: Flow Phantom Version 1

The challenges in Design A motivated the first iteration of a flow phantom. The goal was to create small channels and enable flowing blood to be imaged. The design was inspired by Galyastov et al. [105] and used a 3D printed mold that created flow channels of 500 μm, 300 μm and 100 μm. Due to resolution limitations of the 3D printer, the formation of the 100 μm channel was unsuccessful. PDMS was poured into the mold and allowed to cure.

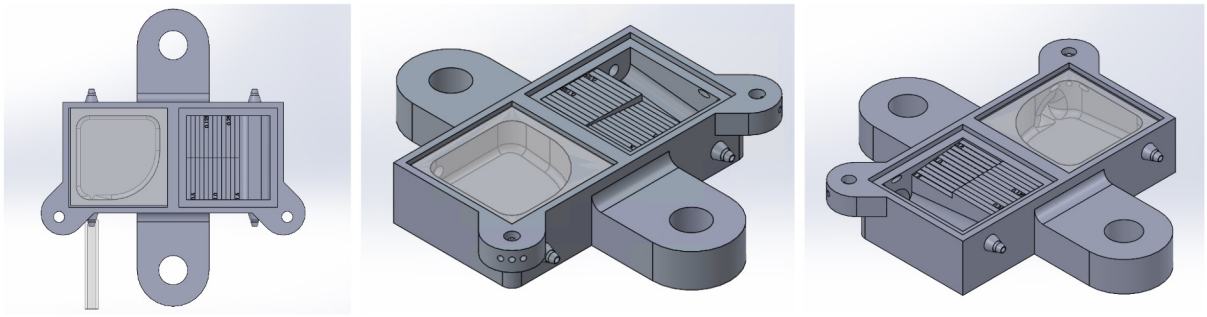


Figure B.1: Liquid sample holder SolidWorks model.

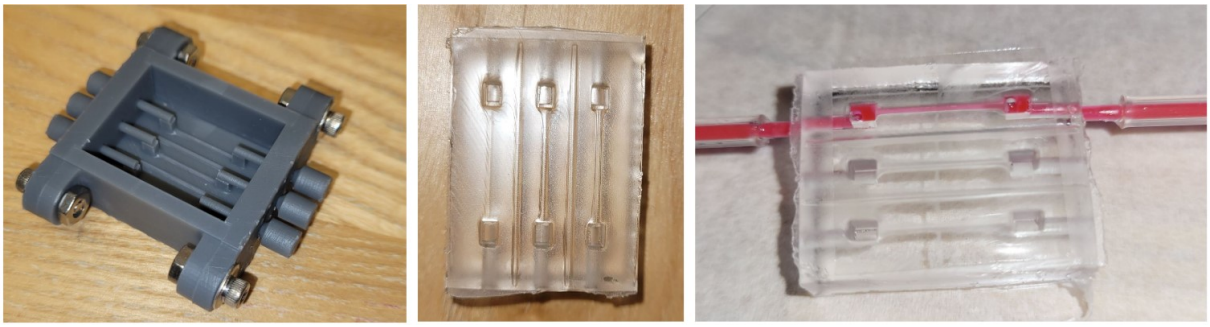


Figure B.2: Flow Phantom Design B, illustrating the 3D printed mold (left), the cured PDMS (center) and the flow phantom with a sample of red craft dye (right).

Then UV plasma cleaning, followed by heating in an oven was used to bond the the PDMS to a coverslip to complete the flow channel [105]. Carbon fibers and water were used in the alignment channels to assist with the determination of depth and alignment. This model was successful in creating a 500 and 300 μm flow channel, however non-radiative signal could still not be attained using this approach. Chapter 5 discusses the subsequent flow phantom design with a 50 μm channel, from which non-radiative signal could be captured.